UNIVERSIDAD DE JAÉN

DOCTORAL THESIS

Characterization of the cerebrospinal fluid flow in the spinal subarachnoid space

---

Author:
Francisco MORAL PULIDO

Supervisors:
Prof. Cándido GUTIÉRREZ MONTES
Prof. Carlos MARTÍNEZ BAZÁN

in the

Grupo de Mecánica de Fluidos TEP-991
Departamento de Ingeniería Mecánica y Minera

Jaén, September 6, 2023

DEPARTAMENTO DE INGENIERÍA MECÁNICA Y MINERA
Escuela Politécnica Superior de Jaén

Characterization of the cerebrospinal fluid flow in the spinal subarachnoid space

Caracterización del flujo cefalorraquídeo en el espacio subaracnoideo espinal

Autor
Francisco Moral Pulido

Directores de Tesis
Prof. Cándido Gutiérrez Montes
Prof. Carlos Martínez Bazán

Jaén, September 6, 2023

A mis padres, mi hermano y Bea

Tesis Doctoral

CHARACTERIZATION OF THE CEREBROSPINAL FLUID FLOW IN THE SPINAL SUBARACHNOID SPACE

Autor:
Francisco Moral Pulido

Directores de Tesis:
Prof. Cándido Gutiérrez Montes
Prof. Carlos Martínez Bazán

Firma del tribunal Calificador:

Firma

Presidente:
Vocal:
Secretario:
Suplente:
Suplente:

Calificación:

Jaén, September 6, 2023

Agradecimientos

La presente tesis muestra un capítulo de mi vida, en el que he crecido tanto en el ámbito profesional como en lo personal. Por suerte, este camino no lo he recorrido solo, y es por esto que quiero agradecer en estas líneas a quienes me han acompañado en este viaje.

Primero, quiero mostrar mi agradecimiento a mis directores de tesis. A Cándido, que me diste la oportunidad de empezar a colaborar en esta familia hace 4 años y adentrarme en el mundo académico, gracias por haberme guiado durante esta etapa iniciándome como docente e investigador, por todas las charlas y consejos, con esa paciencia que te caracteriza y retrasando alguna que otra reunión si era necesario. A Carlos, un referente para todos nosotros y ejemplo a seguir, gracias por hacerme partícipe de esta línea de trabajo, por todo lo que me has enseñado tanto en lo académico como en lo personal, con autoridad pero siempre con amabilidad. Del mismo modo, aunque no hayan formado parte la dirección de esta tesis, quiero dar las gracias a José Ignacio, que siempre tiene la puerta abierta para cualquier cosa a pesar de la enorme carga de trabajo que lleva sobre sus hombros, y a Rocío, gracias por darme la oportunidad de dar mis primeros pasos en la investigación en este grupo durante mis estudios de grado, por mi primera toma de contacto en el arduo terreno experimental y todo lo relacionado con becas y ayudas. En este aspecto, agradezco a la Universidad de Jaén y al Ministerio de Universidades la financiación recibida para desarrollar mis estudios de doctorado, a través de una Ayuda a la Formación de Profesorado Universitario FPU18/05694 (MU), así como la Acción 5B del Plan Operativo de Apoyo a la Investigación (Vicerrectorado de Investigación de la Universidad de Jaén) con la que pude realizar mi estancia predoctoral en UCSD.

No puedo dejar en el tintero a quienes me acogieron en la "sala de doctorandos", aquella dependencia de la planta baja del A3. A Javi, gracias por enseñarme a desenvolverme en el laboratorio junto a Rocío, por todos los consejos que me has dado de forma interesada. A Manu, muchas gracias por todos los consejos y críticas constructivas para perfeccionar mis experimentos. A ambos, muchas gracias por toda vuestra ayuda, me ha permitido ahorrarme mucho tiempo y lograr que mi trabajo sea de mayor calidad. A Carlos, gracias por haber sido un gran apoyo con nuestras charlas científicas (y no tanto) en los cafés, concluyendo siempre con la necesidad de comprar algún artículo de informática. A Antonio José, con quien comparto línea de trabajo y, ante todo, un gran amigo, muchas gracias por nuestras charlas distendidas en las que siempre acabamos mostrando nuestra pasión por la ciencia. Del mismo modo, no puedo olvidarme de los que han ido llegando en el transcurso de mi tesis: a Camacho, Cecilia y José Carlos, personas muy trabajadoras que seguro que llegarán muy lejos, gracias por todos los momentos compartidos en el laboratorio. Y cómo no, no puedo olvidarme de Mario y Arturo, nuestros técnicos de laboratorio, gracias por todo el apoyo que he recibido de vosotros a lo largo de estos años. A todos vosotros, gracias por haber hecho que ir a la universad se haya hecho tan ameno estos años.

Al escribir estas líneas, me doy cuenta de todas aquellas personas que han estado presentes en estos años y con las que he compartido tantos momentos, lo que daría lugar a que la extensión de los agradecimientos tienda al infinito. No obstante, intentaré hacer un pequeño resumen, ya que no es el objeto de esta tesis: en primer

lugar, quiero agradecer a los compañeros del departamento de Ingeniería Mecánica y Minera toda la ayuda en lo que se refiere a gestiones y cualquier cosa que haya podido necesitar, gracias por el buen trato que siempre he recibido. Del mismo modo, quiero agradecer a los compañeros del departamento de Ingeniería Eléctrica y del departamento de Ingeniería Gráfica, Diseño y Proyectos (actuales vecinos de despacho) por los buenos ratos que hemos pasado en pasillos, comentando el estado de nuestras respectivas tesis y cómo de larga se nos ha hecho la espera para la aceptación de algún artículo. Además, no puedo olvidar a los compañeros del IISTA: las charlas a la hora del almuerzo y entre cafés hicieron que mi estancia en Granada, de por sí breve, pasara en un abrir y cerrar de ojos.

De manera un tanto especial quiero mencionar mi estancia en San Diego. Jamás se desvanecerá de mi memoria el día en el que, con la maleta cargada de ilusiones, cogí un vuelo en la T4 de Barajas y viví lo que pudo ser el día más largo de mi vida, trasladando mi lugar de residencia a la otra punta del globo durante tres meses. Quiero agradecer a los miembros del MAE, a Brandon, Daibo, Guillermo, Javi, todas las personas de UCFit, los también visitantes de la UPM y el autodenominado 'trío calavera' todo lo vivido; gracias por tantos momentos inolvidables. Como mención especial, quiero dar las gracias a Obed por hacerme sentir uno más en el laboratorio, a Stephanie y Troy por acogerme con una hospitalidad excepcional, propia de un miembro de la familia, y a Antonio, por ser el perfecto anfitrión: siempre estaré eternamente agradecido.

Finalmente y, en un ámbito ajeno a lo profesional, quiero dedicar estas últimas líneas a mis amigos, a los que he hecho a lo largo de este camino y a los que conozco desde siempre: gracias por hacer que la balanza entre lo personal y profesional estuviera equilibrada en la medida de lo posible. Gracias a mis abuelos, tíos y primos, a los que todavía están y a los que se despidieron hace tiempo, vosotros sois partícipes de que haya llegado hasta aquí. Por último, quiero agradecer a mi padre y a mi madre, quienes me han guiado a lo largo de los años de la mejor forma posible y me han hecho ser quien soy, a mi hermano Nono con quien he compartido tanto, y a Bea, quien llegó hace 10 años y me ha aportado tanto. Gracias por tanto.

Resumen

El líquido cefalorraquídeo (LCR) es un fluido incoloro que baña los espacios ventriculares y el espacio subaracnoideo (ESA), rodeando al sistema nervioso central (SNC). Dicho líquido, proveniente del plasma sanguíneo, se comporta como un fluido Newtoniano, presentando propiedades físicas similares a las del agua.

El LCR presenta una serie de funciones mecánicas y fisiológicas que asegura la protección y el correcto funcionamiento del SNC. Entre ellas se puede destacar que el LCR amortigua los posibles impactos del cerebro en la bóveda craneal, así como que reduce el peso aparente del SNC y evita sobrepresiones en la base del cráneo. Así mismo, el LCR regula los niveles electrolíticos y de acidez del SNC, al igual que actúa como el sistema linfático del SNC debido a la ausencia de éste. Dentro de las diferentes propiedades del LCR, cabe mencionar de forma particular la efectividad de este líquido como medio de transporte de sustancias entre el SNC y el sistema circulatorio, como es el transporte de hormonas, nutrientes y desechos del metabolismo celular. Por lo tanto, se hace necesaria la presencia del LCR, así como el adequado movimiento del mismo, ya que la ausencia de movimiento o el flujo abnormal de éste puede afectar a las funciones vitales del SNC.

En relación al LCR como vehículo de sustancias, el movimiento del LCR genera también interés clínico debido a la posibilidad de suministrar medicamentos que accedan directamente al SNC, lo cual aumenta la efectividad de los tratamientos, pese a que también presenta riesgos sobre el paciente. Esta cualidad hace que crezca el interés de conocer los mecanismos del movimiento del LCR para así obtener mejore protocolos de sumistro de medicamentos, siendo éste el objetivo principal de esta tesis: la caracterización del flujo del líquido cefalorraquídeo en el espacio subarachnoideo espinal.

La presente disertación se divide en tres partes diferenciadas: en cada una de las partes se abordará un problema que, pese a pertenecer a la temática principal, se centra en un aspecto diferente a tratar. La primera parte de la disertación se centra en la caracterización del movimiento del LCR en el canal espinal, así como la dispersión de solutos en el mismo. La presente caracterización se realizará desde dos puntos de vista: en primer lugar, se hará un estudio paramétrico del problema, basado en aspectos fundamentales como la geometría del canal, la naturaleza del movimiento del LCR y el acoplamiento con la deformación del canal, propia del problema de interacción fluido-estructura que se aborda. Este estudio se extiende a un análisis experimental, el cual validará los resultados previamente obtenidos. Para ello, el estudio se realiza sobre un modelo previamente desarrollado por el grupo de investigación, el cual simplifica la compleja geometría del canal espinal a un canal anular, esbelto y excéntrico. Los resultados de este análisis muestran una corriente estacionaria de segundo orden, la cual permite el transporte de sustancias a lo largo del canal y cuya topología depende de las condiciones fijadas por los parámetros del problema.

La segunda parte de esta disertación pretende introducir en el problema un elemento adicional que en la primera simplificación no se tiene en cuenta: la microanatomía del canal. En esta parte se pretende caracterizar de forma experimental los patrones que aparecen en el flujo por la presencia de estos elementos microanatómicos, los cuales pueden influir en el transporte de sustancias. Para ello, se realiza una simplificación del problema gracias a la naturaleza multiescala del mismo, permitiendo considerar el flujo alrededor de un obstáculo que se erije en un canal plano delimitado por paredes inferior y superior. Este análisis evaluará los patrones generados para diferentes variables, como el movimiento del fluido, la geometría, así como el número de elementos y su distribución. Como resultado de este trabajo se generan celdas de recirculación en las inmediaciones del elemento, las cuales varían en función de los parámetros anteriormente citados.

Por último, la tercera parte de esta disertación se centra en el movimiento del LCR en el acueducto cerebral, un conducto situado en el espacio subaracnoideo cerebral (ESAC), pero de interés clínico para el diagnóstico de desórdenes en el movimiento del LCR generados por malformaciones, como puede ser la hidrocefalia de presión normal (HPN). En este aspecto, se pretende caracterizar *in vitro* la presión de apertura, siendo ésta la presión entre los ventrículos laterales y la entrada del canal espinal, así como la relación entre esta presión y el caudal de LCR en el acueducto, de acuerdo a los parámetros biológicos del problema, validados posteriormente por el modelo matemático propuesto en estudios previos del grupo de investigación. Los resultados de este último estudio muestran una clara dependencia del valor promediado integral de la presión de apertura y del desfase con el caudal de la naturaleza del flujo presentando buen acuerdo entre medidas experimentales y predicciones teóricas, lo que muestra el potencial del modelo desarrollado en estudios previos.

Los resultados derivados de este trabajo han sido publicados o están en trámites de publicación en los siguientes artículos:

- **F. Moral-Pulido**, J.I. Jiménez-González, C. Gutiérrez-Montes, W. Coenen, A.L. Sánchez & C. Martínez-Bazán (2023) *In vitro* characterization of solute transport in the spinal. *Physics of Fluids*, 35, 5, 10.1063/5.0150158.
- S. Sincomb, **F. Moral-Pulido**, O. Campos, V. Haughton, C. Martínez-Bazán & A.L. Sánchez (2023) An *in vitro* experimental investigation of oscillatory flow in the cerebral aqueduct. *Enviado al European Journal of Mechanics-B/Fluids.*
- A.J. Bárcenas-Luque, **F. Moral-Pulido**, C. Gutiérrez-Montes, W. Coenen, C. Martínez-Bazán & A.L. Sánchez (2023) Steady streaming around a circular cylindrical post confined between two parallel plates. *En preparación.*
- **F. Moral-Pulido**, C. Gutiérrez-Montes, W. Coenen, A.L. Sánchez & C. Martínez-Bazán (2023) Parametric relationship of the geometrical factors, flow conditions and Fluid-Structure interaction in CSF flow and solute transport. *En preparación.*

Palabras Clave: Mecánica de fluidos biológicos, medidas experimentales, presión intraventricular, líquido cefalorraquídeo e interacción fluido-estructura.

UNIVERSIDAD DE JAÉN

Abstract

Escuela Politécnica Superior de Jaén
Departamento de Ingeniería Mecánica y Minera

Doctor of Philosophy

Characterization of the cerebrospinal fluid flow in the spinal subarachnoid space

by Francisco Moral Pulido

The cerebrospinal fluid (CSF) is a colourless liquid which bathes the ventricular and subarachnoid spaces (SAS), surrounding the central nervous system (CNS). This fluid, filtrated from blood plasma, behaves as a Newtonian fluid with close-to-water physical properties.

The CSF presents several mechanical an physiological functions, which guarantee the protection and well performance of the CNS. Among these properties, the CSF cushions the impacts of the brain within the cranial vault, as well as it reduces the apparent weight of the CNS and, therefore, it avoids the overpressure at the base of the cranium. Furthermore, the CSF keeps the electrolytic environment and the systemic acid-base balance, as well as the CSF is the lymphatic system of the CNS due to it absence. Among all the properties of the CSF, special interest is remarked in the effectiveness of this liquid as a transport medium of substances between the CNS and the circulatory system, such as the transport of hormones, nutrients and wastes from cellular metabolism. Thus, the presence of the CSF and its correct motion are necessary to the adequate performance of the CNS: the absence of CSF motion or abnormal CSF dynamics may compromise the functions of the CNS.

Regarding the CSF as a substance transport, its motion also generates clinical interest due to the possibility of delivering drugs with direct access to the CNS, which enhances the effectiveness of the treatments despite the potential risks. This quality increases the interest in understanding the governing mechanisms of CSF motion in order to improve the drug delivery protocols, being the main goal of this thesis: the characterization of the CSF flow in the spinal subarachnoid space (SSAS).

This dissertation is divided into three different parts: each part addresses a problem that, despite belonging to the main research line, focuses on a different aspect to deal with. The first part of this dissertation is focused on the characterization of the CSF motion and the solute dispersion along the SSAS. This characterization is developed from two different points: on the one hand, a parametric study of the problem is performed. The analysis is based on the fundamental aspects of the problem, i.e. the geometry of the canal, the nature of the CSF motion and its coupling with the deformation of the canal, characteristic in fluid-structure interaction problems. This study is complemented by *in vitro* experiments, whose results validate the model predictions. To that end, the experiments are conducted in a model, previously developed in other works of the research group, which simplifies the complex geometry of the spinal canal to a slender, eccentric annular canal. Results of this analysis show

a second order steady bulk circulation, which drives the transport substances along the spinal canal and whose topology depends on the governing parameters.

The second part of this dissertation includes an extra element not taken into account in the first simplification, i.e. the microanatomy of the canal. In this part, the steady flow patterns induced by the microanatomic elements, which may change the transport dispersion, are characterized through *in vitro* measurements. To that end, the trabeculae and nerve roots are modeled as circular posts confined between two parallel plates. This analysis evaluates the flow patterns generated for different flow conditions, as well as the number of elements and their distribution. As a result, different types of recirculating cells are generated near the elements depending on the governing parameters.

Finally, the third part of this dissertation focuses on the CSF motion along the cerebral aqueduct, a narrow canal located in the cerebral subarachnoid space (CSAS) with clinical potential to diagnose disorders of the CSF motion due to malformations, such the normal pressure hydrocephalus (NPH). In fact, this work aims at characterizing experimentally the transmantle pressure (the instantaneous pressure difference between the lateral ventricles and the entrance of the spinal canal), as well as the relationship between this pressure and the associated CSF flow rate along the aqueduct. The experimental measurements are compared with the results given by a mathematical model previously developed by the research team. Results of the study show a strong dependence of the mean-integral transmantle pressure and the corresponding phase lag of the flow rate with the flow nature. These results are in good agreement with the model predictions, so that they show the clinical potential of the developed model to identify the pressure drop with noninvasive techniques, which is drastically less risky compared with other treatments.

The results of this dissertation have been published or are being submitted to the following journals:

- **F. Moral-Pulido**, J.I. Jiménez-González, C. Gutiérrez-Montes, W. Coenen, A.L. Sánchez & C. Martínez-Bazán (2023) *In vitro* characterization of solute transport in the spinal. *Physics of Fluids*, 35, 5, 10.1063/5.0150158.
- S. Sincomb, **F. Moral-Pulido**, O. Campos, V. Haughton, C. Martínez-Bazán & A.L. Sánchez (2023) An *in vitro* experimental investigation of oscillatory flow in the cerebral aqueduct. *Submitted to the European Journal of Mechanics-B/Fluids.*
- A.J. Bárcenas-Luque, **F. Moral-Pulido**, C. Gutiérrez-Montes, W. Coenen, C. Martínez-Bazán & A.L. Sánchez (2023) Steady streaming around a circular cylindrical post confined between two parallel plates. *Under preparation.*
- **F. Moral-Pulido**, C. Gutiérrez-Montes, W. Coenen, A.L. Sánchez & C. Martínez-Bazán (2023) Parametric relationship of the geometrical factors and flow conditions in CSF flow and solute transport. *Under preparation.*

Keywords: Biological fluid mechanics, experimental measurements, intraventricular pressure, Cerebrospinal fluid, fluid-structure interaction.

Contents

Agradecimientos **ix**

Resumen **xi**

Abstract **xiii**

1 Introduction **1**
1.1 General context and motivation 1
1.2 CSF flow in the spinal canal 3
1.3 CSF flow in the cerebral aqueduct 6
1.4 Outline of the dissertation 8

I Characterization of the CSF flow in the spinal canal **11**

2 Parametric study of the CSF motion and solute transport along the spinal canal **13**
2.1 Introduction 13
2.2 Problem Description 14
2.3 Results 17
2.3.1 Effect of α and β 17
2.3.2 Effect of the wavelength of the elastic wave, k 27
2.3.3 Effect of the compliance of the canal, $\gamma(s)$ 31
2.4 Conclusions 33

3 *In vitro* characterization of the solute transport along the spinal canal **35**
3.1 Introduction 35
3.2 Experimental details and techniques 36
3.3 Results 41
3.3.1 Constant eccentricity configuration: effect of β and α 42
3.3.2 Variable eccentricity configuration 48
3.4 Conclusions 50

II Microanatomy effects on the CSF flow in the spinal canal **53**

4 Oscillatory flow around circular posts: on the effect of microanatomy **55**
4.1 Introduction 55
4.2 Problem description 56
4.3 Experimental setup 57
4.4 Results 59
4.4.1 Effect of the flow frequency: α 60
4.4.2 Effect of ε 61

4.4.3 Time-averaged Lagrangian motion in anharmonic oscillating flows: CSF flow 62
4.4.4 Time-averaged motion around a linear array of posts 64
4.5 Conclusions 66

III Characterization of the CSF flow in the cranial SAS 67

5 *In vitro* characterization of the oscillatory flow in the cerebral aqueduct 69
5.1 Introduction 69
5.2 Problem description 71
5.3 Experimental details and techniques 74
5.4 Results 78
5.5 Conclusions 82

6 Conclusions 85
6.1 General conclusions 85
6.2 Future work 88

Bibliography 91

List of Figures

1.1 Total volume of the cerebrospinal fluid, distributed into the ventricles (blue box), the cerebral subarachnoid space (green box) and the spinal subarachnoid space with cross-sections at different levels (red box). Image extracted from Sass et al. [5]. 2
1.2 Anatomy of the SSAS of a healthy human with axial cuts at several locations and the CSF colored in blue. Extracted from Moral-Pulido et al. [26] 4
1.3 a) Schematic view of the CSAS and the cerebral ventricular system (extracted from Sincomb et al. [72]). b) Schematic view of the cerebral ventricular system (BodyParts3D, ©The Database Center for Life Science licensed under CC Attribution-Share Alike 2.1 Japan). c) 3D model of the cerebral aqueduct. 7

2.1 Schematic view of the geometry of the spinal canal with their corresponding variables, according to Sánchez et al.[29]. Here, a) shows a straight one of constant eccentricity (left) and a curved one whose eccentricity varies along the canal (right). b) Cross section of the canal. 15
2.2 Profiles of the streamwise velocity components of the CSF motion along the spinal canal in the canonical case, $\bar{h}(s) = 1 - \beta\cos(2\pi s)$, at $s = 0$, 0.25 and 0.5 respectively ($\beta = 0.5$, $\alpha = 3$, $k = 10^{-3}$). 18
2.3 Comparison of the CSF velocity profiles at $x = 0$, for a canal geometry given by $\bar{h}(s) = 1 - \beta\cos(2\pi s)$ with $\beta = 0.5$, $k = 10^{-3}$, and different values of α, at azimuthal positions $s = 0$, 0.25 and 0.5 respectively. . . 19
2.4 a) Evolution of the $Re(G)$ (solid lines) and $Im(G)$ (dashed lines) with η for different values of $\alpha\bar{h}/2$ and, b) Complex function G, displayed as $Im(G)$ versus $Re(G)$, for different values of $\alpha\bar{h}/2$. 20
2.5 Evolution of the solute dispersion along the spinal canal using the canonical geometry $\bar{h}(s) = 1 - \beta\cos(2\pi s)$, with $\beta = 0.5$ and $k = 10^{-3}$, for different values of α. 21
2.6 Contours of the axial Lagrangian velocity, u_L, at $x = 0$ for different values of the Womersley number, α, and the eccentricity of the canal, β, with $k = 10^{-3}$. 22
2.7 a) Dependence with α of the time taken by the solute to reach the cranial vault, τ_c, for different values of β. b) Evolution of $\tau_c|_{max}$, with the canal eccentricity, β. 23
2.8 Comparison of the velocity fields obtained using the straight and the curved geometries. a) Contours of the axial, u_L, and azimuthal, w_L, Lagrangian velocities at different downstream positions. b) Lagrangian streamlines of the width averaged values of the axial and azimuthal velocities $\int_0^1 u_L d\eta$ and $\int_0^1 w_L d\eta$ in the $s - x$ plane with contours of $q_L = \left[(\int_0^1 u_L d\eta)^2 + (\int_0^1 w_L d\eta)^2\right]^{1/2}$, the width-averaged Lagrangian velocity magnitude. Here $\alpha = 3$ and $k = 10^{-3}$. 24

2.9 Evolution of the solute dispersion along the spinal canal using the curved geometry $\bar{h}(s) = 1 - \beta\cos(2\pi x)\cos(2\pi s)$, with $\beta = 0.5$ and $k = 10^{-3}$, for different values of α. 26
2.10 Downstream evolution of $p_0'(x)$ for different values of k at several instants of time using the straight geometry ($\beta = 0.5$, $\alpha = 3$). 27
2.11 Downstream evolution of the axial component of the Lagrangian velocity, $u_L(x, 0.5, 0)$, at $\eta = 0.5$ and $s = 0$, for different values of k in the straight geometry ($\beta = 0.5$, $\alpha = 3$). 28
2.12 Comparison of the Lagrangian streamlines of the width averaged values of the axial and azimuthal velocities $\int_0^1 u_L d\eta$ and $\int_0^1 w_L d\eta$ in the $s - x$ plane with contours of $q_L = \left[(\int_0^1 u_L d\eta)^2 + (\int_0^1 w_L d\eta)^2\right]^{1/2}$ for different values of k. Here $\alpha = 3$ and $\bar{h}(s) = 1 - \beta\cos(2\pi s)$ with $\beta = 0.5$. . . . 29
2.13 Comparison of the Lagrangian streamlines of the width averaged values of the axial and azimuthal velocities $\int_0^1 u_L d\eta$ and $\int_0^1 w_L d\eta$ in the $s - x$ plane with contours of $q_L = \left[(\int_0^1 u_L d\eta)^2 + (\int_0^1 w_L d\eta)^2\right]^{1/2}$ for different values of k. Here $\alpha = 3$ and $\bar{h}(x, s) = 1 - \beta\cos(2\pi x)\cos(2\pi s)$ with $\beta = 0.5$. 30
2.14 Dependence on k of the time the solute, initially located at $x = 0.5$, takes to reach the cranial vault, τ_c, for both the straight and the curved geometries with $\alpha = 3$. 31
2.15 Flexible wall motion (upper panel) given by the three different compliance functions of the canal, $\gamma(s)$, shown in the lower plot. 32
2.16 Evolution of $\tau_c(\alpha)$ with α for different compliance functions implemented in the straight geometry with $\beta = 0.5$ and $k = 0.001$. a) $\gamma_A(s) = 3(1 - \gamma_i)(16s^2 - 8s + 1) + \gamma_i$ and b) $\gamma_B(s) = 12(\gamma_i - 1)(2s - 1)s + \gamma_i$. In both cases, $\gamma_i \in [0, 1]$. 33

3.1 a) Schematic representation of the experimental *in vitro* facility of the SSAS. b) Representation of the constant eccentricity canal and c) variable eccentricity canal, with cross sections at planes $x = x^*/L = 0$, 0.5 and 1, showing the dimensionless curvilinear coordinates (x, s, η) which vary from zero to unity, defined in Chapter 2. d) Schematic view of the unperturbed canal width and the eccentricity, e_v, where $e_v(x^*) = e$ in the constant eccentricity canal and $e_v(x^*) = e\cos(2\pi x^*/L)$ in the variable one. 37
3.2 Schematic view of the complete setup: *in vitro* model of the SAS, cameras, programmable peristaltic pump and UV lighting. The flow rate wave form provided by the pump is also displayed in the figure with $Q^*(t^*) = Q_{max}\sin(\omega t^*)$, and the corresponding stroke volume, $\Delta V = 2\,Q_{max}/\omega$, ... 38
3.3 Time sequence of the experimental evolution of the solute along the spinal canal for $\beta = 0.42$ and $\alpha = 4.39$ (experimental set 5 in Table 3.1). The upper and central rows show the experimental frontal and side views, while the bottom row shows the results obtained from the mathematical model (the red and green boxes represent the frontal and side views, respectively). Here, W and N indicate the widest and the narrowest sections of the canal. 41

3.4 Distribution of streamwise components of the steady-streaming, Stokes-drift, and Lagrangian velocity fields at different downstream locations, x. Streamlines obtained for the width-averaged Lagrangian components $\int_0^1 u_L d\eta$ and $\int_0^1 w_L d\eta$ with distribution of width-averaged Lagrangian velocity magnitude, $q_L = \left[\left(\int_0^1 u_L d\eta\right)^2 + \left(\int_0^1 w_L d\eta\right)^2\right]^{1/2}$ . . . 42

3.5 Distribution of a solute, initially filling the canal from $x = 0.5$ to $x = 1$, for $\beta = 0.42$, $\beta = 0.28$, and $\beta = 0.14$, at $\tau = 0.48$ in the straight configuration, corresponding to experiments 5, 3 and 1 of Table 3.1, respectively. Experimental results are represented on the left-hand side of the panels while the theoretical predictions obtained integrating Equation (2.4) are represented on the right-hand side. Here, N and W indicate the location of the narrowest and widest sections in the experimental visualizations. 43

3.6 Temporal evolution of the solute along the spinal canal for $\alpha = 4.39$ and $\beta = 0.14$, 0.28 and 0.42 respectively (experiments 1-6 in Table 3.1). Symbols represent the experimental measurements and the solid lines the results given by the theoretical model with $\gamma = 1$. 44

3.7 a) Contours of the axial component of the Lagrangian velocity, u_L, at the entrance of the canal, $x = 0$, for different values of β, provided by the theoretical model. b) Time taken by the solute to travel from $x = 0.45$ to $x = 0.05$ as a function of β, defined as τ_c. Symbols correspond to the experimental measurements and the solid line represents the model predictions with uniform compliance $\gamma = 1$. 46

3.8 Experimental measurements of the temporal evolution of the solute concentration in the cranial vault, $\langle C\rangle(\tau) = 1/A \int_A C\, d\sigma$, for $\alpha = 4.39$ and $\beta = 0.14$, 0.28 and 0.42 respectively (experiments 7, 9 and 11 in Table 3.1). 47

3.9 Distribution of a solute, initially filling the canal from $x = 0.5$ to $x = 1$, for $\alpha = 3.04$, 6.80, 9.61 and 11.77 where $\beta = 0.42$ in the straight configuration, corresponding to experiments 13-16 of Table 3.1. Experimental results are represented on the left-hand side of the panels while the theoretical predictions obtained integrating Equation (2.4) are represented on the right-hand side. 48

3.10 Temporal evolution of the solute along the spinal canal for $\beta = 4.2$ and $\alpha = 3.04$, 6.80 and 9.61 and 11.77 respectively (experiments 13-16 in Table 3.1). 49

3.11 Dependence of the time taken by the solute, initially located at $x = 0.5$, to travel from $x = 0.45$ to $x = 0.05$, τ_c, with α. Symbols represent the experimental measurements and solid lines the model predictions obtained for $\gamma_1 = 1$ and $\gamma_2(s) = 0.2 - 9.6\,(2s^2 - s)$, respectively. Here $\beta = 0.42$. 50

3.12 Time sequence of the evolution of a solute along a curved canal of unperturbed thickness $\bar{h}(x, s) = 1 - \beta\cos(2\pi x)\cos(2\pi s)$, with $\beta = 0.5$, initially filling the canal from $x = 0.5$ to $x = 1$,corresponding to experiment 17 of Table 3.1. Experimental results are represented on the left-hand side of the panels while the theoretical predictions obtained integrating Equation (2.4) are represented on the right-hand side. 51

3.13 a) Temporal evolution of the solute along a constant eccentricity canal of $\beta = 0.42$ (experiment 5 in Table 3.1), and a canal whose eccentricity varies with x as $\beta \cos(2\pi x)$, with $\beta = 0.5$ (experiment 17 in Table 3.1), for $\alpha \approx 4.4$. Symbols represent the experimental measurements and the solid lines the results given by the theoretical model with $\gamma(x, s) = 1$. b) Experimental measurements of the temporal evolution of the solute concentration in the cranial vault, $\langle C \rangle(\tau) = 1/A \int_A C \, d\sigma$, for the constant and the variable eccentricity canals (experimental sets 11 and 18 respectively in Table 3.1). 52

4.1 a) Scheme of the flow around a cylindrical post confined between two parallel plates, including the corresponding variables. b) Top schematic view of the oscillatory fluid flow around a linear array of cylindrical posts, separated a distance $2d$ among each other. 57
4.2 Schematic view of the full experimental facility (experimental model, programmable peristaltic pump and open-air container) and the image acquisition setup (YAG laser and CCD camera). 58
4.3 Steady pathlines (top row) and velocity + vorticity fields (bottom row) of the fluid around a single cylindrical post at different values of α. Left side of each panel corresponds to the experimental measurements ($\varepsilon = 0.2$) and right side to the analytical predictions ($\varepsilon \ll 1$). 61
4.4 Steady flow patterns (left) and corresponding velocity and vorticity fields (right) of the flow around a cylindrical element at different values of α (subcritical flow on the left column and supercritical flow on the right column) and ε (theory approximation corresponds to the top row and order-unity values correspond to the bottom row). 62
4.5 a) Harmonic flow waveform ($t_1 = t_2 = \pi$). b) Realistic flow waveform, obtained through MRI measurements and set as Fourier expansion ($t_1 \neq t_2$). Here, $t = 2\pi t^*/T$ represents the dimensionless time with $T = 1/f = 2\pi/\omega$ is the period of the waveform. 63
4.6 Steady pathlines of the flow around an obstacle confined between two parallel walls at different values of α and $\varepsilon = 0.2$. Top row corresponds to the tracking lines obtained with a harmonic waveform and bottom row corresponds to the tracking lines obtained through realistic flow motion. 64
4.7 Steady fluid particles trajectories around a cylindrical post for different cases of α and ε, obtained with subject-specific CSF waveform. 64
4.8 Steady flow patterns around a linear array of cylindrical posts separated by $\ell = 2$ at different values of α (columns) and ε (rows), induced by a harmonic waveform. 65
4.9 Steady pathlines of the flow around a cylinder at different values of α for $\varepsilon = 0.2$, induced by a patient-specific waveform. 66
4.10 Particle pathlines of the steady flow around a cylindrical post for different values of α and ε, with a realistic CSF waveform. 66

5.1 a) Scatter plot of values of the Womersley number (α) and stroke length-to-aqueduct length ratio ($\Delta L/L$) for 77 healthy volunteers participating in an IRB-approved study at HMRI, as reported elsewhere [79]. Distribution of these values for b) α and c) $\Delta L/L$. 72

5.2 a) Geometry of the cerebral aqueduct, extracted from Magnetic Resonance Images (MRI) b) Schematic view of the complete *in vitro* model: both reservoirs, the latex balloon and the duct which represents the aqueduct (the presented model corresponds to the canonical geometry, provided at [72]. In addition, the differential pressure transducer is also represented. c) Scheme of the different geometries of the cerebral aqueduct with the corresponding dimensions (left), frontal view of the *in vitro* model (middle) and input flow rate waveforms, divided into the CSF real flow (right-up) and a harmonic waveform (right-down). . 74

5.3 Dimensionless interventricular pressure $\Pi(t)$ corresponding to $\alpha = 2$ and $\Delta L/L = 1$ as determined from the previously published mathematical model [72] (top) and from the experimental measurements (bottom) for the cylindrical aqueduct ($a/L = 0.062$) with sinusoidal flow rate $\bar{Q} = \frac{1}{2}\sin t$ (a) and with the PC-MRI flow rate (b). Each plot includes an indication of the associated time-averaged pressure difference $\langle|\Pi|\rangle$ and phase lag φ. 79

5.4 The variation with $\Delta L/L$ of the time-averaged magnitude of the pressure difference $\langle|\Pi|\rangle$ and phase lag φ for $\alpha = 2$ (blue) and 4 (red) as measured with three different glycerol-water mixtures (viscosity values are indicated in the labels) in experiments using a harmonic flow rate along with a circular cylinder as a canonical representation of the aqueduct (hollow symbols: $a/L = 0.096$, solid symbols: $a/L = 0.062$). 80

5.5 The variation with $\Delta L/L$ of the time-averaged magnitude of the pressure difference $\langle|\Pi|\rangle$ and phase lag φ for $\alpha = (2, 3, 4)$ as measured with three different glycerol-water mixtures (see labels in Figure 5.4) in experiments using an anatomically correct aqueduct shape (top left inset) together with a) a harmonic flow rate and b) an MRI-measured flow rate. 81

List of Tables

3.1 Experimental conditions of the different sets of experiments performed. Here, β is the relative eccentricity, f is the oscillatory frequency of the motion, with $\omega = 2\pi f$, $\alpha = \left(h_c^{*2}\omega/\nu\right)^{1/2}$ is the Womersley number, $\Delta V/V \ll 1$ is the ratio between the stroke volume and the total volume in the canal, f_s is the data acquisition frequency, *Str* is straight configuration, *Curv* is curved configuration, and *CV* is cranial vault. . 40

4.1 Experimental conditions of the different sets of experiments performed. Here, $\alpha = \left(a^2\omega/\nu\right)^{1/2}$ is the Womersley number, f is the oscillatory frequency of the motion, with $\omega = 2\pi f$, U_∞ is the peak velocity of the CSF motion for the harmonic waveform, and the harmonic equivalent peak velocity of the CSF motion for the anharmonic waveform, and $\varepsilon = \left(U_\infty/\omega\right)/a$ is the small parameter. The waveform indicated as 'Sine' is a harmonic wave and that indicated as 'MRI' corresponds to an anharmonic cardiac signal obtained from Magnetic Resonance Imaging. 59

5.1 Differential pressure transducer configuration 76

5.2 List of experiments conducted for each geometry ('CS' for *canonical short*, 'CL' for *canonical long* and 'RE' for *real geometry*) and viscosity value with corresponding frequency $\omega/2\pi$ (expressed in beats per minute, BPM) and sampled range of dimensionless stroke length $\Delta L/L$ (increments of $\Delta\left(\Delta L/L\right) = 0.1$). The α value determined for each mixture and where measurements were made 3 separate times is given in bold. 77

Chapter 1

Introduction

1.1 General context and motivation

The cerebrospinal fluid (CSF) is a colourless liquid which surrounds the entire surface of the Central Nervous System (CNS). This fluid is generated from blood plasma in the cerebral ventricles with similar composition, but exempt of proteins and red blood cells in healthy patients [1], [2]. In physical terms, it behaves as a Newtonian liquid with close-to-water properties at normal body temperature (37^oC), being the density and kinematic viscosity equal to $\rho = 10^3$ kg/m^3 and $\nu = 0.71 \times 10^{-6}$ m^2/s, respectively.

The total volume of CSF varies in accordance with several parameters, such as sex, age and others. Despite this variability, the total volume of CSF in human adults can be estimated between 140 mL and 170 mL. As seen in Figure 1.1, this total volume is distributed between different spaces, being the cerebral ventricles (V) the region with less CSF inside ($V_V \simeq 30$ mL), followed by the subarachnoid spaces or SAS ($V_{SAS} \simeq 120$ mL), also divided into the spinal subarachnoid space, the SSAS ($V_{SSAS} \simeq 40 - 60$ mL), and the cerebral subarachnoid space, the CSAS ($V_{CSAS} \simeq 70 - 80$ mL) [3]. This volume is renewed due to the continuity fluid balance between the CSF production and absorption in the arachnoid villi, requiring $5 - 6$ h approximately to be completely renovated [1], [4].

The presence of CSF has acquired clinical interest over the years due to its properties, and its contribution to the welfare of the CNS. In this aspect, CSF presents a widespread variety of mechanical and physiological functions: on the one hand, CSF cushions the brain within the skull, so that it acts as a shock absorber which avoids severe injuries of the brain. Moreover, as the CNS is immersed in the CSF, the apparent weight of this body is considerably reduced (from an apparent weight of 1500 g on air to 50 g in CSF), being the average reducing factor 1/30, which also reduces the compression of the spinal cord [6]. On the other hand, the different physiological CSF functions guarantee the well-performance of the CNS, being mentioned below: firstly, CSF keeps the electrolytic environment of the CNS and maintains its systemic acid-based balance. In addition, CSF acts as the lymphatic system of the CNS due to the lack of lymph nodes in the CNS. Finally, the CSF is a well-known transport medium of substances, like hormones, nutrients and wastes from cell metabolism [7]–[10]. Regarding these properties, specifically the transport of substances between the CNS and the circulatory system, CSF yields clinical interest to deliver drugs, being a more effective way than the most common procedures, such as via oral, subcutaneous and intravenous, where medicines must get across the Blood-Brain Barrier (BBB), a biological barrier which avoids agent substances get directly into the CNS [11]. In order to surpass the BBB, there are several treatments in which the drug is injected

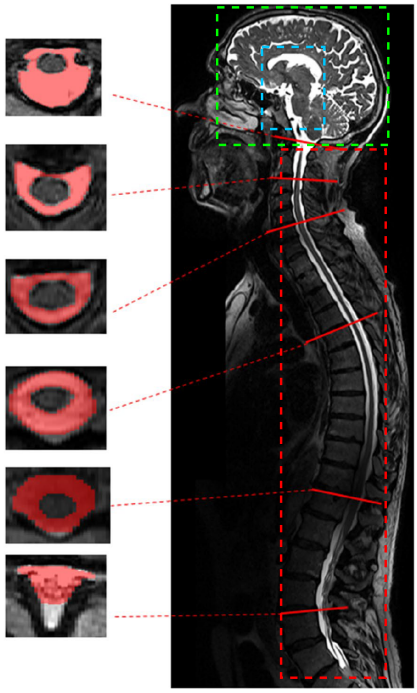

Figure 1.1: Total volume of the cerebrospinal fluid, distributed into the ventricles (blue box), the cerebral subarachnoid space (green box) and the spinal subarachnoid space with cross-sections at different levels (red box). Image extracted from Sass et al. [5].

directly to this space, such as the Ommaya reservoir [12], where the drug is delivered into the cranial cavity, and the intrathecal drug delivery (ITDD) [13], being the most common injection point the lumbar region of the SSAS, relevant for this dissertation. Indeed, these mechanisms result much more effective than the previously mentioned treatments since they do not get across the BBB, so that less quantity of drug is required. However, the widespread use of ITDD faces challenges related to underdosing and overdosing, with the former resulting in reduced therapeutic effects in the case of cancer treatments and the latter leading to permanent nerve damage in the case of pain medication [14].

As aforementioned described, normal CSF dynamics is necessary for the correct performance of the CNS: if these conditions change, CSF may cause dysfunctions or malformations in the space where it is contained with the corresponding development of neurological pathologies [15], [16], such as the Hydrocephalus (the enlargement of the ventricular space) [17] or obstructions in the entrance of the SSAS, like the Chiari Malformation Type 1 [18], which may induce syringomyelia (the presence of a syrinx inside the central canal of the spinal cord). Thus, it is essential to characterize the CSF flow dynamics, which provides a deeper understanding and allows to improve clinical procedures (i.e. ITDD) for a better living of people. In this aspect, CSF motion has been the subject of numerous theoretical, numerical, and *in vivo* and *in vitro* experimental studies (see, for example, the recent literature reviews given in Kelley et al. [19] and Linninger et al. [20]). These previous studies set the background of the present dissertation, being its main objective the characterization of the CSF motion in the SAS.

1.2 CSF flow in the spinal canal

The increasing interest of characterizing the CSF motion has been addressed from the 60s to nowadays, reported in several publications in clinical journals as well as in physics or engineering journals recently, which are collected in extended reviews, as is seen in Linninger et al. [20] and Kelley et al. [19], among others. These studies show that, in regard to the key role of CSF in the transport of substances between the CNS and the circulatory system, the CSF motion along the SSAS results an important topic to study, being the first objective of this dissertation.

Characterizing the CSF motion and solute transport is a non-straightforward aim due to its complexity. In anatomical terms, the SSAS is defined as a slender, compliant and annular canal, which surrounds the spinal cord. As shown in Figure 1.2, the spinal canal, which is connected to the cranial cavity through the foramen magnum and is closed at its distant sacral end, is bounded externally by the dura membrane, which separates it from an outer epidural layer containing fatty tissue and blood vessels which give its compliance, and internally by the pia membrane, which evolves the spinal cord. Regarding the fluid motion nature, the CSF flow along the SSAS is considered pulsatile with zero-averaged velocity component, predominantly aligned with the spinal cord. This pulse can also be divided into two different components synchronized with the cardiac and respiratory cycles, with peak values on the order of a few centimeters per second. The cardiac-driven motion, with a typical frequency of 1 Hz, is induced by pressure fluctuations in the cranial vault associated with the cyclic in-/outflow of arterial/venous blood [21]. During each cardiac cycle, a small CSF volume $\Delta V \simeq 1-2$ mL is pushed in and out of the SSAS through the foramen magnum. This stroke volume is accommodated by the displacement of the dura and pia membranes, with the local CSF pressure fluctuations related to the local changes in cross-sectional area of the SSAS through a complicated fluid-structure-interaction problem involving the displacement of venous flow and fatty tissue [20]. The cardiac-driven oscillatory flow rate is maximum near the foramen magnum and decays monotonically to zero at the sacrum, with typical peak values of order 5 mL/s in the upper cervical region and 1 mL/s in the lumbar region [21], [22].

Unlike the cardiac-driven motion, the flow component synchronized with the respiratory cycle [23], which exhibits frequencies on the order of 0.3 Hz, is not driven by the intracranial pressure fluctuations. Instead, its origin is hypothesized to lie in the pressure variations induced by respiration in the venous plexus, located in the epidural space of the lower thoracic and upper lumbar spine [24]. Recent magnetic resonance (MR) measurements performed under normal breathing conditions have revealed that the associated flow rates are maximum near the thoracolumbar junction ($1-3$ mL/s), and smaller in the cervical spine [25].

Apart from the aforementioned purely oscillatory motion, CSF also undergoes a slow steady motion characterized by small velocities on the order of a centimeter per minute. Unlike the oscillatory flow, this 'bulk motion' has the ability to transport solutes along the total distance of the SSAS, and therefore plays a key role in enabling the numerous physiological functions attributed to CSF. This bulk motion is also important in connection with the transport of drugs in ITDD procedures [27] as mentioned above, which is a technique used to administer pain, analgesic, and cancer medication where the drug is delivered directly into the CSF, typically through a lumbar puncture, thereby circumventing the BBB [13]. Nevertheless, as it has been

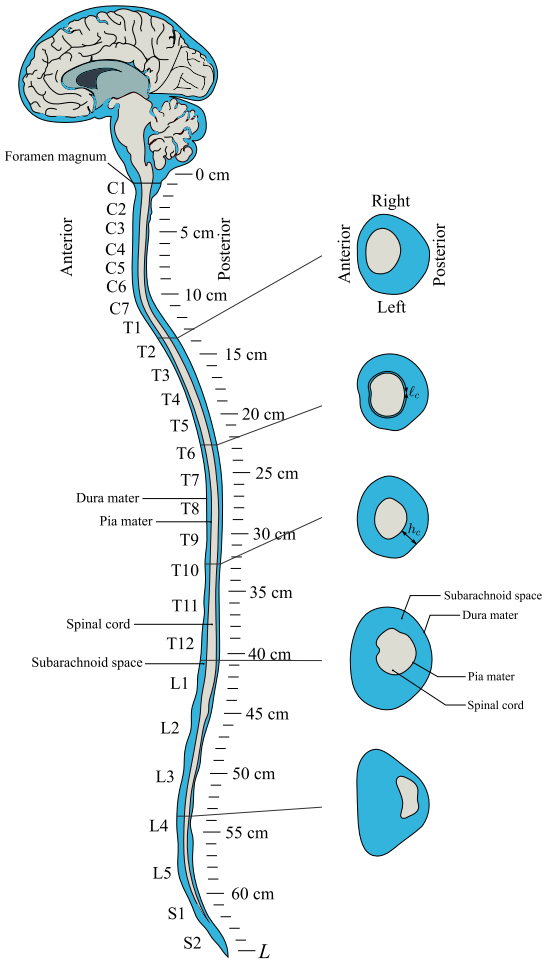

Figure 1.2: Anatomy of the SSAS of a healthy human with axial cuts at several locations and the CSF colored in blue. Extracted from Moral-Pulido et al. [26]

previously commented, the widespread use of ITDD faces important challenges and, thus, it is evident that a better understanding of the bulk motion of CSF in the SSAS is essential to enable optimized subject-specific ITDD protocols.

While the existence of bulk motion has been known since the seminal radiographic observations of Di Chiro [28], its physical origin has been unveiled only relatively recently [29]. The analysis considered a simplified model of the cardiac-driven oscillatory flow in agreement with the considerations described before. The associated Eulerian velocity field was computed using a perturbation analysis involving a small parameter ε representing the ratio $\Delta V/V \ll 1$ of the stroke volume $\Delta V \simeq 1-2$ mL to the total volume of CSF contained in the SSAS ($V \simeq 40-60$ mL). In the limit $\varepsilon \ll 1$, the velocity at leading order was found to be purely oscillatory, with a zero time-averaged value. By way of contrast, the first-order corrections, associated with the nonlinear convective acceleration, were found to contain a steady-streaming component that corresponds to the bulk flow observed in *in vivo* experiments. The theory was applied to a simplified geometry, which consisted of an annular doubly slender canal, open at the entrance and closed at the end (this steady component has also been studied with elliptical cross-section geometries in recent works [30]). Although complicating microanatomical features, such as nerve roots, dentriculate ligaments and trabeculae were not taken into account (see, for example, Refs. [21], [31]–[38]), the model did account for a key feature of the SSAS, namely, the eccentric placement of the spinal cord within the lumen of the spinal canal. The magnitude of the axial

streaming flow was found to depend critically on the level of eccentricity.

The analysis of Sánchez et al. [29] was extended in Lawrence et al. [39] to show that the mean Lagrangian velocity experienced by a fluid particle in the SSAS is the sum of the steady-streaming velocity, determined by time-averaging the Eulerian velocity field, and the so-called Stokes drift [40], a purely kinematic effect associated with the spatial nonuniformity of the pulsatile flow. One can understand the origin of the Stokes drift by noting that, in the presence of a velocity gradient, a fluid particle subject to an oscillating velocity field experiences during each oscillatory cycle an instantaneous velocity that differs by a small amount from that existing at the initial point at corresponding times. As a result, the fluid particle does not return to its original position at the end of the cycle. The Stokes drift arises as the result of the accumulation of displacements over subsequent cycles, yielding characteristic velocities that are comparable in magnitude to those of steady streaming. The asymptotic analysis performed in Lawrence et al. [39] also provided a reduced transport equation describing the dispersion of a solute carried by the CSF, with the mean Lagrangian velocity (i.e. the sum of the steady-streaming and Stokes-drift velocities) determining the convective transport rate in the long time scale characterizing dispersion along the spinal canal. The strength of the previous reduced models [29], [39] lies in the fact that they provide closed-form expressions for the time-averaged velocity field associated with the bulk motion, as well as simplified transport equations that describe the slow solute transport, which can be evaluated very efficiently, without the need to solve the flow over thousands of oscillation cycles, as is required in direct numerical simulations targeting solute dispersion along the spinal canal.

As mentioned before, the eccentricity of the spinal canal has an important effect on the Lagrangian motion, and hence on the transport of solutes in the spinal canal. As shown in Figure 1.2, in the human SSAS, this eccentricity changes longitudinally, as the spinal cord changes its position relative to the dura in the anteroposterior plane. Indeed in healthy humans, the spinal canal exhibits concavity variations in the sagittal plane stemming from the four main curves of the spine, i.e. two kyphoses, and two lordosis [41], characterized by the Cobb angles [42]. In adults, the spinal cord located inside the spinal canal extends cranially from the brain to nearly the end of the L1 region [41]. The spinal cord's relative position inside the SSAS varies along the canal [41], [43], as well as with posture [44], [45], which yields subject-specific spinal canal eccentricity variations. In particular, the spinal cord is located near the posterior side of the canal in the cervical region, but close to the anterior side in most of the thoracic region, shifting towards the posterior side again as it approaches the lumbar region [21], [32], [35], [43], [46]. This variable eccentricity has an important effect on the spatial structure of the Lagrangian motion, leading to the emergence of closed recirculating regions. These recirculating Lagrangian vortices have been computed on theoretical grounds for a realistic patient specific geometry [22] and were corroborated in an idealized geometry by means of direct numerical simulations [47]. The existence of these Lagrangian recirculating regions can have a strong clinical impact, since they modulate the rate of transport with which a drug injected intrathecally in the lumbar region is transported to the cranium. The presence of closed Lagrangian streamlines leads to augmented solute residence times in certain regions, thereby possibly increasing the risk of local overdose in ITDD procedures. All these analytic-numerical works have been complemented with *in vitro* works [48]–[52], where different types of *in vitro* models have been evaluated, ranging

from an idealized channel with a simplified flow waveform [48] to realistic patient-specific geometries with real CSF flow rates [49], [50], which lead to promising results. However, these studies deal with rigid canals that are open at both ends, and do not directly address the role of the compliant dura membrane and the associated fluid-structure interaction problem, an important aspect of the CSF dynamics in the SSAS.

Motivated by the clinical relevance of solute transport in the spinal canal, this dissertation pretends to enlighten, in part, the understanding of the CSF motion along this region. Thereby, and following the previous developed models of the CSF motion and solute transport [29], [39], [47], efforts are made in understanding the effects of the main governing parameters of the CSF flow, divided into the geometrical aspects of the canal, the flow conditions and the elastic properties of the SSAS, exploiting the analytical model on the one hand, and experimentally on the other hand. In addition, an initial study to characterize the effect of the microanatomy in the SSAS is carried out through *in vitro* measurements, following recent works wherein an array of elements immersed in an oscillatory field is considered [38]. Results of this work will allow to clarify and optimize the ITDD protocols, yielding an improvement in people lives.

1.3 CSF flow in the cerebral aqueduct

Apart from the investigation of the CSF motion and solute transport along the SSAS, there is also clinical interest in characterizing its motion in other spaces, i.e. the CSF motion in the cranial cavity, with remaining interest in clinical applications. Indeed, the slow steady flow of CSF occurs in this region between the ventricles (CSF is mainly produced in the choroid plexus) and the SAS, from which it exists via multiple pathways [53], [54]. In addition to this slow motion, the oscillatory component of CSF motion is also important, being driven by the spatial pressure differences induced by the cardiac and respiratory cycles [19], [20], [55]–[57]. In the cranial cavity, the largest velocities and, therefore, the largest pressure drops are found in the cerebral aqueduct, consisting of a narrow passage of length $L \sim 10 - 15$ mm and average radius $a \sim 1 - 1.5$ mm, which connects the third and fourth ventricles [20], [58]. These velocities have clinical potential value in investigating the development of Normal Pressure Hydrocephalus (NPH) [59]–[62] and understanding the effects of different treatments like shunting [63], [64] or lumbar puncture [65].

One closely related parameter of clinical interest is the transmantle pressure, defined as the instantaneous pressure difference between the lateral ventricles and the SAS, which are connected by the foramina of Monro (lateral ventricles and third ventricle), the cerebral aqueduct or aqueduct of Sylvius (third and fourth ventricles) and the foramina of Magendie and Luschka (fourth ventricle and SAS), as can be seen in Figure 1.3(a) and (b). Although there are different passages wherein CSF oscillates, the maximum pressure drop occurs across the cerebral aqueduct or aqueduct of Sylvius (see Figure 1.3c) [66], [67]. Therefore, a good approximation to evaluate this phenomena is using the trans-aqueductal pressure difference, i.e. the pressure difference between the third and fourth ventricles $\Delta p_{aq}(t^*) = p_3 - p_4$, to characterize the transmantle pressure difference. The value of $\Delta p_{aq}(t)$, of order of a few pascals, fluctuates from positive to negative about a negligibly small time-averaged value [68], being these fluctuations the mechanism of the oscillatory flow across the aqueduct,

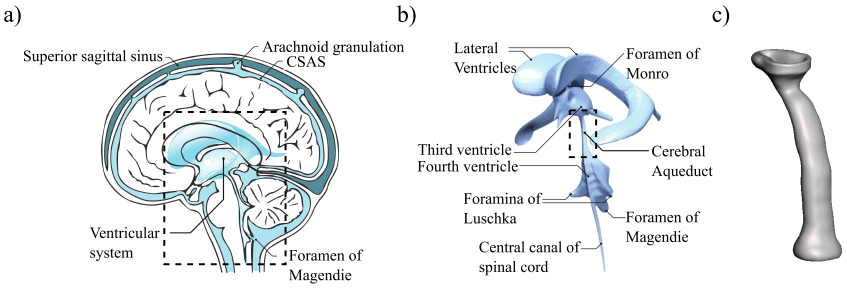

Figure 1.3: a) Schematic view of the CSAS and the cerebral ventricular system (extracted from Sincomb et al. [72]). b) Schematic view of the cerebral ventricular system (BodyParts3D, ©The Database Center for Life Science licensed under CC Attribution-Share Alike 2.1 Japan). c) 3D model of the cerebral aqueduct.

with associated peak volumetric rates $Q_{aq}(t^*) \sim 0.1$ mL/s [69]–[71].

Despite being small the corresponding mean force that the transmantle pressure exerts on the brain [68], this pressure difference has been argued to play a role in the ventricle enlargement characterizing NPH patients [73]: the cyclic strain field acting on the brain parenchyma over a long time is supposed to change the brain viscoelastic properties in NPH patients with altered CSF flow dynamics [74]. Accordingly, not only the transmantle pressure, but also the phase lag between $\Delta p_{aq}(t^*)$ and the flow rate $Q_{aq}(t^*)$ has been investigated due to its potential clinical relevance in NPH patients [75], which underscores the implications of the waveforms involved in aqueduct flow.

As aforementioned, knowing the values of the transmantle pressure becomes relevant in diagnosing possible disorders. However, obtaining these direct measurements of the transmantle pressure requires accurate simultaneous readings from two separate high-resolution pressure sensors [76], an invasive surgical procedure with considerable risk factors [77]. By contrast, several efforts have been focused on characterizing this pressure by a non-invasive procedure. In fact, as the intraventricular pressure difference $\Delta p_{aq}(t)$ drives the flow along the aqueduct, its value can be inferred from non-invasive MRI measurements of the oscillatory aqueduct flow rate $Q_{aq}(t)$ [67], being the pressure differences associated with the cardiac-driven flow about four times larger than those associated with respiration [76]. Thus, different models have been developed for the relation between $\Delta p_{aq}(t)$ and $Q_{aq}(t)$ by solving the Navier-Stokes equations inside the cerebral aqueduct [67], [72], [78], needed to enable estimates of the former from measurements of the latter [79]. In this aspect, a recent work of Sincomb et al. [72] shows that accurate predictions require consideration of effects of flow acceleration as well as pressure losses at the nearly inviscid entrance regions connecting the aqueduct with the ventricles.

The evaluation of the transmantle pressure through the non-invasive techniques, represented by previously mentioned models, has been performed through *in vivo* investigations of aqueduct flow using MR techniques, wherein the associated flow rates and stroke volumes have been quantified (see, e.g. [55], [57] and references therein). Besides, more detailed quantitative information has been acquired in different computational investigations [80]–[83] and also in *in vitro* experimental studies of aqueduct flow [84]–[87]. The latter type of studies have focused, in particular, on the characterization of the flow in the third ventricle of an anatomically correct *in vitro* models, using either particle tracking velocimetry (PTV) combined with phase contrast (PC)

MRI [84] or particle image velocimetry (PIV)[85], being related the latter study to steady flow, which is not representative of the markedly unsteady conditions found in the human aqueduct, for which resulting Strouhal numbers are of order unity [72]. Whereas the *in vitro* anatomically-sized analyses require high-resolution devices to properly measure the variables, scaling up the model is a good way to avoid such small ranges and to improve the quality in measurements. To that end, the phantom study of Schibli et al. [84] uses a scaled-up model, with physical similarity accounted for by modifying the properties of the working fluid. Their analysis, imposing a pressure difference varying sinusoidally in time, identified many interesting features pertaining to the unsteady flow in the third ventricle. These early studies, specifically targeting the ventricular flow structure, were followed by the *in vitro* study of Bottan et al. [86], who were able to provide simultaneous measurements of the intracranial pressure fluctuation, aqueduct pressure drop, and aqueduct flow rate driven by the cardiac cycle by using a life-size model of the entire cranial domain. Their phantom model, with clear potential for extensive measurements of physiologically relevant quantities, was used to generate a single set of representative waveforms, yielding shapes that did not fully match those obtained on healthy subjects [86], departures being attributed to limitations in the bandwidth of the actuation system. In a more recent study, Holmlund et al.[87] performed benchtop aqueduct experiments of unsteady flow in a simplified aqueduct model with a realistic flow rate driven by a syringe pump. Corresponding intraventricular pressure differences were measured and associated time-averaged values of about 0.5 Pa were computed, but corresponding pressure fluctuations and relative flow-rate/pressure-gradient phase lags, both of clinical interest, were not reported.

All these previous works have set the background of the work presented in this dissertation. Here, an *in vitro* work is conducted to complement these previous studies by providing a more detailed parametric description of the intraventricular pressure difference under biological ranges in healthy subjects. Following the initial steps in characterizing the CSF flow in the cerebral aqueduct presented in Sincomb [88], this dissertation reports results of an *in vitro* study conducted in a scaled up and anatomically correct model, keeping physical similarity, whose results are validated with predictions obtained using the previously published theoretical model [72]. This study provides a thorough description of the relation between the flow rate and the intraventricular pressure difference. The new information can be useful in designing future protocols for quantification of transmantle pressure differences based on non-invasive phase contrast (PC) MRI measurements.

1.4 Outline of the dissertation

The present dissertation is divided into three different parts. Part I considers the characterization of the steady CSF flow in the SSAS. To that end, Chapter 2 extends the study of the flow field in the spinal canal for a canonical geometry developed in previous works [29], [39], [47] to evaluate the different effects induced by the governing parameters of the flow, relating to the geometrical aspects, as well as the flow frequency and the elastic properties of the canal. Such study exploits the biological ranges of the main parameters and describes the different flow topologies which can be present in the SSAS, as well as it establish the relationships among parameters. Following this parametric study, Chapter 3 characterizes the CSF flow and solute transport in an *in vitro* facility, where the eccentricity and the flow frequency are

evaluated. These experiments, which consider the fluid-structure interaction problem by integrating the induced CSF motion through the wall displacement, thank to the flexibility of the wall itself, have been performed by the use of laser induced fluorescence techniques (LIF), and include the advance of the solute along the canal and the temporal variation of the solute concentration inside the brain, which has clinical impact in ITDD procedures.

Extending the analysis of the flow field in the spinal canal, Part II includes an additional effect related with the microanatomy of the SSAS, such as nerve roots or trabeculae, which are emulated by cylindrical posts. This effect is experimentally evaluated in Chapter 4 in an *in vitro* simplified facility, thanks to the disparity of geometrical scales (the radial component is quite smaller than the azimuthal component). To that end, it is considered that the curvature near the microanatomic element is negligible, so that the steady flow surrounding a cylindrical post inside a planar confined canal becomes the new problem to study at first. As done in Part I, an analysis of the governing parameters is performed including the flow frequency and the stroke volume (here, the stroke length of the CSF motion reaches values of order of the diameter of the post). The study assumes a harmonic flow waveform first, and is subsequently extended to consider a real CSF waveform, obtained from magnetic resonance imaging (MRI) measurements, which presents differences in the steady flow patterns from those obtained for the harmonic waveform. Finally, the analysis is also extended to account for the presence of multiple elements, to emulate the effect of a bundle of nerves in the spinal canal.

After characterizing the CSF flow along the SSAS, Part III presents the characterization of the CSF flow in the cranial region. In particular, the problem focuses on the experimental characterization of the CSF dynamics in the cerebral aqueduct, a narrow canal connecting the third and fourth ventricles, where the CSF flow is believed to be intimately connected with the development of disorders, such as NPH. To that end and following the previous works, where it is modelled analytically, Chapter 5 reports an *in vitro* study where the transaqueductal pressure and the flow rate are experimentally characterized in order to establish the relationship between both signals. This work sets the basis of the development of non-invasive techniques to measure the transmantle pressure and to detect possible pathologies in patients. Finally, Chapter 6 summarizes the main conclusions of this dissertation and introduces some ideas for future works.

Part I

Characterization of the CSF flow in the spinal canal

Chapter 2

Parametric study of the CSF motion and solute transport along the spinal canal

We present a parametric analysis of the CSF motion and the transport of a neutrally buoyant solute along the SSAS. In this analysis, the parametric dependence of the Lagrangian velocity field and the solute transport is evaluated in a canonical model of the spinal canal, which consists of an eccentric, slender and annular canal, delimited internally by a rigid wall, the pia mater, and externally by a flexible membrane, the dura membrane, both modelled as surfaces of circular cross section of constant radii. The evaluated parameters in this analysis are related to the geometry of the canal, namely, the relative eccentricity, $\beta = e_v/h_c^*$, where e_v is the distance between the axis of the inner and outer walls of the canal and h_c^* is the characteristic radial width of the spinal canal, the flow, through the Womersley number $\alpha = h_c^*/\left(\nu/\omega\right)^{1/2}$, with ν the kinematic viscosity of the fluid and $\omega = 2\pi f$ the angular frequency of the pulsatile flow, and the canal compliance, characterized by the dimensionless wave number, $k = L\omega/\left[\left(h_c^*/\gamma_c^*\right)/\rho\right]^{1/2}$, where L is the length of the canal, γ_c^* the characteristic compliance of the flexible wall and ρ the density of the CSF. Results of this study show different flow topologies of the time-averaged Lagrangian velocity as a function of α. For low values of α, the flow moves upwards along the narrowest region of the canal and downwards along the widest region of the canal, whilst this flow configuration changes for increasing values of α, for which the upward motion is found to occur along the widest region of the canal and the downward motion along the narrowest one, for $\alpha > 10$. The transition between flow configurations and the eigen steady flow patterns differ with the rest of the parameters, giving a wider understanding of the CSF motion and the corresponding solute transport.

This chapter is comprised, in part, in the paper: "In vitro characterization of solute transport in the spinal canal", by F. Moral-Pulido, J.I. Jiménez-González, C. Gutiérrez-Montes, W. Coenen, A. L. Sánchez & C. Martínez-Bazán, published in Physics of Fluids (2023).

2.1 Introduction

The CSF is a close-to-water Newtonian fluid, located in the CSAS and SSAS. This liquid presents important mechanical and physiological functions, necessary to maintain an adequate performance of the CNS. In addition, CSF serves as a vehicle to transport drugs administered via direct injection inside the spinal canal, commonly known as ITDD. Given their importance, a comprehensive understanding of these

problems results paramount, for example in the design of medical protocols, in optimizing the effectiveness of the existing procedures or in reducing the associated risks. In that regard, many efforts in different disciplines have been made in previous works, collected in several compilations [19], [20], [35]. In particular, Sánchez et al. [29] and Lawrence et al. [39] developed models of the Eulerian and Lagrangian velocity fields, as well as the transport of a solute along the SSAS. The latter have been validated through comparison with numerical simulations [47] and *in vitro* experiments [26]. In these studies, although the results show the dependence of the fluid variables on the main parameters of the problem, no complete parametric analysis has been conducted. To that end, the present study aims to comprehensively extend the previous results by broadening the range of parameters of interest and describing the role they play in CSF movement and solute transport.

In the following, we briefly describe the CSF Eulerian and Lagrangian motion and the solute transport along the spinal canal, in accordance with the mathematical model, developed by Sánchez et al. [29], Lawrence et al. [39] and Gutiérrez-Montes et al. [47]. Once the flow and transport are described, details of the computations of the model are provided, including the ranges of the governing parameters. Finally, results of the velocity field and the solute transport are presented covering a wide range of parameters considering both, a straight SSAS geometry and a curved one.

2.2 Problem Description

The flow of CSF in the SSAS fundamentally involves a fluid-structure-interaction problem governed by the Navier-Stokes equations for an incompressible fluid, together with a constitutive law characterizing the deformable dura membrane behaviour. In addition, to describe the transport of a solute of molecular diffusivity κ, the species transport equation should also be solved [39], [47]. In previous works [29], [39], the flow and transport of the CSF along the spinal canal was described in terms of dimensionless curvilinear coordinates, including the normalized axial and azimuthal coordinates $x = x^*/L$ and s, where x is the distance from the canal entrance normalized with the canal length and s is the azimuthal distance normalized with the perimeter of the pia mater $\ell^*(x)$, along with the transverse coordinate η, defined as the transverse distance to the inner surface normalized with the local width, $h^*(x, s, t)$, so that all coordinates vary from zero to unity (see Figure 2.1). Here, $t = t^*\omega$ represents the dimensionless time and the variables with asterisks denote dimensional variables. Since a detailed derivation of the reduced-order equations is available in previous publications [29], [39], we shall only give below a succinct description of the model.

In the analysis, the cranial pressure oscillations are assumed to be harmonic, described by $(\Delta p)_c \cos(t)$, with $(\Delta p)_c$ representing the intracranial pressure-fluctuation amplitude. Since the canal is slender, in that the characteristic values of the canal length L, spinal-cord perimeter ℓ_c^*, and characteristic SSAS width h_c^* satisfy $L \gg \ell_c^* \gg h_c^*$, terms of order $(\ell_c^*/L)^2$ and $(h_c^*/L)^2$ (and smaller) can be neglected in the conservation equations, as well as those associated with the small curvature along the spinal canal (see Sánchez et al. [29]). The small local deformations δh^* of the canal width $h^* = \bar{h}^* + \delta h^*$, induced by the local pressure variations δp^*, are described using a linear elastic model $\delta h^* = \gamma^* \delta p^*$, where γ^* measures the canal compliance [21], [39], [47] and whose spatial variations are accounted for by the introduction of the dimensionless function $\gamma(x, s) = \gamma^*/\gamma_c^*$, where γ_c^* is the characteristic value of

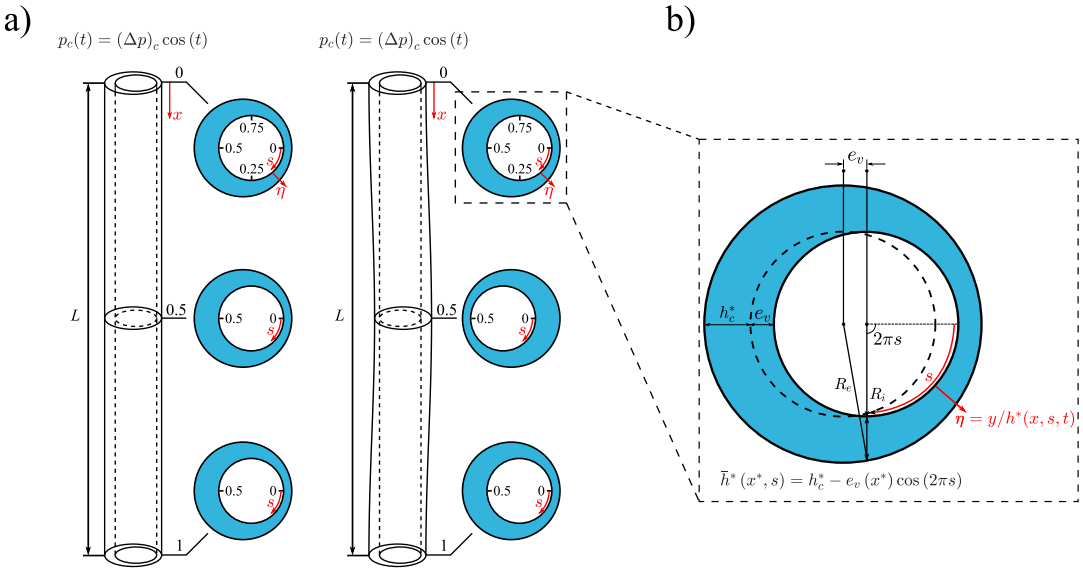

Figure 2.1: Schematic view of the geometry of the spinal canal with their corresponding variables, according to Sánchez et al.[29]. Here, a) shows a straight one of constant eccentricity (left) and a curved one whose eccentricity varies along the canal (right). b) Cross section of the canal.

γ^*. The canal compliance is limited, in that

$$\varepsilon = \frac{\gamma_c^*(\Delta p)_c}{h_c^*} \simeq \frac{\Delta V}{V} \approx \frac{\Delta L}{L} \ll 1, \tag{2.1}$$

where ΔL is the characteristic value of the stroke length.

An order-of-magnitude of the Navier-Stokes equations shows that the convective acceleration, of order u_c^2/L is ε smaller than the local acceleration, of order ωu_c, where $u_c \sim \omega\,\Delta L \sim \varepsilon\omega L$ is the characteristic axial flow velocity. The viscous force per unit mass, of order $u_c\nu/h_c^{*2}$, scales in the dimensionless formulation with the inverse of α^2, where

$$\alpha = \left(\frac{h_c^{*2}\omega}{\nu}\right)^{1/2}, \tag{2.2}$$

is the relevant Womersley number, typically in the range $3 \lesssim \alpha \lesssim 10$. On the other hand, the deformable behaviour of the dura membrane is characterized by the dimensionless wavenumber

$$k = \frac{\omega L}{[(h_c^*/\gamma_c^*)/\rho]^{1/2}}, \tag{2.3}$$

representing the ratio between the canal length and the characteristic wavelength of the elastic wave or, in other words, the ratio between the characteristic velocity, ωL, and the characteristic elastic wave speed, $[(h_c^*/\gamma_c^*)/\rho]^{1/2}$.

In the dimensionless formulation [29], [39], the geometry of the canal is characterized by the dimensionless functions $\ell(x) = \ell^*/\ell_c^*$ and $h(x,s,t) = h^*/h_c^*$. The limited compliance of the dura membrane leads to small changes of the canal width $h(x,s,t) = \bar{h}(x,s) + \varepsilon h'(x,s,t)$, where $\bar{h}(x,s)$ is the unperturbed canal width and $h'(x,s,t)$ represents the time-dependent radial deformation. The streamwise, azimuthal and traverse components of the velocity are scaled with their corresponding characteristic values, namely $u_c = \varepsilon\omega L$, $w_c = \varepsilon\omega\ell_c^*$, and $v_c = \varepsilon\omega h_c^*$, respectively, to

give (u, w, v). In addition, the streamwise pressure difference from the entrance value is scaled with its characteristic value $\rho\varepsilon\omega^2 L^2$, whereas the small pressure variations around the canal at a fixed value of x, which are necessary to describe the azimuthal motion, are scaled with its corresponding characteristic value $\rho\varepsilon\omega^2\ell_c^{*2}$ to give the functions $p'(x,t)$ and $\hat{p}(x,s,t)$, respectively.

The problem can be solved under the assumptions of canal slenderness $L \gg \ell_c^* \gg h_c^*$ and small compliance $\varepsilon \ll 1$, by introducing regular asymptotic expansions in powers of ε for all variables (i.e. $\phi = \phi_0 + \varepsilon\phi_1 + \varepsilon^2\phi_2 + ...$, with ϕ representing any unknown function). The non-linear terms associated with convective acceleration, of order ε, can be neglected at leading order, leading to a linear unsteady lubrication problem involving a linear elastic law, the solution of which depends on the specific geometry of the spinal canal through the functions $\ell(x)$ and $h(x,s,t)$, on the dimensionless elastic-wave number k and the Womersley number, α, and on the compliance distribution, measured by the function $\gamma(x,s)$. The resulting velocity components and wall deformation can be expressed in the harmonic form $u_0 = Re(iUe^{it})$, $w_0 = Re(iWe^{it})$, $v_0 = Re(iVe^{it})$, and $h_0' = Re(H'e^{it})$, where U, W, V, and H' are complex functions carrying the spatial dependence. Since at leading order the time-averaged values are zero, it is the first-order corrections, arising from the non-linear effects associated with the convective acceleration and the canal deformation, that induce a nonzero steady component (u_{SS}, w_{SS}, v_{SS}). This steady-streaming motion [89] has longitudinal velocities that are of order $\varepsilon^2\omega L$, resulting in residence times in the spinal canal of order $\varepsilon^{-2}\omega^{-1} \gg \omega^{-1}$. Since $\varepsilon \sim 1/40$, it follows that the residence time is about half an hour, to be compared with the period of the cardiac cycle (i.e. $T \simeq 1$ s).

As shown in Lawrence et al. [39], the mean Lagrangian motion following a fluid particle has an additional component arising from the so-called Stokes drift, whose magnitude is comparable to that of the steady-streaming velocities, so that the mean Lagrangian velocity determining the slow convective transport of the solute in the spinal canal is given by $(u_L, v_L, w_L) = (u_{SS} + u_{SD}, v_{SS} + v_{SD}, w_{SS} + w_{SD})$. The dispersion of the solute includes an additional diffusion contribution that scales with the solute molecular diffusivity κ. The disparity of time scales between the oscillatory motion of CSF particles, with characteristic time ω^{-1}, and the time-averaged Lagrangian motion, with characteristic time $\varepsilon^{-2}\omega^{-1}$, enables a two-time-scale asymptotic analysis to be performed, leading to a reduced transport equation,

$$\frac{\partial C}{\partial \tau} + u_{\mathrm{L}}\left(\frac{\partial C}{\partial x} - \frac{\partial \bar{h}}{\partial x}\frac{\eta}{\bar{h}}\frac{\partial C}{\partial \eta}\right) + \frac{v_{\mathrm{L}}}{\bar{h}}\frac{\partial C}{\partial \eta} + \frac{w_{\mathrm{L}}}{\ell}\left(\frac{\partial C}{\partial s} - \frac{\partial \bar{h}}{\partial s}\frac{\eta}{\bar{h}}\frac{\partial C}{\partial \eta}\right) = \frac{1}{\alpha^2\varepsilon^2 S\bar{h}^2}\frac{\partial^2 C}{\partial \eta^2}, \tag{2.4}$$

for the solute concentration $C(x,s,\eta,\tau)$ involving the slow time variable $\tau = \varepsilon^2 t$ and the Schmidt number $S = \nu/\kappa \sim \varepsilon^{-2} \gg 1$. Note that, since Equation (2.4) only accounts for transverse molecular diffusion, the streamwise dispersion of the solute is driven entirely by convective transport. The above simplified description, whose accuracy was tested in Gutiérrez-Montes et al. [47] via comparisons with results of direct numerical simulations, will be used below for generating theoretical predictions, to be compared with the experimental results in Chapter 3.

2.3 Results

The effect of the governing parameters on the solute transport are investigated below. Two different canal geometries will be explored in this chapter. The first one is a constant eccentric canal, consisting of two eccentric cylinders, whose unperturbed canal width is given by $\bar{h}(s) = 1 - \beta\cos(2\pi s)$ where $\beta = e/h_c^*$, with e the distance between the axis of the inner and outer cylinder (see the left side of Figure 2.1a). The second one is a variable eccentric geometry of unperturbed width $\bar{h}(x, s) = 1 - e_v(x)\cos(2\pi s)$, with $e_v(x) = \beta\cos(2\pi x)$ also seen in the right side of Figure 2.1(a). The combined effect of the oscillatory frequency of the flow, α, and the geometry of the canal, β, is presented in Section 2.3.1. First, the canonical constant-eccentric geometry has been considered, where $\beta \in [0, 0.9]$ and $\alpha \in [1, 15]$, to subsequently study the variable-eccentric one under the same conditions. The results show the existence of an interdependence between both parameters, with changes in the flow topology. Section 2.3.2 shows the influence of the dimensionless wavenumber, k, i.e. the ratio of the canal length to the characteristic wavelength of the elastic wave, in the range $k \in [0, 2]$, considering a constant and uniform value of the compliance factor γ. Finally, the effect of a variable spatial distribution of the elastic properties of the canal is presented in Section 2.3.3, where γ is varied from a constant value to a function which depends on the azimuthal component, s.

2.3.1 Effect of α and β

The combined effect of the geometry and the flow frequency on the CSF motion is evaluated first for the constant eccentricity geometry, $\bar{h}(s) = 1 - \beta\cos(2\pi s)$. To that aim, a case of $\beta = 0.5$ and $\alpha = 3$, with $k = 10^{-3}$, has been selected as the reference one. Velocity profiles from this canonical case are shown in Figure 2.2. As indicated in Sánchez et al. [29], the Eulerian velocity field is described as the combination of a purely oscillatory component driven by the intracranial pressure fluctuations at leading order, obtained as an unsteady lubrication problem, and a steady first-order correction that is a factor ε smaller than the oscillatory flow, associated with the convective acceleration and the deformation of the canal.

For the leading order component (left column in Figure 2.2), in this particular case, the maximum CSF velocity takes place around the widest region of the canal, $s = 0.5$, achieving an amplitude of $u_0 = 1.878$ at $x = 0$, $\eta = 0.5$. This oscillating velocity decreases with the azimuthal component, being $u_0 = 0.384$ at $s = 0$, due to the viscous effects acting around the narrowest section. Considering the first order correction, a characteristic steady bulk flow is established, which moves mainly downwards (away from the brain) along the widest region of the canal and towards the cranial vault along the narrowest one, $s = 0$ (see second column of Figure 2.2). However, there is a thin layer around $0 \lesssim \eta \lesssim 0.1$ and $0.9 \lesssim \eta \lesssim 1$ at $s = 0.5$ where CSF flow reverses, being $u_{SS} = -0.038$ at $\eta = 0.04, 0.96$. Outside this layer, CSF velocity increases rapidly, becoming $u_{SS} = 0.96$ at $\eta = 0.5$ (note that negative velocities indicate that the flow moves towards the brain). The width of this layer increases as we move towards the narrowest region: for example, the reverse flow layer expands from $\eta = 0$ to $\eta \simeq 0.4$ in the symmetry plane, $s = 0.25$, where its amplitude increases to $u_{SS} = -0.162$ at $\eta = 0.14$. In the narrowest region, $s = 0$, the velocity profile has turned completely towards the cranial direction, with a maximum value $u_{SS} = -0.919$ at $\eta = 0.5$. In addition to this steady-streaming velocity, a second steady motion denoted Stokes drift, induced by a purely kinematic effect associated with the spatial nonuniformity of the pulsatile flow, is also established (see column

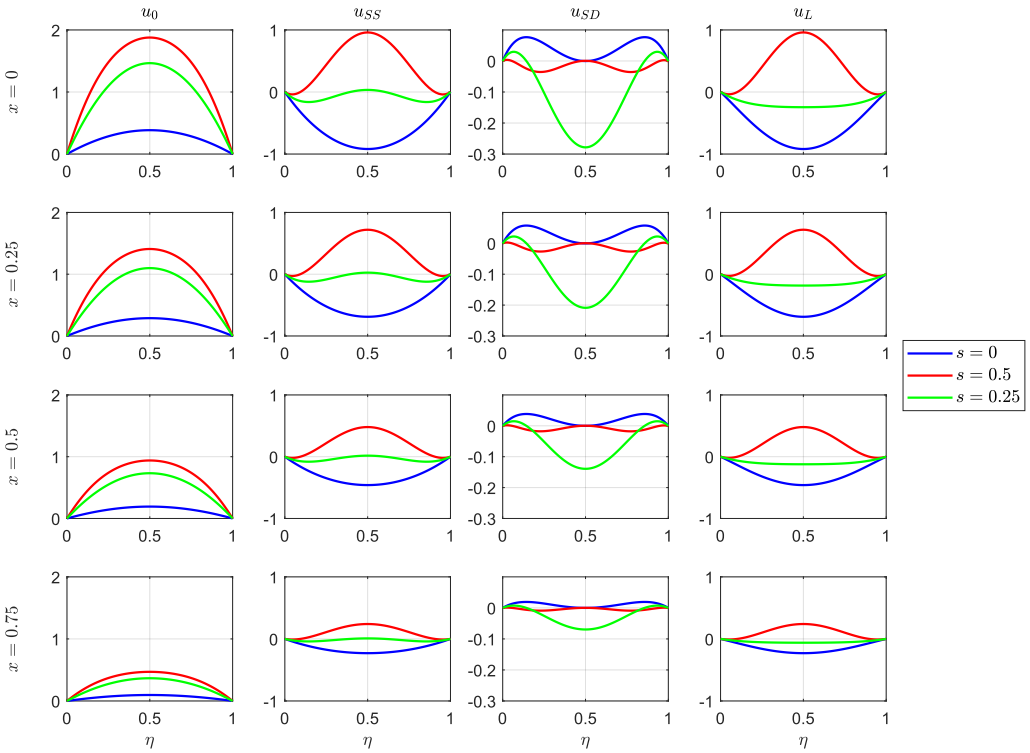

Figure 2.2: Profiles of the streamwise velocity components of the CSF motion along the spinal canal in the canonical case, $\bar{h}(s) = 1 - \beta\cos(2\pi s)$, at $s = 0$, 0.25 and 0.5 respectively ($\beta = 0.5$, $\alpha = 3$, $k = 10^{-3}$).

3 in Figure 2.2). This second steady component is small compared to the steady-streaming one at $s = 0$ and $s = 0.5$, but it becomes relevant around the mid-width region of the canal, $s = 0.25$, where the Stokes drift is of the order of the steady-streaming. Finally, the mean Lagrangian velocity of a fluid particle is the sum of both steady components (see the most right column in Figure 2.2). As indicated above, the mean Lagrangian velocity profiles are similar to the steady-streaming ones at $s = 0$ and $s = 0.5$, being the maximum values $u_L = -0.919$ and $u_L = 0.96$ respectively, which differ substantially from that at $s = 0.25$, where $u_L = -0.2$.

As described by Stuart [90] and Grotberg [91], the time-averaged velocity field is characterized by the steady-streaming induced by the Reynolds stresses acting in the oscillatory boundary layers developing near the walls of the canal. These stresses generate a thin viscous layer of thickness $\delta_v \sim \sqrt{\nu/\omega}$, which can be related with the width of the canal through the Womersley number, $\alpha = h_c^*/\delta_v$. Thus, the dependence of the CSF flow with α is presented herein. In particular, Figure 2.3 shows the axial velocity components of the oscillatory and the bulk flows at different azimuthal locations at $x = 0$, corresponding to the narrowest, mid-width and widest sections of the canal, for $\beta = 0.5$ and different values of α. Substantial differences are observed with α. While the oscillating flow exhibits parabolic profiles at the lowest value of α, it flattens as α increases, especially at $s = 0.25$ and $s = 0.5$. In fact, the maximum velocity decays from $u_0 = 1.878$ for $\alpha = 3$ to $u_0 = 1.142$ for $\alpha = 9$, both peaks located at $s = 0.5$. Such a decrease in the maximum velocity is due to the narrowing of the viscous Stokes layer with α. As α increases, δ_v decreases and the velocity profile becomes flatter away from the walls. These differences are generated by the geometry of the domain. The thickness of the canal is very small and comparable to the Stokes layer in the narrowest section, developing parabolic profiles.

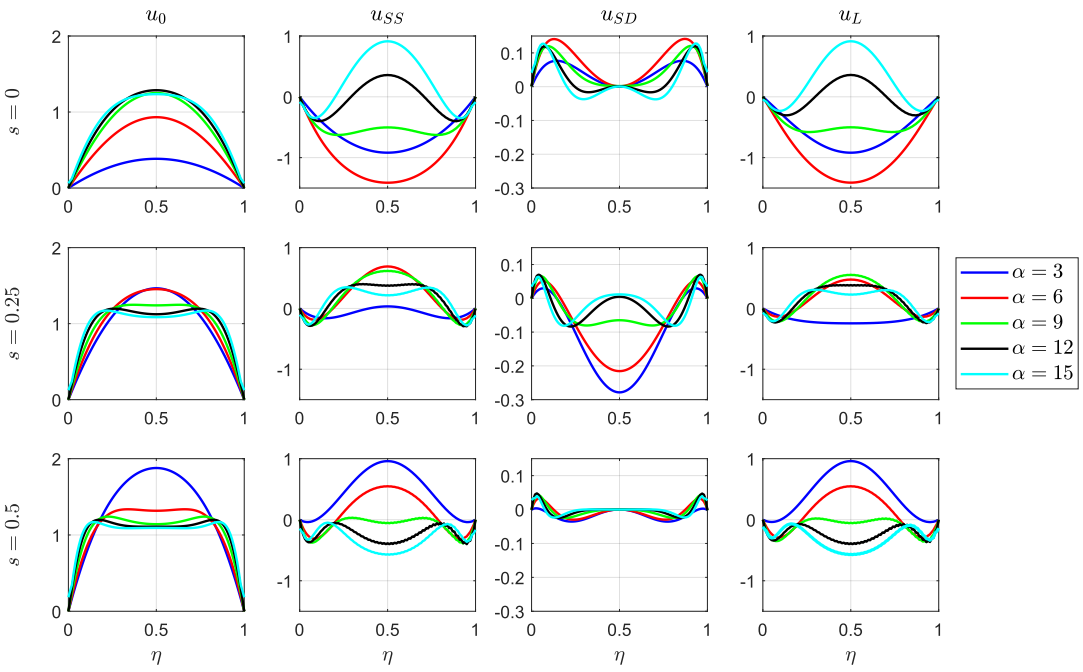

Figure 2.3: Comparison of the CSF velocity profiles at $x = 0$, for a canal geometry given by $\bar{h}(s) = 1 - \beta\cos(2\pi s)$ with $\beta = 0.5$, $k = 10^{-3}$, and different values of α, at azimuthal positions $s = 0$, 0.25 and 0.5 respectively.

However, in the widest section the gap is larger than the Stokes layer and the velocity profiles evolve differently. This phenomenon can be explained by an inspection of the dimensionless x-momentum equation [29],

$$\frac{\partial u}{\partial t} + \varepsilon F_x = -\frac{\partial p'}{\partial x} + \frac{1}{h^2\alpha^2}\frac{\partial^2 u}{\partial \eta^2}. \tag{2.5}$$

where

$$\begin{aligned} F_x = \frac{1}{\ell}\frac{\partial}{\partial x}(\ell u^2) \quad &+ \quad \frac{1}{h}\frac{\partial}{\partial \eta}(uv) + \frac{1}{\ell}\frac{\partial}{\partial s}(uw) \\ &- \quad \frac{\partial h'}{\partial t}\frac{\eta}{h}\frac{\partial u}{\partial \eta} - \frac{\partial h}{\partial x}\frac{\eta}{h}\frac{\partial}{\partial \eta}(u^2) - \frac{1}{\ell}\frac{\partial h}{\partial s}\frac{\eta}{h}\frac{\partial}{\partial \eta}(uw) \end{aligned} \tag{2.6}$$

represent the convective terms. If the leading order $\mathcal{O}(1)$ terms are collected, an unsteady lubrication problem appears. Neglecting the high order terms and substituting the unknowns to the combined expression of a spatial function and a temporal function $\phi_0 = Re\left(\Phi\left(x,\eta,s\right)\Psi\left(t\right)\right)$, Equation (2.5) can be reduced to the following ordinary differential equation,

$$\frac{i}{\bar{h}^2\alpha^2}\frac{\partial^2 U}{\partial \eta^2} + U = \frac{dP'}{dx}, \tag{2.7}$$

where $U(x,\eta,s)$ is the complex function of the axial velocity component, $\bar{h}(x,s)$ is the unperturbed width of the canal and $P'(x)$ is the value of the pressure. The solution

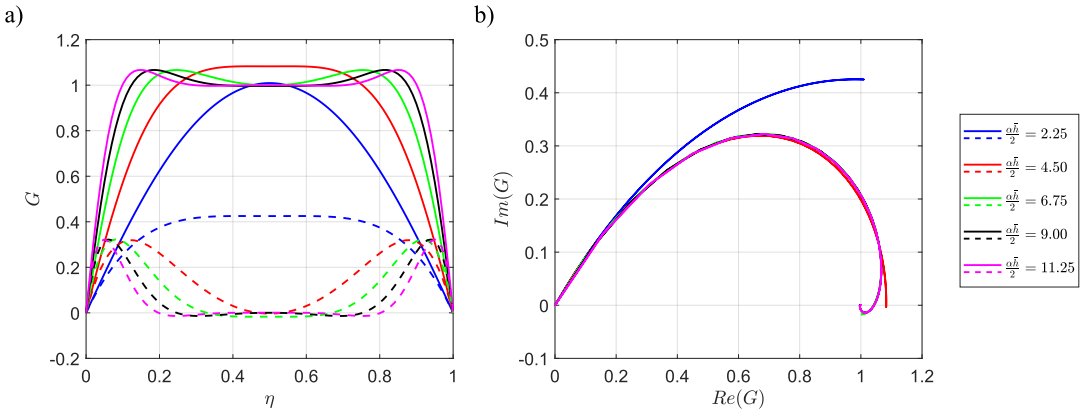

Figure 2.4: a) Evolution of the $Re(G)$ (solid lines) and $Im(G)$ (dashed lines) with η for different values of $\alpha\bar{h}/2$ and, b) Complex function G, displayed as $Im(G)$ versus $Re(G)$, for different values of $\alpha\bar{h}/2$.

for the velocity can be obtained as

$$U(x,\eta,s) = \frac{dP'(x)}{dx} G(x,\eta,s), \quad \text{with} \quad G(x,\eta,s) = 1 - \frac{\cosh\left[\frac{\alpha\bar{h}}{2}\frac{1+i}{\sqrt{2}}(2\eta-1)\right]}{\cosh\left[\frac{\alpha\bar{h}}{2}\frac{1+i}{\sqrt{2}}\right]}, \tag{2.8}$$

being G the solution of the homogeneous ODE [29]. Since P' is a function which depends only on the axial position and $\bar{h}(s) = 1 - \beta\cos(2\pi s)$ for the canonical geometry, G depends on η, the azimuthal position s and α. The evaluation of G for different values of $\alpha\bar{h}/2$ is shown in Figure 2.4. Note that $G = 0$ at $\eta = 0$ and $\eta = 1$, and $Re(G)$ increases as η approaches to $\eta = 0.5$. For low values of $\alpha\bar{h}/2$, both the real and the imaginary parts of G exhibit a parabolic profile (see Figure 2.4a), and $Im(G)$ increases linearly with $Re(G)$ (Figure 2.4b). However, as $\alpha\bar{h}/2$ increases, it can be observed that $Re(G)$ and $Im(G)$ reach a maximum at a value of η that decreases with $\alpha\bar{h}/2$. On the other hand, in the core region, both the real and the imaginary parts of G flatten, reaching values of $Re(G) = 1$ and $Im(G) = 0$ respectively. The thin layer where G increases until it reaches a maximum value corresponds to the thin viscous Stokes layer, whose thickness decreases as $\alpha\bar{h}/2$ increases.

Continuing with the effect of α in the CSF flow, the first order terms $\mathcal{O}(\varepsilon)$ are displayed in the second column of Figure 2.3. Focusing first on the the widest region of the canal, $s = 0.5$, for low values of α, a mean steady velocity is established towards the end of the canal. However, it can be observed that there is a narrow region near the walls where the fluid moves towards the cranial vault. If α increases, this layer becomes wider and the maximum value of u_{SS} decreases (for $\alpha = 6$, $u_{SS,max} = 0.548$ while $u_{SS,max} = 1$ for $\alpha = 3$) until α reaches a certain value, for which the velocity profile is completely caudocranial. Note that, for $\alpha > 9$, the axial velocity in the middle of the canal has turned to negative values ($u_{SS} = -0.05$ for $\alpha = 9$). If the narrowest section is now evaluated, the flow moves towards the brain for $\alpha \leq 9$ with a velocity that decreases with α and starts moving downwards for larger values of α. As consequence, changes of the flow in the mid-width region, $s = 0.25$ are also remarkable. Around $s = 0.25$ the flow mainly moves towards the end of the canal for $\alpha > 3$, although it goes up towards the cranial vault near the walls. However, for $\alpha < 3$ it moves upwards as in the narrowest section, $s = 0$. In the case of the Stokes drift component, its contribution to the total steady motion is very small in

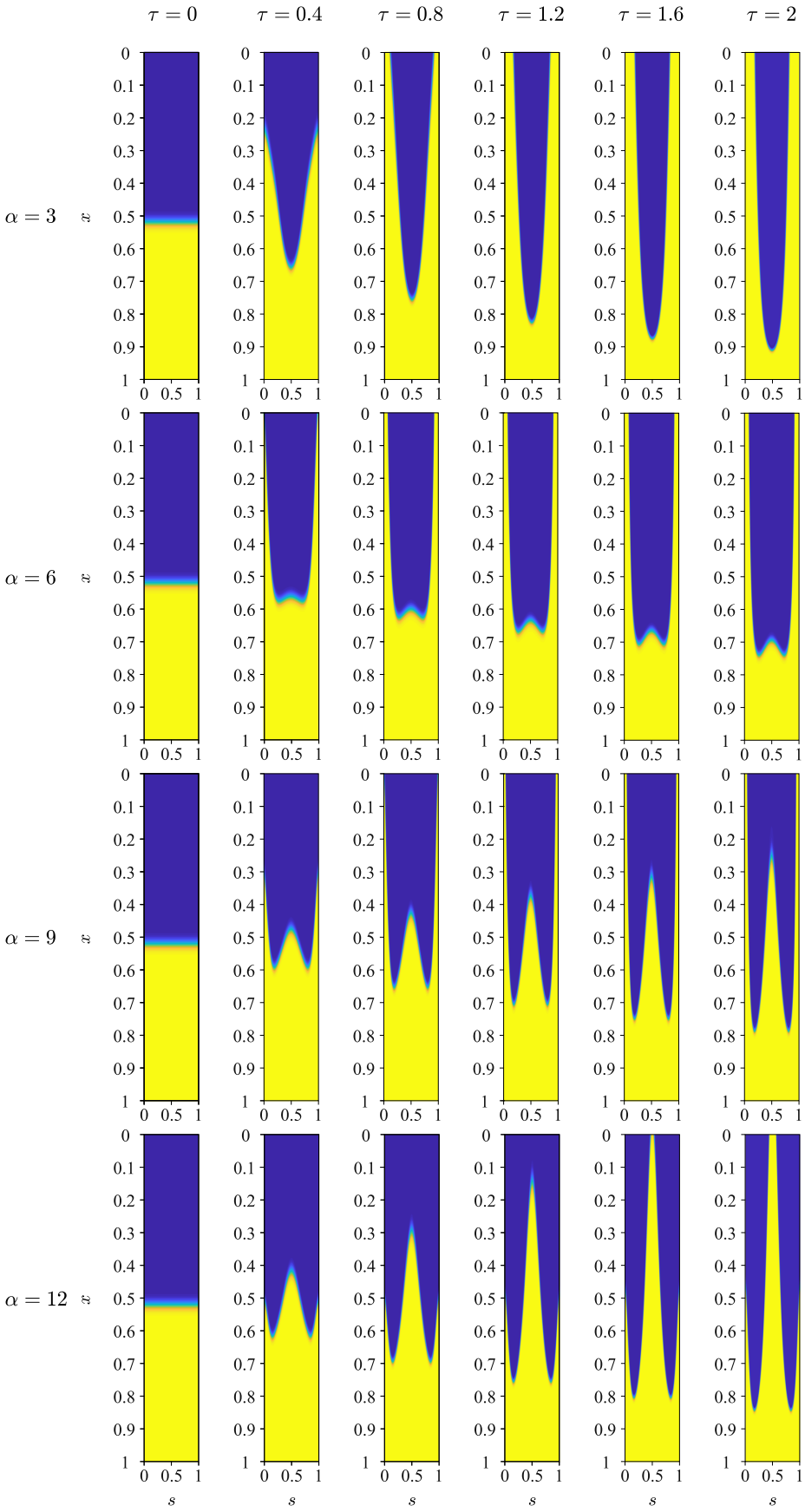

Figure 2.5: Evolution of the solute dispersion along the spinal canal using the canonical geometry $\bar{h}(s) = 1 - \beta\cos(2\pi s)$, with $\beta = 0.5$ and $k = 10^{-3}$, for different values of α.

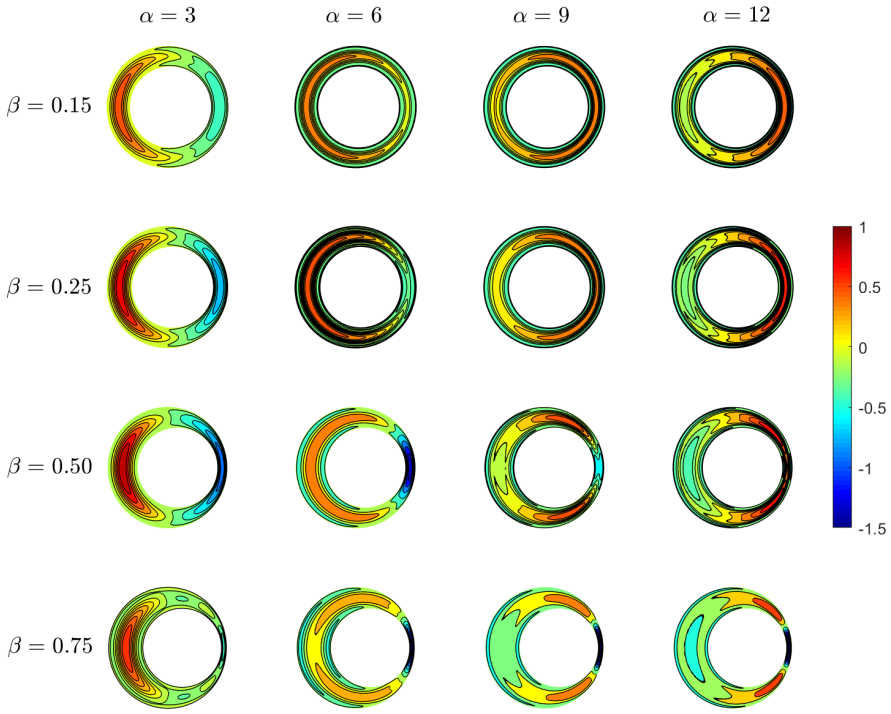

Figure 2.6: Contours of the axial Lagrangian velocity, u_L, at $x = 0$ for different values of the Womersley number, α, and the eccentricity of the canal, β, with $k = 10^{-3}$.

the widest and the narrowest sections, $s = 0.5$ and $s = 0$ respectively, being more relevant around the mid-width section ($s = 0.25$). In this region, u_{SD} is mainly negative (caudocranial, towards the cranial vault) with a value at $\eta = 0$ whose magnitude increases as α decreases. As discussed above, in Figure 2.2, the Lagrangian velocity component is the sum of both the steady-streaming and the Stokes drift components, $u_L = u_{SS} + u_{SD}$, being the steady streaming one the main contribution to the bulk CSF flow.

The CSF steady velocity is crucial to describe the transport of a solute along the SSAS. As inferred from the transport Equation (2.4), the Lagrangian velocity field is one of the two mechanisms driving the dispersion of solute. The second one is the molecular diffusion which depends on the Schmidt number, S, and whose characteristic values are quite large for most of the common administered drugs. Therefore, diffusion effects may become negligible compared to convective transport ones. In order to evaluate this mechanism, Figure 2.5 shows the dispersion of a solute in the spinal canal for different values of α in the $x - s$ plane. In this case, the bottom half of the canal is initially filled from $x = 0.5$ to $x = 1$ with a solute of concentration $C(\tau = 0) = 1$ and Schmidt number $S = 2000$, with a smooth transition at $x = 0.5$, between the maximal and minimal values, to avoid highly diffusive effects during the early stages of the dispersion process. With these initial considerations, the evolution of the solute for $\alpha = 3$ is shown in the first row of Figure 2.5. Due the Lagrangian velocity field described above, it can be observed that the solute rises towards the entrance of the canal along the narrowest section ($s = 0, 1$) and goes down, although slower, along the widest one ($s = 0.5$). For larger values of α, the flow keeps decreasing

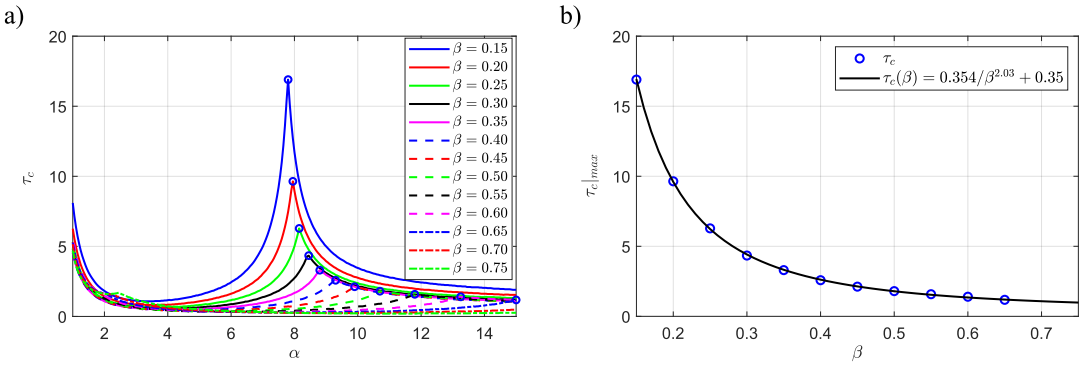

Figure 2.7: a) Dependence with α of the time taken by the solute to reach the cranial vault, τ_c, for different values of β. b) Evolution of $\tau_c|_{max}$, with the canal eccentricity, β.

around $s = 0.5$ but it also does so in the region $0.25 \leq s \leq 0.75$ with velocities slightly larger around $s = 0.25, 0.75$, giving rise to the formation of a small amplitude local maximum of solute concentration at $s = 0.5$ (see second row in Figure 2.5). This indicates that the solute starts to slowly rise around the widest section at $\alpha = 6$. This change generates a second flow topology with an upward motion along the narrowest ($s = 0, 1$) and the widest ($s = 0.5$) regions and a downward motion along the mid-width ($s = 0.25$) region of the canal (see the third row in Figure 2.5). This topology reaches a maximum around a critical value of α, denoted $\alpha_c \simeq 9$, and for $\alpha > \alpha_c$, the solute reaches the cranial vault through the widest section (fourth row in Figure 2.5). Similar flow behaviour is observed for different values of β although the transitions in the flow topology take place at different values of α.

It has been already shown that there is a dependence of the solute dispersion on the Lagrangian velocity field and, therefore on α. Consequently, the time the solute takes to reach the cranial vault, denoted here as τ_c, should also depend on α as well as on the canal geometry, characterized in this case by β. In fact, it has been observed that τ_c increases when the solute begins to rise through the widest section of the canal. Let us try to clarify this phenomenon. Knowing that $\bar{h}(s) = 1 - \beta\cos(2\pi s)$, Equation (2.5) can be approximated by

$$\frac{\partial u}{\partial t} + \varepsilon F_x = -\frac{\partial p'}{\partial x} + \frac{1}{\left[1 - \beta\cos(2\pi s)\right]^2 \alpha^2}\frac{\partial^2 u}{\partial \eta^2}, \tag{2.9}$$

indicating that there is a dependence of the velocity field with β^2. To simplify the discussion, let us focus on s= 0, the narrowest section of the canal. In this case, the term $(1-\beta)^2$ in Equation (2.9) is lower than 1 and higher eccentricities translate in a reduction in the *effective* Womersley number and the corresponding delay in α_c and in the change of the flow topology. In fact, Figure 2.6 shows that the flow moves towards the cranial vault along $s = 0$ for all values of β when $\alpha = 3$. However, the flow changes and begins to move downwards at values of α that increase with β. Moreover, as it can be observed, low values of β generate slow velocities, for example, for $\beta = 0.15$ and $\alpha = 3$, the largest velocities take place at $s = 0$ and $s = 0.5$, being the corresponding values $u_L = -0.444$ and $u_L = 0.60$ respectively. As β increases, the magnitude of the velocity also increases (i.e., for $\beta = 0.50$ and $\alpha = 3$, $u_L = -0.92$ and $u_L = 0.96$, at $s = 0$ and 0.5), reducing the time the solute takes to reach the cranial vault, τ_c. However, as already mentioned, a delay in the change of the flow topology is apparent, occurring at larger values of α.

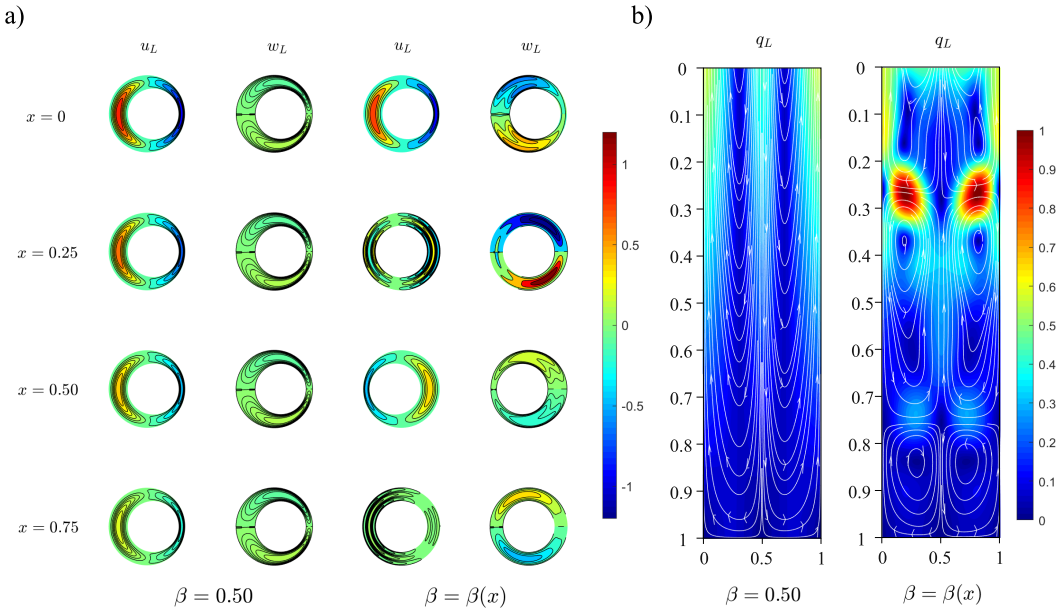

Figure 2.8: Comparison of the velocity fields obtained using the straight and the curved geometries. a) Contours of the axial, u_L, and azimuthal, w_L, Lagrangian velocities at different downstream positions. b) Lagrangian streamlines of the width averaged values of the axial and azimuthal velocities $\int_0^1 u_L d\eta$ and $\int_0^1 w_L d\eta$ in the $s-x$ plane with contours of $q_L = \left[(\int_0^1 u_L d\eta)^2 + (\int_0^1 w_L d\eta)^2\right]^{1/2}$, the width-averaged Lagrangian velocity magnitude. Here $\alpha = 3$ and $k = 10^{-3}$.

In addition to the velocity contours displayed in Figure 2.6, τ_c can be used to evaluate the combined effect of α and β. To that aim, Figure 2.7(a) shows the evolution of τ_c with α for different values of β. Initially, for low values of α, the time taken by the solute to reach the cranial vault decreases as α increases until it reaches a minimum value between $4 \lesssim \alpha \lesssim 7$ that depends on β. Afterwards, τ_c begins to increase, corresponding to a situation when the flow rises slowly towards the brain through the widest and narrowest sections, until it reaches a maximum value, $\tau_c = \tau_c|_{max}$, at $\alpha = \alpha_c$, when the flow moves in both sections with similar velocities. Larger values of α make the upward flow at $s = 0$ to slow down, increasing the rising velocity along the widest section ($s = 0.5$). Consequently, the solute transport towards the brain becomes faster again and the value of τ_c decreases rapidly with α. The same behaviour occurs for all values of β, although $\tau_c(\beta)|_{max}$ decreases, and takes place at higher values of α, as β increases. In fact, the maximum value of τ_c decays with β as

$$\tau_c(\beta)|_{max} = \frac{0.354}{\beta^2} + 0.35, \tag{2.10}$$

as shown in Figure 2.7(b). This expression is in good agreement with the modified expression of the momentum equation, where the velocity components are related to β^{-2}.

So far the analysis has been developed for a canonical geometry which consists of an eccentric annulus with a constant cross section, given by $\bar{h}(s) = 1 - \beta\cos(2\pi s)$. However, the geometry of the spinal canal is much more complex. Thus, to go a little deeper into the knowledge of the behaviour of the CSF flow, we are going to take a step forward and analyze the case of a geometry with variable eccentricity.

This new geometry consists of an eccentric annulus whose eccentricity varies with x, given by $\bar{h}(x,s) = 1 - \beta\cos(2\pi s)\cos(2\pi x)$, as shown in Figure 2.1(a). Figure 2.8 displays the comparison of the velocity fields obtained using the straight and the curved geometries for $\alpha = 3$, $\beta = 0.5$ and $k = 10^{-3}$. In particular, Figure 2.8(a) shows the contours of the axial, u_L, and azimuthal, w_L, Lagrangian velocities at different downstream positions, while Figure 2.8(b) displays Lagrangian streamlines of the width-averaged values of the axial and azimuthal velocities $\int_0^1 u_L(\eta)d\eta$ and $\int_0^1 w_L(\eta)d\eta$ in the $s-x$ plane with contours of width-averaged Lagrangian velocity magnitude, $q_L = \left[(\int_0^1 u_L(\eta)d\eta)^2 + (\int_0^1 w_L(\eta)d\eta)^2\right]^{1/2}$. As described above, in the straight configuration, at $\alpha = 3$, the CSF flow is caudocranial along the widest section and craniocaudal along the narrowest, with almost negligible azimuthal velocities except near the bottom of the canal. However, when the curved geometry is used the flow topology significantly changes. Three recirculating regions are formed inside the canal, a first one from $x = 0$ to $x \approx 0.25$, the second one from $x \approx 0.25$ to $x \approx 0.75$ and a third one from $x \approx 0.75$ to $x = 1$, exhibiting two stagnation points at $x \approx 0.25$ and 0.75 respectively. In this case, the flow goes down along the widest region ($s = 0.5$) in the upper recirculating zone while it goes up through the narrowest one ($s = 0, 1$). However, the flow field changes in the central region, ascending around $s = 0.5$ and descending through $s = 0, 1$ due to the changes of the geometry where at $x = 0.5$ the narrowest section changes to $s = 0.5$ and the widest one to $s = 0, 1$. Large azimuthal velocities are generated near the upper stagnation point, where the flow that goes down around $s = 0.5$ turns towards $s = 0, 1$ before beginning to rise (see the velocity contours of w_L at $x = 0.25$ in the fourth column of Figure 2.8a and the red spots around $x \approx 0.25$ in the second column of Figure 2.8b). If the contours of u_L are compared, it is seen that the axial flow is slightly faster in the canonical case at $x = 0$.

Despite the formation of three different recirculating cells in the variable-eccentric geometry, it is important to describe how the solute is transported towards the cranial vault in this case. Evolution of the solute dispersion along the spinal canal using the curved, unperturbed geometry, given by $\bar{h}(x,s) = 1 - \beta\cos(2\pi x)\cos(2\pi s)$, with $\beta = 0.5$ and different values of α is shown in Figure 2.9. For $\alpha = 3$, the CSF flow transports the solute along $s = 0.5$ (narrowest region of the canal at $x \approx 0.5$) until $x \simeq 0.25$, where it turns azimuthally towards $s = 0, 1$ before starting to recirculate towards the bottom of the canal at $\tau \approx 0.8$. However, a small amount of solute crosses to the upper cell and reaches the cranial vault through a very thin layer that rises at $s = 0, 1$. Since the velocity field established in the curved geometry configuration is considerably different from that of the straight case, the time the solute takes to reach the cranial vault increases substantially (while Figure 2.5 shows that $\tau_c < 0.8$ in the straight geometry, it increases to $\tau_c = 1.2$ in the variable eccentric case). Similar behaviour is observed if α increases to $\alpha = 6$. However, the filament of solute that rises around $s = 0.5$ is narrower in this case than in the case of $\alpha = 3$, indicating that the amount of solute transported is considerably reduced. Furthermore, when the solute reaches $x \approx 0.25$, it also turns towards $s = 0, 1$ and begins to descend along a very thin layer with nearly no solute crossing to $x < 0.25$. If α is further increased to $\alpha = 9$, it can be observed the formation of a very thin filament of solute that rises thorough $s = 0.5$ all the way to the cranial vault without turning down. At the same time, clean CSF slowly descents towards the bottom of the canal around $s = 0.25, 0.75$. Finally, striking differences are observed at $\alpha = 12$, where most of the solute rises very slowly around $s = 0, 1$ with the formation of a very thin filament at $s = 0.5$, increasing substantially the time the solute takes to reach the entrance of

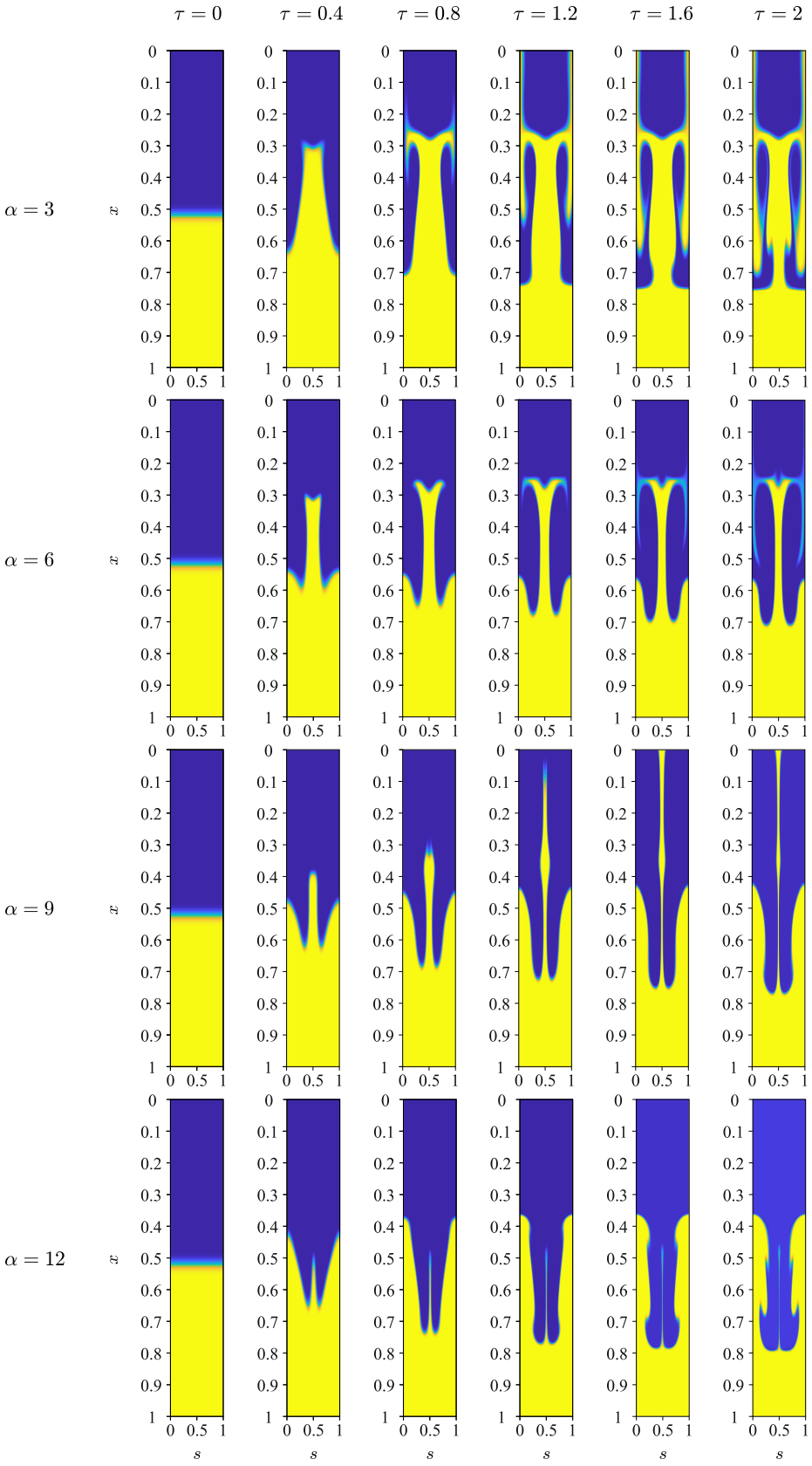

Figure 2.9: Evolution of the solute dispersion along the spinal canal using the curved geometry $\bar{h}(s) = 1 - \beta\cos(2\pi x)\cos(2\pi s)$, with $\beta = 0.5$ and $k = 10^{-3}$, for different values of α.

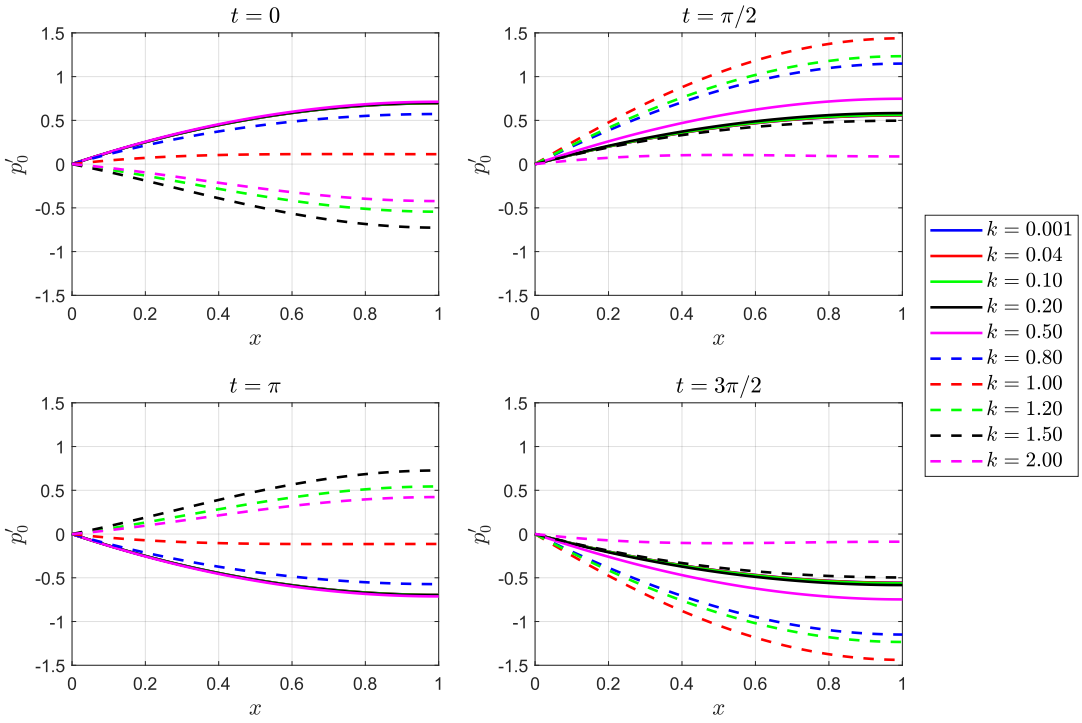

Figure 2.10: Downstream evolution of $p_0'(x)$ for different values of k at several instants of time using the straight geometry ($\beta = 0.5$, $\alpha = 3$).

the canal.

2.3.2 Effect of the wavelength of the elastic wave, k

The following relevant aspect to evaluate the CSF motion and the corresponding solute transport along the spinal canal is the effect of the elastic wave of the canal, which depends on its compliance, γ^*. As described in Sánchez et al. [29] and Lawrence et al. [39], the intracranial pressure fluctuations (induced by the cardiac flow) displace a small amount of CSF accommodated in the spinal canal in and out the spinal canal. The effect of the pressure wave propagating along the canal will be described in terms of its dimensionless wavenumber, k, given by Equation (2.3), with $[(h_c/\gamma_c^*)/\rho]^{1/2}$ representing the relevant elastic wave speed. Following the analysis to compute the leading order velocity field, presented in Sánchez et al. [29] and Lawrence et al. [39], the deformation of the outer surface, H', can be determined through the constitutive equation,

$$H' = \gamma \left(1 + k^2 P'\right), \tag{2.11}$$

where it is remembered that $\gamma(x, s)$ is the dimensionless compliance of the canal, k is the dimensionless wave number and $P'(x)$ is the relative spatial pressure variation. Substituting Equation (2.11) in the continuity balance and integrating in the cross-section area yields [39],

$$\frac{1}{\ell}\frac{d}{dx}\left(\ell\, Q \frac{dP'}{dx}\right) + \left(\int_0^1 \gamma\, ds\right)\left(k^2 P' + 1\right) = 0, \tag{2.12}$$

with $P' = 0$ at $x = 0$ and $dP'/dx = 0$ at $x = 1$, and $Q(x)$ being the volume flux, which depends on α and $\bar{h}$. The solution of Equation (2.12) exhibits an interdependence between $Q(x)$ and k. In the simplified case, where the flow is driven by the

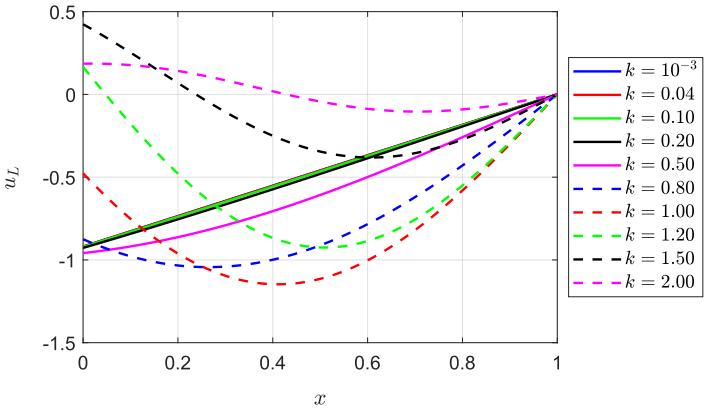

Figure 2.11: Downstream evolution of the axial component of the Lagrangian velocity, $u_L(x, 0.5, 0)$, at $\eta = 0.5$ and $s = 0$, for different values of k in the straight geometry ($\beta = 0.5$, $\alpha = 3$).

periodic pressure fluctuations in the cranial cavity, $P'(x)$ is given by,

$$P' = \frac{1}{k^2}\left(\frac{\cos\left[k\left(1-x\right)/\sqrt{Q}\right]}{\cos\left(k/\sqrt{Q}\right)} - 1\right). \tag{2.13}$$

Results of the pressure variations, given by $p_0'(x,t) = Re\left[e^{it}P'(x)\right]$ are shown in Figure 2.10 at different instants of time for several values of k. As expected, $p_0'(x,t)$ varies with x, with a magnitude that increases from $p_0' = 0$ at $x = 0$ to a finite value at $x = 1$, where $dp_0'/dx = 0$. In particular, $p_0'(x)$ barely depends on k for $k < 0.5$, indicated with solid lines in Figure 2.10. In these cases the wavelength of the elastic wave is larger than the length of the canal and the wall deforms everywhere at the same time, being all the points in phase. Differences are observed as k increases, for which the evolution of $p_0'(x)$ depends on time due to the oscillating nature of the flow. For example, at $t = 0$ ($t = \pi$), $p_0'(x)$ decreases (increases) as k increases, being $dp_0'/dx > 0$ ($dp_0'/dx < 0$) for $k < 1$ and $dp_0'/dx < 0$ ($dp_0'/dx > 0$) for $k > 1$, and the situation reverses at $t = \pi$ ($t = 0$). At $t = \pi/2$ ($t = 3\pi/2$) the dependence of p_0' with k varies due to the complex interaction of $P'(x)$ with e^{it} in the determination of $p_0'(x,t)$. In this case $p_0'(x) \approx 0$ for $k = 2$ while $p_0'(x) \approx 0$ for $k = 1$ at $t = 0$ ($t = \pi$).

Since k is one of the parameters that govern the development of the leading order velocity profiles through $p_0'(x,t)$, it also affects the first order components. To explore such effects, Figure 2.11 shows the variation of the axial component of the Lagrangian velocity at $\eta = 0.5$ and $s = 0$, along the length of the canal, $u_L(x, 0.5, 0)$. As it happened with $p_0'(x)$, the Lagrangian velocity barely depends on k for $k < 0.5$. In this case, $u_L(x, 0.5, 0)$ is negative along the spinal canal, $0 \leq x \leq 1$, indicating that the velocity goes towards the cranial vault with a magnitude that decreases linearly as x increases. However, differences begin to be observed for $k \geq 0.5$. In these cases, the axial Lagrangian velocity no longer decreases with x, but reaches a maximum at a downstream position that increases with k, although its magnitude decreases with k for $k > 1$. For $k > 1$, for which the wavelength of the elastic wave is smaller than the length of the canal, it can be observed that the flow goes down near the entrance of the canal while it reverses and begins to rise up further downstream. This change in the velocity indicates the formation of recirculating cells with velocity magnitudes that decrease as k increases.

Beyond the evaluation of the axial velocity component at a given radial and azimuthal position, it is interesting to investigate the effect of k in the entire canal.

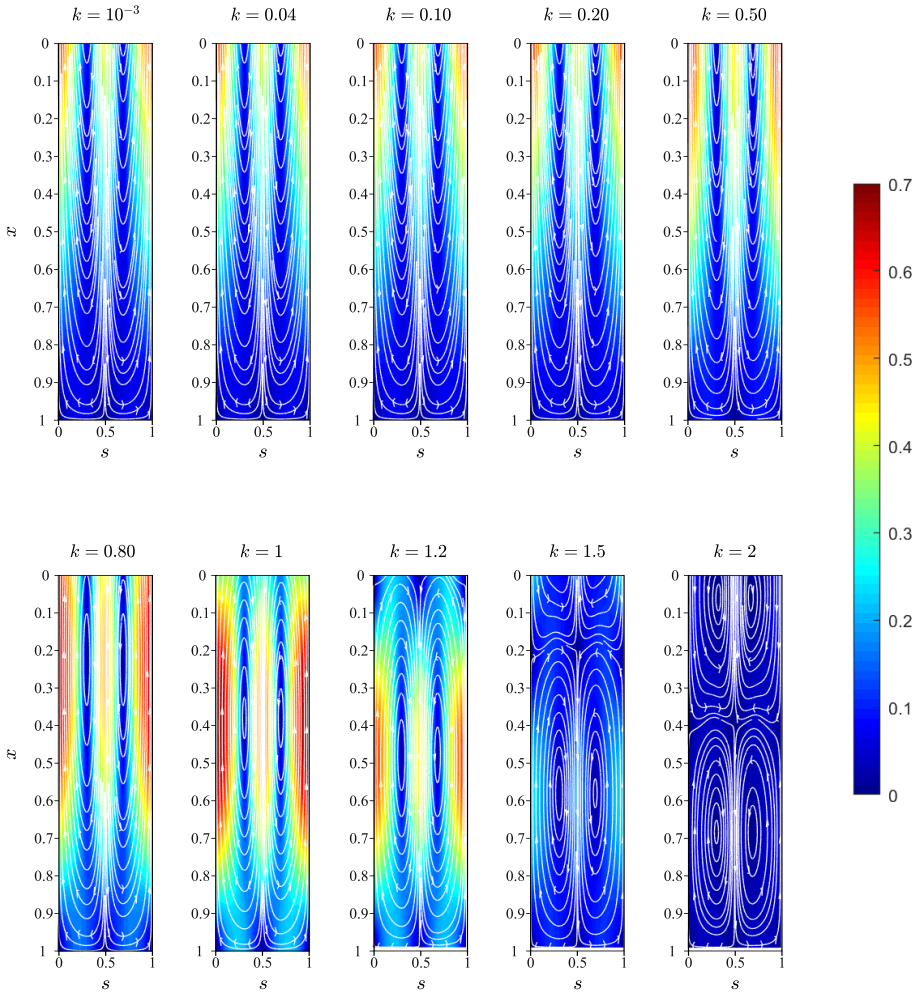

Figure 2.12: Comparison of the Lagrangian streamlines of the width averaged values of the axial and azimuthal velocities $\int_0^1 u_L d\eta$ and $\int_0^1 w_L d\eta$ in the $s-x$ plane with contours of $q_L = \left[(\int_0^1 u_L d\eta)^2 + (\int_0^1 w_L d\eta)^2\right]^{1/2}$ for different values of k. Here $\alpha = 3$ and $\bar{h}(s) = 1 - \beta\cos(2\pi s)$ with $\beta = 0.5$.

Thus, Figure 2.12 displays Lagrangian streamlines of the width averaged values of the axial and azimuthal velocities $\int_0^1 u_L(\eta)d\eta$ and $\int_0^1 w_L(\eta)d\eta$ in the $s-x$ plane with contours of $q_L = \left[(\int_0^1 u_L(\eta)d\eta)^2 + (\int_0^1 w_L(\eta)d\eta)^2\right]^{1/2}$, the width-averaged Lagrangian velocity magnitude, for different values of k. For low values of k, the flow goes down towards the bottom of the canal around $s = 0.5$, the widest section, and rises up around $s = 0, 1$, the narrowest one. In these cases, the maximum velocity is found near the entrance of the canal and the streamlines do not close at $x = 0$. However, as k increases, it can be observed that the location of maximum velocity penetrates inside the spinal canal and the streamlines begin to close. For $k > 1.2$ the flow field exhibits the formation of a couple of recirculating regions, indicating that only fluid in the upper part of the canal is refreshed (penetrating around $s = 0, 1$ and exiting around $s = 0.5$). The upper recirculating region increases while the lower one decreases as k increases. Consequently, the flow field changes dramatically with k for

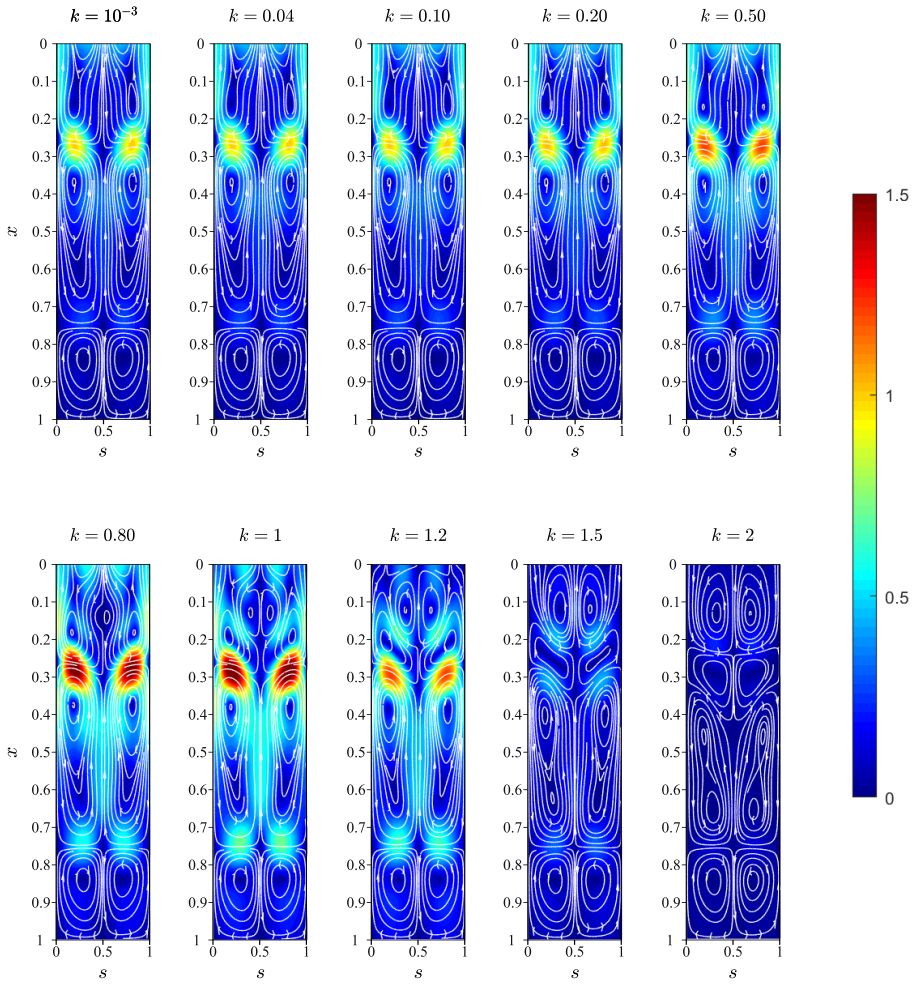

Figure 2.13: Comparison of the Lagrangian streamlines of the width averaged values of the axial and azimuthal velocities $\int_0^1 u_L d\eta$ and $\int_0^1 w_L d\eta$ in the $s - x$ plane with contours of $q_L = \left[(\int_0^1 u_L d\eta)^2 + (\int_0^1 w_L d\eta)^2\right]^{1/2}$ for different values of k. Here $\alpha = 3$ and $\bar{h}(x, s) = 1 - \beta \cos(2\pi x) \cos(2\pi s)$ with $\beta = 0.5$.

$k > 1$, affecting the solute dispersion along the canal.

Although the dependence of the velocity field and flow topology on k has been evaluated in the canonical case, the actual geometry of the SSAS is more complex. Thus, it is necessary to extend the present study to a more detailed geometry, where the eccentricity change is considered. Consequently, flow patterns for different values of k are presented in Figure 2.13 using the variable eccentric geometry described above. In general, it can be seen the presence of three different recirculating cells, caused by the changes in the eccentricity along the canal, with the separating streamlines located at $x \approx 0.25$ and 0.75. The flow pattern barely changes for $k < 0.5$, observing only a small increase in the velocity magnitude near the upper stagnation point (around $x = 0.25$, $s = 0.25, 0.75$) with k. For larger values of k, the flow topology changes, with the generation of an additional recirculating cell in the range of $x \in [0.05, 0.2]$. This new cell enlarges with k, reducing the central one. In addition, the magnitude of

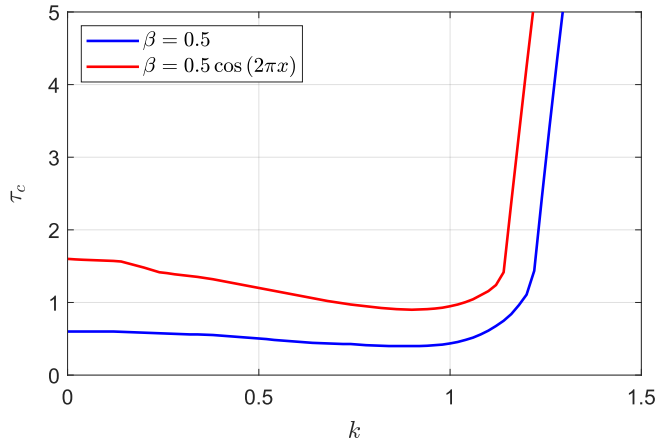

Figure 2.14: Dependence on k of the time the solute, initially located at $x = 0.5$, takes to reach the cranial vault, τ_c, for both the straight and the curved geometries with $\alpha = 3$.

q_L also increases with k and reaches its maximum at $k = 1$, before decreasing again for larger values of k.

The characterization of the CSF motion at different values of k can be extended to the corresponding solute transport. To that end, it is worth exploring the effect of k in the time taken for the solute to reach the cranial vault, $\tau_c(k)$. Figure 2.14 shows the evolution of τ_c with k using both, the straight and the curved geometries with $\alpha = 3$. It is clearly observed that the solute reaches faster the cranial vault in the straight geometry since in this case the flow pattern does not exhibit recirculating cells where the solute gets trapped. It is also seen that in both cases τ_c decreases with k in the range $0 < k < 1$, reaching a minimum value at $k \approx 1$. For $k > 1$, τ_c increases rapidly due to the formation of recirculating cells that hinder the transport of solute to the brain.

2.3.3 Effect of the compliance of the canal, $\gamma(s)$

In this chapter the analysis of the CSF motion has been evaluated assuming simplified configurations. First, a canonical geometry ($\beta = 0.5$) has been used with specific flow conditions ($\alpha = 3$) and wave number ($k = 0.001$). Under these conditions, a parametric analysis has been conducted, modifying the geometry of the canal and flow conditions (Section 2.3.1) on the one hand, and the wave number on the other hand (Section 2.3.2). However, the effect of the elastic properties of the canal has not been evaluated yet. Results from the analysis of the effect of $\gamma(s)$ on the CSF flow will be presented in this section. Thus, to perform the analysis, although the compliance of the canal can vary with x and s, we will assume that γ does not change with x and establish a function given by $\gamma(s) = as^2 + bs + c$, with $2\int_0^{0.5} \gamma(s)\, ds = 1$. Three different cases are studied varying the canal compliance as shown in Figure 2.15. The first case considers the compliance in the canal with $\gamma_0 = 1$. In the second case, $\gamma_A = 3(1-\gamma_i)(16s^2 - 8s + 1) + \gamma_i$, the compliance is maximum at $s = 0, 0.5$ and the outer wall elongates around the narrowest and widest regions and flattens around $s = 0.25, 0.75$, acquiring an oblate shape. Finally, the third case, $\gamma_B = 12(\gamma_i - 1)(2s-1)s + \gamma_i$, is the opposite to the second one with the outer wall elongating at $s = 0.25, 0.75$ and flattening around the narrowest and widest sections, acquiring thus a prolate shape. Here γ_i indicates the minimum value of γ_A at $s = 0.25$ and γ_B

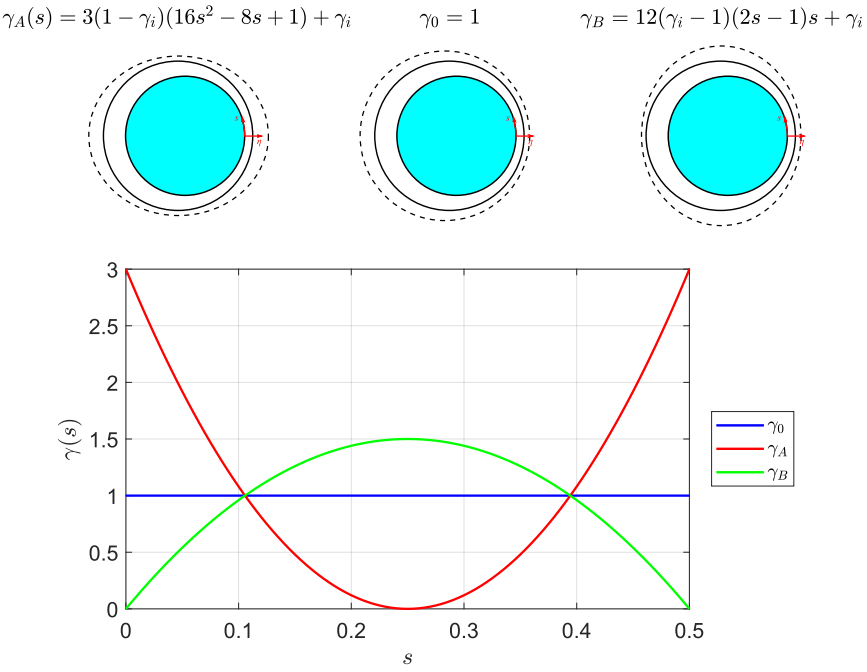

Figure 2.15: Flexible wall motion (upper panel) given by the three different compliance functions of the canal, $\gamma(s)$, shown in the lower plot.

at $s = 0, 0.5$. Notice, that $\gamma_0 = \gamma_A = \gamma_B$ for $\gamma_i = 1$.

Results of the solute dispersion for the different cases of $\gamma(s)$ are presented in Figure 2.16 using the straight geometry, $\bar{h}(x,s) = 1 - \beta\cos(2\pi s)$, with $\beta = 0.5$ and $k = 10^{-3}$. Here, the time taken for the solute, initially at $x = 0.5$, to reach the cranial vault, τ_c, is evaluated, considering the previously described compliance functions $\gamma(s)$, parameterized with γ_i. Results show different behaviours depending of the compliance of the walls, although there are some similarities. In all the cases it can be observed that τ_c decreases with the Womersley number for low values of α until it reaches a minimum in the range $4 \leq \alpha \leq 7$, that depends on γ_i. As α increases, τ_c increases rapidly until it reaches a sharp maximum, $\tau_c|_{max}$, before it decreases again with α. A clear decrease is observed in τ_c in the range $1 \leq \alpha \leq 10$, when an azimuthal variation of the compliance of the canal is given by γ_A (see Figure 2.16a). In fact, in this case where γ is higher (more flexible) around the narrowest and the widest section and smaller (more rigid) at $s = 0.25$, the minimum of τ_c decreases from $\tau_c = 0.36$ for $\gamma_i = 1$ to $\tau_c = 0.16$ for $\gamma_i = 0$, taking place in both situations at $\alpha = 5.3$. This resulting trend indicates that the enhanced deformation of the canal around $s = 0$ and $s = 0.5$ intensifies the flow of the CSF that rises through the narrowest section, decreasing therefore τ_c. However, at larger values of α the flow topology changes and starts to rise up through the widest and narrowest sections and to go down around $s = 0.25$, to eventually go up through the widest section ($s = 0.5$) and go down through the narrowest one ($s = 0$) for larger values of α. These changes in the flow topology cause the sharp increase of τ_c observed around $\alpha \approx 11$. Such increase is more apparent when a varying function of the compliance, given by γ_A, is assumed than when it is assumed to be constant, $\gamma_0 = 1$. For example $\tau_c|_{max}$ increases from $\tau_c|_{max} = 1.8$, at $\alpha_c = 10.7$ for $\gamma_0 = 1$, to $\tau_c|_{max} = 3.58$, at $\alpha_c = 11.2$ for $\gamma_i = 0.6$. If γ_i continues decreasing, the trend reverses: for $\gamma_i < 0.5$, the peak represented by $\tau_c|_{max}$ decreases and takes place at lower values of α (i.e., for $\gamma_i = 0$, $\tau_c|_{max} = 1.54$ and $\alpha_c = 10.7$).

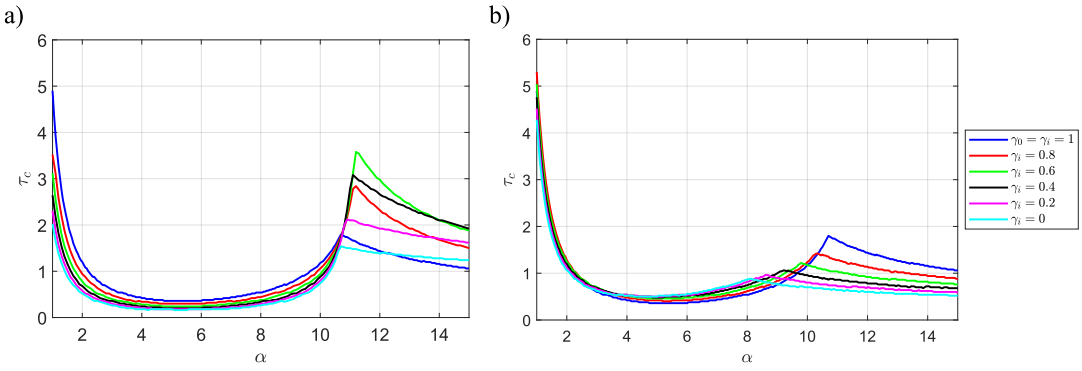

Figure 2.16: Evolution of $\tau_c(\alpha)$ with α for different compliance functions implemented in the straight geometry with $\beta = 0.5$ and $k = 0.001$. a) $\gamma_A(s) = 3(1-\gamma_i)(16s^2 - 8s + 1) + \gamma_i$ and b) $\gamma_B(s) = 12(\gamma_i - 1)(2s - 1)s + \gamma_i$. In both cases, $\gamma_i \in [0, 1]$.

In the opposite case, Figure 2.16(b) evaluates the effect of $\gamma(s)$ when the perturbed shape of the canal is given by $\gamma_B = 12(\gamma_i - 1)(2s - 1)s + \gamma_i$ (the most compliant regions are located at $s = 0.25, 0.75$ as shown by the green line in Figure 2.15). In this case, the changes of τ_c with γ_i are less relevant than in the previous case where $\gamma(s) = \gamma_A(s) = 3(1-\gamma_i)(16s^2 - 8s + 1) + \gamma_i$. In fact, τ_c barely changes with γ_i in the range $1 < \alpha < 3$ and, unlike in the case with γ_A, it decreases as γ_i decreases for larger values of α. It is worth noticing that, using a compliance function given by γ_B, $\tau_c|_{max}$ decreases considerably and takes place at lower values of α as γ_i decreases.

2.4 Conclusions

The present chapter analyses the CSF motion along the SSAS, with special attention focused on the solute injected dispersion around low thoracic and lumbar regions of the spinal canal, the most common injection points in ITDD protocols. To that aim, we have characterized the velocity field and flow topology varying the governing parameters of the problem. This parametric analysis has been developed for the canonical geometry presented in previous theoretical [21], [29], [39] and numerical [47] studies. In these works, the canal has been modelled as an annular, eccentric and slender canal, whose motion depends on the induced intracranial pressure fluctuations. Following this model, the flow topology has been evaluated according to the geometry of the canal and the nature of the oscillatory motion, the pressure wave propagation and the elastic behaviour of the canal. This study, which has been initially performed with a canonical straight geometry, has been extended to a more realistic geometry. The results of this study highlight the interdependence of the geometry and the oscillatory nature of the CSF motion, which shows a close relationship between the changes of the flow topology and the geometry of the canal. Recirculating regions are generated in the straight geometry when the wavelength of the elastic wave is smaller than the length of the canal, i.e $k > 1$. Finally, considering the flexibility of the dura membrane as a s-dependent function, the flow conditions are modified, varying also the flow topology and the time the solute takes to reach the cranial vault. These results constitute a deeper study of the CSF motion along the spinal canal than those in previous works, which allows to go a step further in understanding the phenomena in specific patients and, therefore, in developing more efficient ITDD protocols.

Chapter 3

In vitro characterization of the solute transport along the spinal canal

This chapter presents an experimental study of the CSF solute transport along the SSAS, which corresponds to a continuance of the previous model [29], [39], [47] and the parametric study presented in Chapter 2. In fact, this study focuses on the effects of the governing parameters in the CSF solute dispersion, such as the SSAS geomtery and the oscillatory flow frequency. To that end, an *in vitro* model has been manufactured, consisting of an annular eccentric canal with constant cross-section, delimited by an exterior crystal-clear rigid wall and an inner rubber flexible wall, on which the CSF motion is induced thanks to a programmable peristaltic pump, which allows to control the flow frequency and injected stroke volume. This canal is connected to a rigid, closed cubic reservoir on one side, corresponding to the brain, and is closed on the other side. By the use of phase-averaged tracking of a fluorescent dye, the experiments evaluate the effect of the eccentricity for three different eccentricities under the same flow conditions with two different techniques: tracking the solute edge by one side, and the temporal tracer concentration inside the brain by the other side. Moreover, the effect induced by the flow frequency is also evaluated for the most eccentric geometry. Finally, as is seen in previous studies [21], [22], [32], [47], the solute dispersion in this canonical geometry is compared with that in a close-to-real geometry, which consists of a variable eccentric canal. Results of this work are in good agreement with the corresponding results of Chapter 2, which validates the analytical model of CSF motion and solute transport along the spinal canal.

This chapter is comprised in the paper: "In vitro characterization of solute transport in the spinal canal", by F. Moral-Pulido, J.I. Jiménez-González, C. Gutiérrez-Montes, W. Coenen, A. L. Sánchez & C. Martínez-Bazán, published in Physics of Fluids [26].

3.1 Introduction

The CSF, provided from the blood plasma, is a Newtonian liquid with close-to-water physical properties. This fluid, located at the SAS and the perivascular space, presents well-known mechanical and physiological properties, being the transport of substances one of the most relevant features for the sake of a well-performance of the central nervous system. In fact, as CSF is concerned to be an effective drug transport medium because of surpassing the BBB, modelling the CSF motion yields a paramount interest, as seen in literature. Indeed, previous works[29] characterize the CSF motion as

the cumulative sum of a purely oscillatory component, induced by intracranial pressure fluctuations, with characteristic times of the heart beat ω^{-1}, and a second-order steady bulk circulation with characteristic times of $\varepsilon^{-2}\omega{-}1$, where ε is of order of the relative stroke volume of CSF. This steady component depends on two effects: on the one hand, the non-linear convective effects and, on the other hand, the so-called Stokes Drift (a purely kinematic effect appeared in oscillatory phenomena). In regard to the solute transport, the model uses a reduced transport equation, where the width-averaged Lagrangian velocity field determines the convective transport rate in the long time scale, reducing the computational time by not computing the solute dispersion during the short time scale cycle [39]. This model, which has been developed for simplified geometries of the spinal canal, has been evaluated in previous works [22], [47] and intensively in the previous chapter, wherein the effects of the governing parameters have been studied deeply, such as the related effects to the geometry, the oscillatory frequency, the pressure wave propagation and the compliance of the canal.

Beyond efforts to analytically and numerically model CSF flow and solute transport, a few attempts have been made to address the problem experimentally [48]–[52]. In these works, different types of *in vitro* models, from idealized channel with a simplified flow waveform [48] to ultra realistic patient-specific geometries with real CSF flow rates [49], [50], have been considered, leading to promising results. However, these studies deal with rigid canals that are open at both ends, and do not directly address the role of the compliant dura membrane and the associated fluid-structure interaction problem, an important aspect of the CSF dynamics in the SSAS.

Motivated by the clinical relevance of solute transport in the spinal canal and the lack of a thorough experimental characterization of the problem, we present here an *in vitro* experimental study of the solute transport along a compliant spinal canal. In the following, Section 3.2 provides a description of the experimental facility, accordingly to the aforementioned model, and the experimental techniques, employed in this study. Then the results of the considered experiments are presented in Section 3.3, dividing into the canonical geometry (Section 3.3.1) and a first-approximation model, based on a variable eccentric canal (Section 3.3.2). Finally, conclusions of this chapter are drawn in Section 3.4.

3.2 Experimental details and techniques

The experimental facility used in this study, to be described below, enables the quantification of effects of spinal-cord eccentricity and flow frequency on solute transport in the spinal canal. The experiments were performed in an *in vitro* model of the SAS, using distilled water of density $\rho = 998.2$ kg/m^3 and kinematic viscosity $\nu = 10^{-6}$ m^2/s as working fluid. The model consisted of a $15 \times 15 \times 15$ cm^3 acrylic tank, emulating the cranial vault, connected to a plexiglass tube of length $L = 50$ cm, representing the dura mater. To allow for temporal variations of the local cross-sectional area, needed to accommodate the oscillating flow, a hollow flexible tube of circular section was placed inside, with its distal end anchored at the closed bottom of the rigid tube and its proximal end connected to a peristaltic pump, as indicated in Figure 3.1(a). The flexible tube, with outer radius $R_i = 7$ mm and thickness $h_s = 2$ mm, was made up of rubber (Shore hardness 60A, elastic modulus of approximately

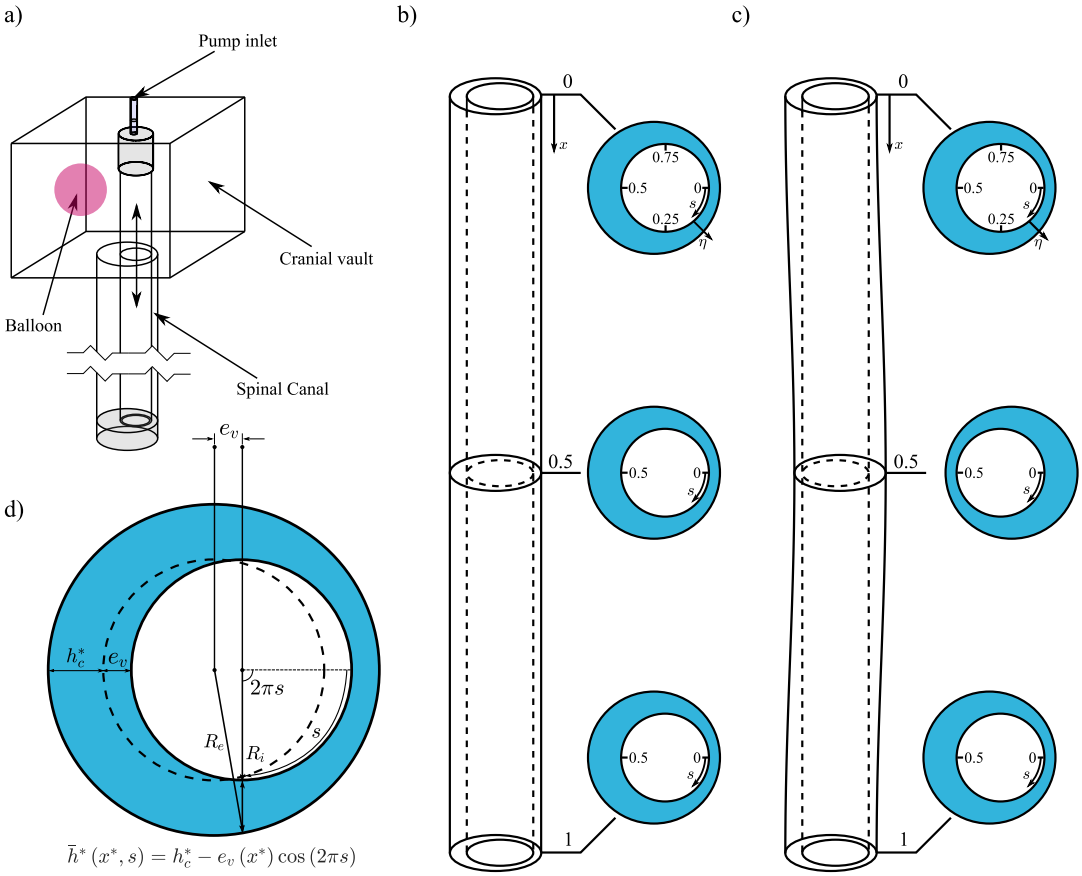

Figure 3.1: a) Schematic representation of the experimental *in vitro* facility of the SSAS. b) Representation of the constant eccentricity canal and c) variable eccentricity canal, with cross sections at planes $x = x^*/L = 0$, 0.5 and 1, showing the dimensionless curvilinear coordinates (x, s, η) which vary from zero to unity, defined in Chapter 2. d) Schematic view of the unperturbed canal width and the eccentricity, e_v, where $e_v(x^*) = e$ in the constant eccentricity canal and $e_v(x^*) = e\cos(2\pi x^*/L)$ in the variable one.

$E_c = 2.2$ MPa and tensile strength of $T_s = 11$ MPa), yielding an elastic wave of characteristic wavelength $(E_c/\rho)^{1/2}/\omega$, larger than the tube length L. The deformation of the inner tube associated with this elastic wave drives the motion in the annular canal. Expressions for the local variation of the cross-sectional area can be derived, as done in Gutiérrez-Montes et al. [47], enabling the elastic wave to be related to the pressure variations along the canal. Note that the speed of the elastic wave in the experiments $(E_c/\rho)^{1/2} \simeq 45$ m/s is comparable to, although somewhat larger than, those reported in the literature, with values ranging from 3.5 m/s to 33.8 m/s for subjects under different conditions [5], [92]–[94].

To explore effects of spinal-cord eccentricity, two different canal geometries were implemented, as indicated in Figure 3.1. Most experiments considered the geometry depicted in Figure 3.1(b), in which the outer tube is a circular cylinder of inner radius $R_e = 10.5$ mm that lies parallel to the inner tube, so that the resulting canal eccentricity, characterized by the distance between their axes, e, remains constant along the canal. The eccentricity can be changed using cams with different eccentricities in the lower and upper parts of the facility, where the flexible tube was anchored. In this case, the resulting undeformed canal width can be approximated by the expression $\bar{h}^*(s) = h_c^*\,[1 - \beta\cos(2\pi s)]$, where $h_c^* = (R_e - R_i) = 3.5$ mm is the average canal width, $\beta = e/h_c^* < 1$ the dimensionless eccentricity, and s is the azimuthal distance

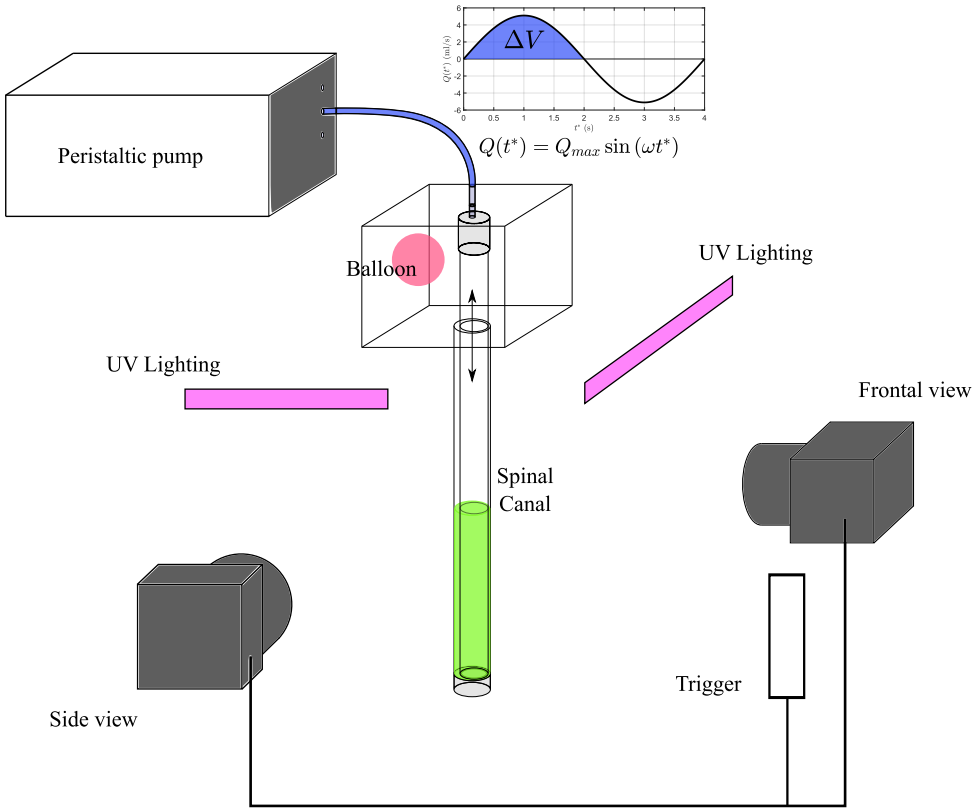

Figure 3.2: Schematic view of the complete setup: *in vitro* model of the SAS, cameras, programmable peristaltic pump and UV lighting. The flow rate wave form provided by the pump is also displayed in the figure with $Q^*(t^*) = Q_{max} \sin(\omega t^*)$, and the corresponding stroke volume, $\Delta V = 2\,Q_{max}/\omega$,

normalized with the perimeter of the inner tube $\ell^* = 2\pi R_i$, with $0 \leq s \leq 1$ and $2\pi s$ being the corresponding azimuthal angle (see Figure 3.1d). A limited set of experiments used the geometrical configuration shown in Figure 3.1(c), involving an outer rigid tube with longitudinal curvature, resulting in a canal eccentricity that varies with the distance from the canal entrance x^* according to $e_v = e\cos(2\pi x^*/L)$ mm, where $e = 1.5$ mm was fixed. In this case, the circular section of the outer tube has inner radius $R_e = 10$ mm, so that h_c^*= 3 mm and $\beta = e/h_c^* = 0.5$. In this case, the canal width varies with both x^* and s according to $\bar{h}^* = h_c^*\,[1 - \beta\cos(2\pi x^*/L)\cos(2\pi s)]$. A programmable peristaltic pump was used to generate a flow rate varying harmonically with time t^* according to $Q^*(t^*) = Q_{max}\sin(\omega t^*)$ of amplitude Q_{max} and angular frequency ω, the latter related to the period T and frequency f by $\omega = 2\pi f = 2\pi/T$. The stroke volume that enters and leaves the flexible tube during each cycle, given by $\Delta V = \int_0^{\pi/\omega} Q^*\,\mathrm{d}t^* = 2Q_{max}/\omega$, was chosen to be a small fraction of the volume contained in the annular canal $V = \pi L(R_e^2 - R_i^2)$, resulting in values of $\Delta V/V \approx 0.018 - 0.084$ similar to those observed in the SSAS [20]. The volume changes induced by the expansions and contractions of the flexible tube were accommodated in the facility thanks to the presence of a compressible air balloon placed inside the tank (see Figure 3.1a).

Two types of experiments were performed using LIF. The first type was used to determine the transport of a solute concentration along the spinal canal, from an initial position $x_0^*/L = 0.5$ from the entrance of the canal. In these experiments, the lower half of the canal (from this initial position $x^*/L = 0.5$ to the closed end of the canal

$x^*/L = 1$) was filled with a neutral buoyant fluorescent dye of sodic fluorescein (emission wavelength $\lambda_{sol} = 541$ nm) with a mass concentration of $C = 1.6$ g/cm^3, whose corresponding molecular diffusivity and Schmidt number are $\kappa \approx 4 \times 10^{-10}$ m^2/s and $S = \nu/\kappa \approx 2500$ respectively. The dye was injected directly into the bottom of the SSAS using a syringe pump with a flow rate $Q_{syr} \approx 50$ mL/s, in order to avoid the formation of jets and inertial effects (the corresponding Reynolds number was Re ≈ 30). The facility was illuminated with an UV LED's lighting system (emission wavelength of $\lambda_{UV} \approx 300$ nm), consisting of a pair of UV LED's lights located on planes $s = 0$ and $s = 0.25$. In each plane, the UV LED's lights were adequately placed to have a homogeneous illumination. The ascending motion of the solute, induced by the peristaltic pump, was recorded with two synchronized reflex cameras, located at the same planes (from now on, plane $s = 0$ will be considered the principal plane or the side view and plane $s = 0.25$ the secondary plane or the frontal view). The resolution of both cameras was 4288×2848 px and the images were saved in 16-bit TIF format. The images were acquired at a sampling period that was an integer-multiplier of the oscillatory period, thus all the images of the tracer dispersion were collected at the same phase of the cycle. During the experiments, the sampling period was adjusted to lie between 2 and 8 times the period of the oscillating flow to assure a minimum of 200 images per test. Thus, we were able to track the front of the filament moving toward the upper reservoir until it reached the canal entrance. The second type of experiments focused on the evolution of the solute concentration in the cranial vault, an important aspect for ITDD procedures targeting brain tumors. In these experiments, the tank was illuminated with a black light and the time evolution of the intensity of the light emitted by the fluorescein reaching the tank was recorded with a CCD camera, with the sampling period selected to be 30 times the oscillatory period T. Since the light intensity is proportional to the solute concentration, these measurements provided a useful quantification of the time evolution of the concentration of solute reaching the cranial vault.

For the two types of experiments described above, the images were processed with a custom MATLAB® routine as described below. Both processes have the same initial steps: first, an initial image without UV-light illumination and presence of fluorescein was used to crop all the images in the Region Of Interest (ROI) for each experiment, being the spinal canal for the first type of experiments and the cranial vault for the second one. Secondly, a background image was subtracted from all the images to eliminate the external noise induced by the UV-light (this image was taken for each test, before filling the facility with the fluorescent dye). Since the wavelength of light emitted by the fluorescein is $\lambda_{sol} = 541$ nm, corresponding to green color, only the green component of the RGB image was processed and converted to a grey-scale image. Afterwards, the minimum value of the intensity of each pixel of the images was subtracted from all the images to enhance the solute detection process and to avoid the generation of shadows and bright areas, which could be wrongly interpreted as part of the solute motion. The pre-processed images were subsequently post-processed to determine the motion of the front of the tracer through application of an image analysis routine based on that developed by [49], [50], [95]. An iterative width-averaged tracer distribution along the canal was computed to obtain an accurate position of the edge of the solute during the whole test. To that end, a threshold intensity value was computed in each iteration. Using this value as upper limit of an image contrast adjustment, the limits of integration in the width-averaged distribution were recomputed, improving the solute concentration tracking method. For the second type of experiments, measuring the temporal evolution of the solute

concentration in the cranial vault, two windows, located at both sides of the flexible tube crossing the reservoir, were selected and the temporal evolution of the averaged value of the tracer concentration in each region was determined. To be able to compare the results, all the experiments were performed under the same conditions of light intensity, UV LED light location and initial solute concentration. This analysis allowed us to obtain not only the time taken for the solute to reach the cranial vault, but also the amount of solute entering it.

No.Exp.	β	f (Hz)	ω (rad/s)	α	$\Delta V/V$	f_s (Hz)	Config.	Type
1	0.14	0.25	1.571	4.39	0.052	0.03125	Str	SSAS
2	0.14	0.25	1.571	4.39	0.084	0.03125	Str	SSAS
3	0.28	0.25	1.571	4.39	0.052	0.05000	Str	SSAS
4	0.28	0.25	1.571	4.39	0.084	0.05000	Str	SSAS
5	0.42	0.25	1.571	4.39	0.052	0.08333	Str	SSAS
6	0.42	0.25	1.571	4.39	0.084	0.08333	Str	SSAS
7	0.14	0.25	1.571	4.39	0.052	0.00833	Str	CV
8	0.14	0.25	1.571	4.39	0.084	0.00833	Str	CV
9	0.28	0.25	1.571	4.39	0.052	0.00833	Str	CV
10	0.28	0.25	1.571	4.39	0.084	0.00833	Str	CV
11	0.42	0.25	1.571	4.39	0.052	0.00833	Str	CV
12	0.42	0.25	1.571	4.39	0.084	0.00833	Str	CV
13	0.42	0.12	0.754	3.04	0.030	0.04000	Str	SSAS
14	0.42	0.60	3.77	6.80	0.030	0.10000	Str	SSAS
15	0.42	1.20	7.54	9.61	0.024	0.20000	Str	SSAS
16	0.42	1.80	11.31	11.77	0.018	0.20000	Str	SSAS
17	0.50	0.35	2.20	4.45	0.052	0.01750	Curv	SSAS
18	0.50	0.35	2.20	4.45	0.052	0.00833	Curv	CV

Table 3.1: Experimental conditions of the different sets of experiments performed. Here, β is the relative eccentricity, f is the oscillatory frequency of the motion, with $\omega = 2\pi f$, $\alpha = \left(h_c^{*2}\omega/\nu\right)^{1/2}$ is the Womersley number, $\Delta V/V \ll 1$ is the ratio between the stroke volume and the total volume in the canal, f_s is the data acquisition frequency, *Str* is straight configuration, *Curv* is curved configuration, and CV is cranial vault.

A large number of experiments were performed using the straight configuration depicted in Figure 3.1(b) for different values of the eccentricity β and the oscillating frequency $\omega = 2\pi f$, the latter characterized in the following plots by the associated Womersley number $\alpha = \left(h_c^{*2}\omega/\nu\right)^{1/2}$ (see Table 3.1). To explore effects of canal eccentricity on solute transport, three values of β were tested, namely $\beta = 0.14$, 0.28 and 0.42, using the straight configuration with $\alpha = 4.39$. Experiments 1 to 6 in Table 3.1 were devoted to the description of the time evolution of the tracer front along the canal, while experiments 7 to 12 focused on the description of the time evolution of the concentration of solute in the reservoir (Cranial vault). In addition, to study the effect of the oscillation frequency, a series of experiments was performed varying α from 3.04 to 11.77 (experiments 13 to 16), for $\beta = 0.42$. The variable-eccentricity configuration of Figure 3.1(c) was used in experiments 17 and 18 for a fixed value of the Womersley number α=4.45. In particular, experiment 17 focuses on the motion of the tracer along the curved SSAS, while experiment 18 aims at describing the evolution of the tracer concentration in the cranial vault.

3.3 Results

The effects of eccentricity and pulsation frequency on the dispersion of a solute are to be investigated below using the *in vitro* experiments and mathematical model. We begin by presenting in Section 3.3.1 the experimental results obtained with the constant–eccentricity model depicted in Figure 3.1(b) for values of β ranging from $\beta = 0.14$ to $\beta = 0.42$ and Womersley numbers ranging from $\alpha = 3.04$ to $\alpha = 11.77$. The configuration with variable eccentricity shown in Figure 3.1(c) is investigated separately in Section 3.3.2 for a Womersley number equal to $\alpha = 4.45$. The measurements will be compared with predictions from the theoretical analysis, which will also be used to describe the velocity field along the canal.

Attention will be focused on the evolution of the solute front. In particular, the temporal variation of the front shape and its advance rate along the canal towards the cranial vault will be registered and compared with predictions obtained from the model with $S \approx 2500$. In presenting the results, the axial coordinate and the time will be expressed in the dimensionless form $x = x^*/L$ and $\tau = \varepsilon^2 \omega\, t^* = \varepsilon^2\, t$, respectively, as is consistent with the theoretical model [39].

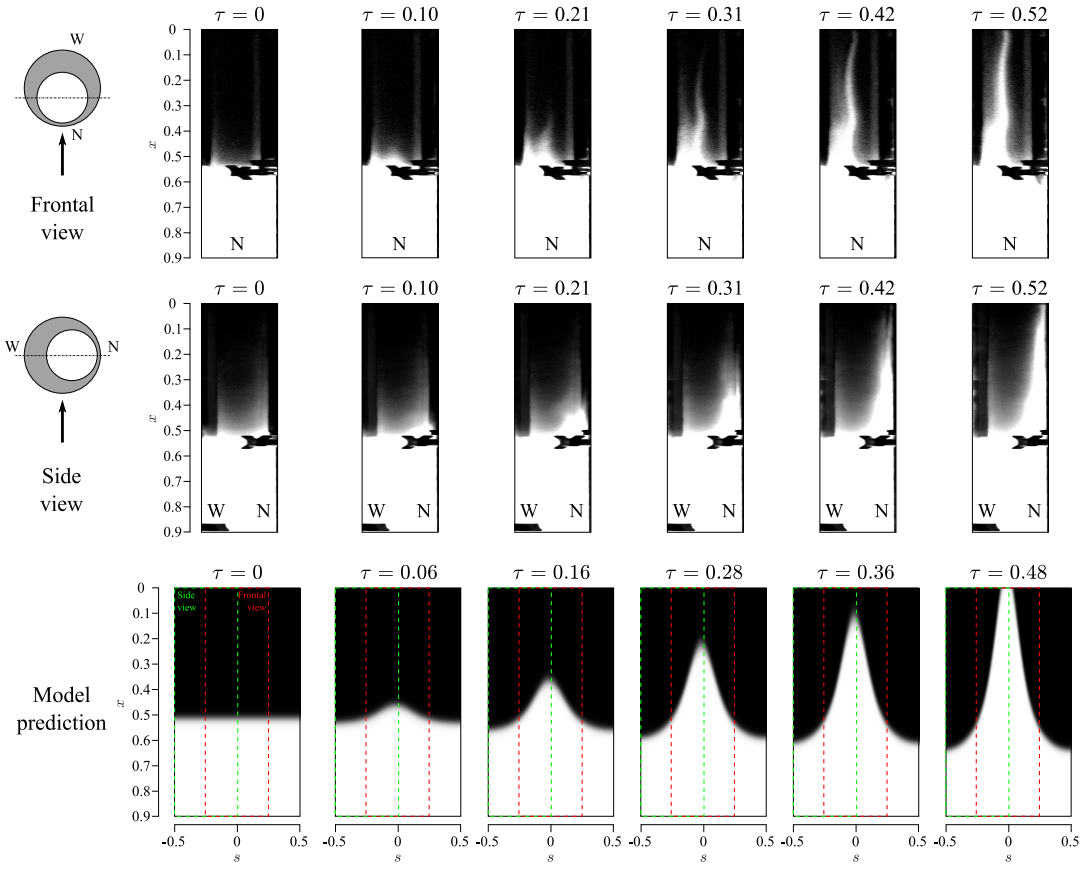

Figure 3.3: Time sequence of the experimental evolution of the solute along the spinal canal for $\beta = 0.42$ and $\alpha = 4.39$ (experimental set 5 in Table 3.1). The upper and central rows show the experimental frontal and side views, while the bottom row shows the results obtained from the mathematical model (the red and green boxes represent the frontal and side views, respectively). Here, W and N indicate the widest and the narrowest sections of the canal.

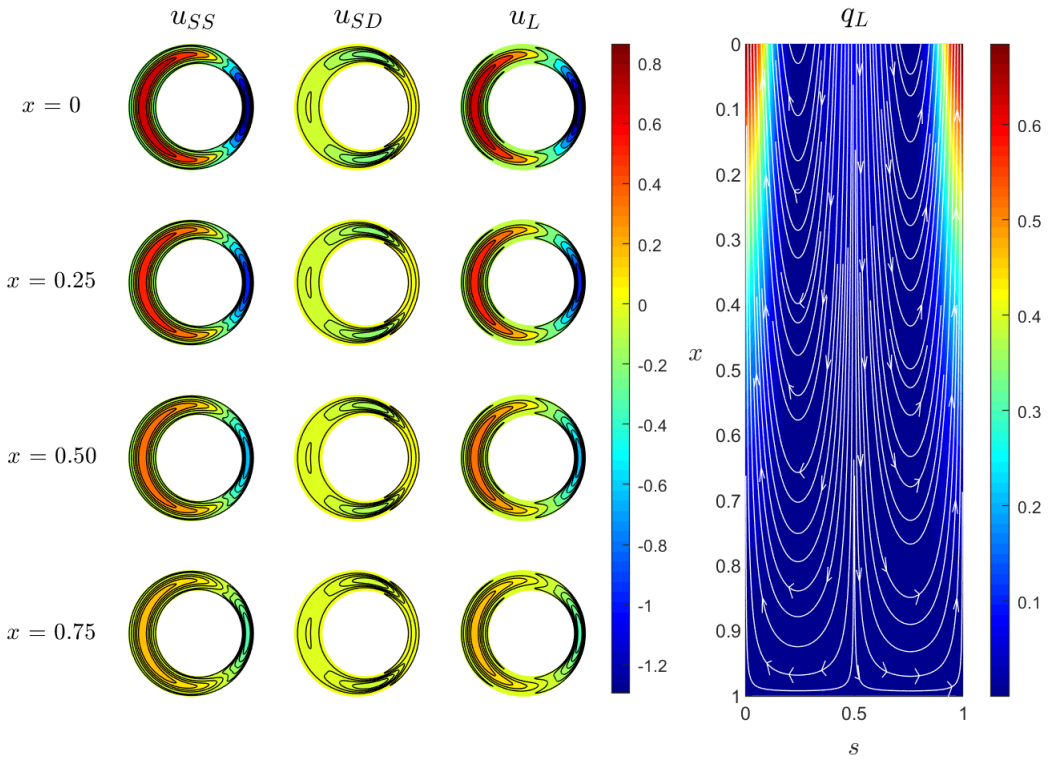

Figure 3.4: Distribution of streamwise components of the steady-streaming, Stokes-drift, and Lagrangian velocity fields at different downstream locations, x. Streamlines obtained for the width-averaged Lagrangian components $\int_0^1 u_L d\eta$ and $\int_0^1 w_L d\eta$ with distribution of width-averaged Lagrangian velocity magnitude, $q_L = \left[\left(\int_0^1 u_L d\eta\right)^2 + \left(\int_0^1 w_L d\eta\right)^2\right]^{1/2}$.

3.3.1 Constant eccentricity configuration: effect of β and α

Let us begin by analyzing the case corresponding to $\beta = 0.42$ and $\alpha = 4.39$, as the reference case. Figure 3.3 shows a sequence of snapshots of the temporal evolution of a solute initially filling the tube from $x = 0.5$ to $x = 1$. The frontal view shows the projection on a vertical plane at $s = 0.25$, where the narrowest section is at the central axis of the view, while the lateral view shows a projection on a vertical plane at $s = 0$, where the widest section is on the left of the image and the narrowest one on the right. Note that, since the experimental images are in fact projections of a three-dimensional view, the abscissa axes do not really show the variable s. The inner, compliant tube can also be seen in the images and should not be confused with the light emitted by the fluorescein. Although perturbed, the ascending motion of the solute is nearly symmetric with respect to the symmetry plane around the narrowest section, as observed in the frontal view. For this configuration, the solute is observed to move upwards (cranial direction) along a small region within the narrowest part of the canal, $s = 0$, whereas it moves towards the distal end (caudal direction) around the widest part of the canal, $s = 0.5$. The decrease in the area close to the widest region is not appreciated in the images because, as previously stated, they show the projection on a plane of a three-dimensional view. Thus, the liquid in front of the narrowest section, whose level is higher, blocks the view of that area. Furthermore, it can be inferred from the time sequences that the front advances with a speed that increases as it gets closer to the cranial vault, as it will be later corroborated.

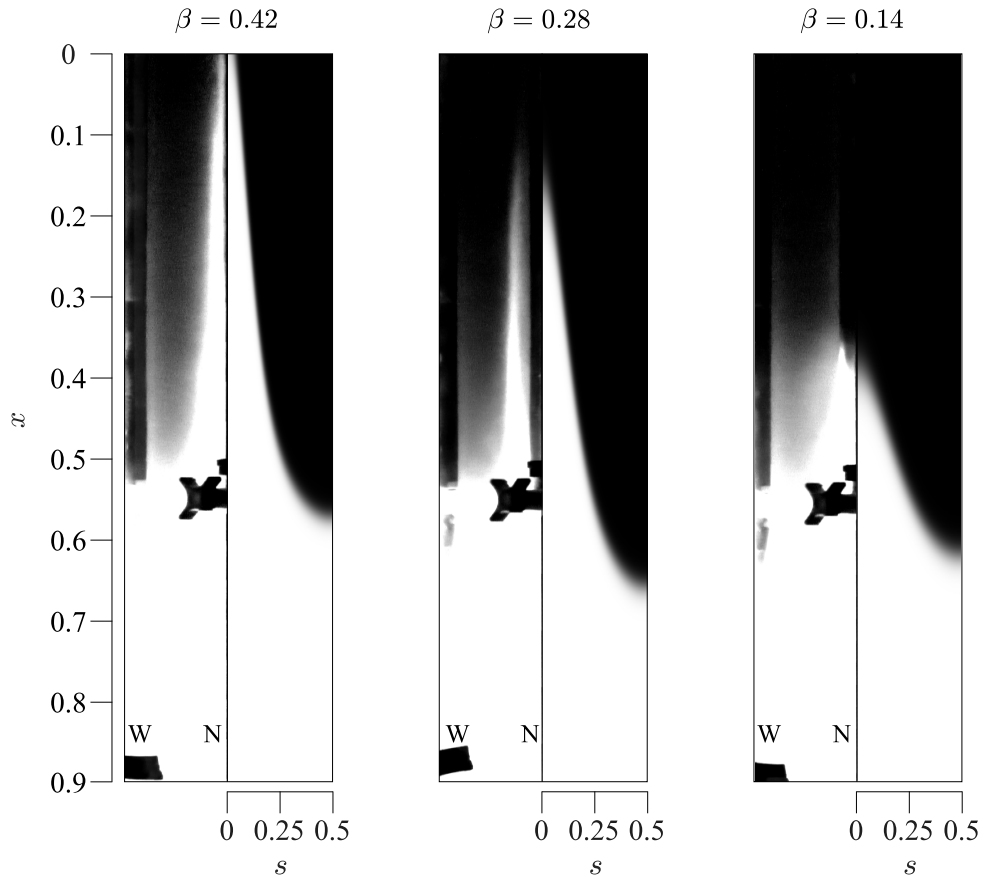

Figure 3.5: Distribution of a solute, initially filling the canal from $x = 0.5$ to $x = 1$, for $\beta = 0.42$, $\beta = 0.28$, and $\beta = 0.14$, at $\tau = 0.48$ in the straight configuration, corresponding to experiments 5, 3 and 1 of Table 3.1, respectively. Experimental results are represented on the left-hand side of the panels while the theoretical predictions obtained integrating Equation (2.4) are represented on the right-hand side. Here, N and W indicate the location of the narrowest and widest sections in the experimental visualizations.

The model predictions show reasonably good agreement with the measurements. In particular, as displayed in the bottom panel of Figure 3.3, the solute exhibits cranial motion along the narrowest region, and descends towards the distal end along the widest region. In addition, the transport velocity is also seen to increase near the canal entrance. The quantitative agreement between the experiments and the model is excellent, as seen by comparing the time needed for the solute to reach the canal entrance as predicted by the model ($\tau = 0.48$) and by the experiments ($\tau \approx 0.52$).

The mathematical model will be used to analyze in detail the experimental results shown in Figure 3.3. Unless otherwise stated, the computations assume a uniform compliance factor $\gamma = 1$. Figure 3.4 shows distributions of the streamwise components of the steady-streaming, u_{SS}, Stokes-drift, u_{SD}, and Lagrangian velocities, u_L, respectively, at different distances from the entrance, x. As it can be observed, the steady streaming motion is directed towards the distal end around $s = 0.5$ (widest section - red) and towards the canal entrance close to $s = 0$ (narrowest section - blue), whereas the Stokes drift shows a downwards movement along $s = 0$ and upwards along $s = 0.5$, the latter becoming larger for intermediate values of s and peaking close to $s = \pm 0.25$. The steady-streaming velocity is significantly larger than the Stokes-drift velocity, so that the resulting distribution of Lagrangian velocity, shown in the third column of Figure 3.4, is similar to that of steady streaming, shown

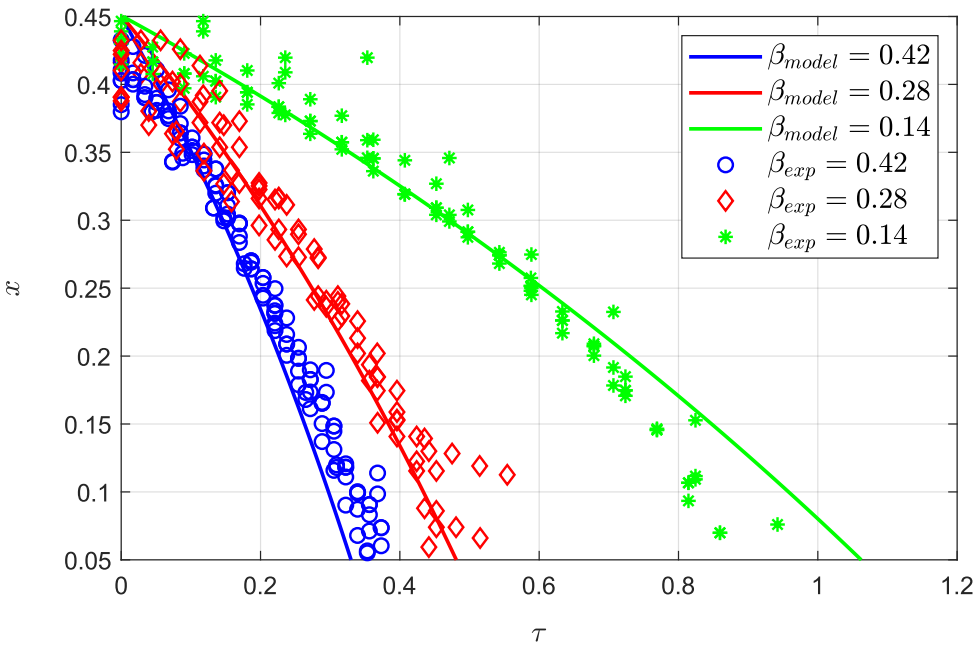

Figure 3.6: Temporal evolution of the solute along the spinal canal for $\alpha = 4.39$ and $\beta = 0.14$, 0.28 and 0.42 respectively (experiments 1-6 in Table 3.1). Symbols represent the experimental measurements and the solid lines the results given by the theoretical model with $\gamma = 1$.

in the first column. The associated induced net convective flow can be characterized by representing the Lagrangian streamlines of the width-averaged values of the axial and azimuthal velocities $\int_0^1 u_L d\eta$ and $\int_0^1 w_L d\eta$ in a $s - x$ plane (see Figure 3.4). A net stationary motion is observed entering the channel and moving down through $s = 0.5$ at a relatively large velocity, as indicated by the proximity of the streamlines. The motion decelerates with the distance from the canal entrance, where the fluid moves with an azimuthal component towards $s = 0$, and begins to rise towards the cranial vault with a speed that increases as it approaches the entrance of the canal (i.e. as x decreases).

The effect of the eccentricity on the transport of a solute was further investigated experimentally by varying the distance between the axes of both cylinders, e, to yield values of β equal to 0.14, 0.28 and 0.42, respectively (see Figure 3.1), while maintaining a constant value of the Womersley number $\alpha = 4.39$. Snapshots at $\tau = 0.48$ are shown in Figure 3.5 for the three values of β and compared with the results obtained from the theoretical model. Two volume ratios $\Delta V / V$ were considered, namely 0.052 and 0.084 (Table 3.1), yielding similar results. From the measurements, it can be observed that, while β hardly affects the flow topology in the range considered, i.e. the solute travels upwards around $s = 0$ and downwards around $s = 0.5$, it has a major impact on the net flow velocity and, thus, the time needed for the solute to reach the cranial vault. As seen in the snapshots for $\tau = 0.48$, increasing the eccentricity results in larger transport velocities, so that the front of the solute distribution, initially located at $x = 0.5$, reaches $x \approx 0.35$ for $\beta = 0.14$, $x \approx 0.12$ for $\beta = 0.28$, and $x \simeq 0$ for $\beta = 0.42$. The right-hand side of each panel in Figure 3.5 shows the corresponding predictions of the solute distribution given by the theoretical model, yielding results in reasonably good agreement with the experimental observations.

To better quantify the effect of β, the time evolution of the solute front as it moves towards the canal entrance, between $x = 0.45$ and $x = 0.05$, is shown in Figure 3.6 for

$\beta = 0.14$, 0.28, and 0.42 and a constant value of $\alpha = 4.39$, both for the experiments and the theoretical model. As it has been previously mentioned, in the range of eccentricities considered here, the solute rises faster as β increases. The plots indicate that the increase in dispersion rate is not linearly proportional to β. For instance, the time needed for the solute to reach the canal entrance is halved when β increases from 0.14 to 0.28, while it is reduced by approximately only 25% when β is increased from 0.28 to 0.42. It is also of interest that the slope of the curves, $-\mathrm{d}x/\mathrm{d}\tau$, increases as x decreases, indicating that the rising velocity increases as the solute approaches the entrance of the canal. All of these features are also captured by the reduced model, with results represented by solid curves in Figure 3.6.

The model was used to further investigate effects of variations of β, with results given in Figure 3.7, including distributions of the axial component of the Lagrangian velocity, u_L, at the entrance of the canal, $x = 0$, for different values of β (Figure 3.7a), as well as the variation with β of the time that the solute takes to travel from $x = 0.45$ to $x = 0.05$ (Figure 3.7b). Peak velocities are seen to initially increase with β, reaching a maximum value at $\beta \simeq 0.54$, for which the associated time needed to reach $x = 0.05$ is correspondingly minimum, as shown in Figure 3.7(b). For values of $\beta \geq 0.54$ the proximity of the walls at $s = 0$ causes the peak velocity to decrease in magnitude, as shown for the case of $\beta = 0.75$ in the contours of velocity displayed in Figure 3.7(a). Similarly, the net flow rate entering/exiting the canal decreases monotonically as β increases in the range $0 \leq \beta \leq 0.54$.

In addition to performing experiments to describe the transport of a solute along the canal, we also characterized temporal evolution of fluorescein concentration at the cranial vault (experimental sets 7-12 in Table 3.1). In these experiments, the temporal evolution of the light intensity emitted by the fluorescein reaching the measuring windows in the reservoir was recorded, $\langle C \rangle(\tau) = 1/A \int_A C \, \mathrm{d}\sigma$. Here, A is the area of the measuring windows and C is the solute concentration, which is proportional to the light emitted by the fluorescein. Figure 3.8 displays the temporal evolution of the mean solute concentration in the interrogation windows in the cranial vault for $\beta = 0.14$, 0.28 and 0.42 corresponding to $\alpha = 4.39$. Here, three different stages of the evolution of the tracer dispersion are presented. In accordance with the results of the solute transport in the *spinal canal* described above, it can be seen that the time at which the fluorescein begins to be detected in the ROI increases as β decreases. Note that, such time does not correspond with τ_c reported in Figure 3.7 since the amount of fluorescein in the ROI must be larger than a given threshold to be detected in these experiments. Nevertheless, it can be observed that the rate at which the solute reaches the cranial vault increases with β, since $d\langle C \rangle / d\tau$ increases with β. Interestingly, the quasi-asymptotic value of the concentration that reaches the cranial vault also increases with β. This result is attributable to the existence of increasing rising velocities at the bottom of the canal for increasing values of β. Quantitative information regarding dispersion times is important in connection with ITDD processes, especially in the case of drugs of short half-life [96].

Effects of the oscillating frequency were investigated in experiments with constant eccentricity $\beta = 0.42$ by varying α from 3.04 to 11.77 (experimental sets 13-16 in Table 3.1). Figure 3.9 shows the distribution of solute, obtained both experimentally (left-hand side of the panels), and using the theoretical model (right-hand side of the panels), at different selected times. The results reveal that variations in α lead to markedly different flow topologies and associated velocities. This strong dependence

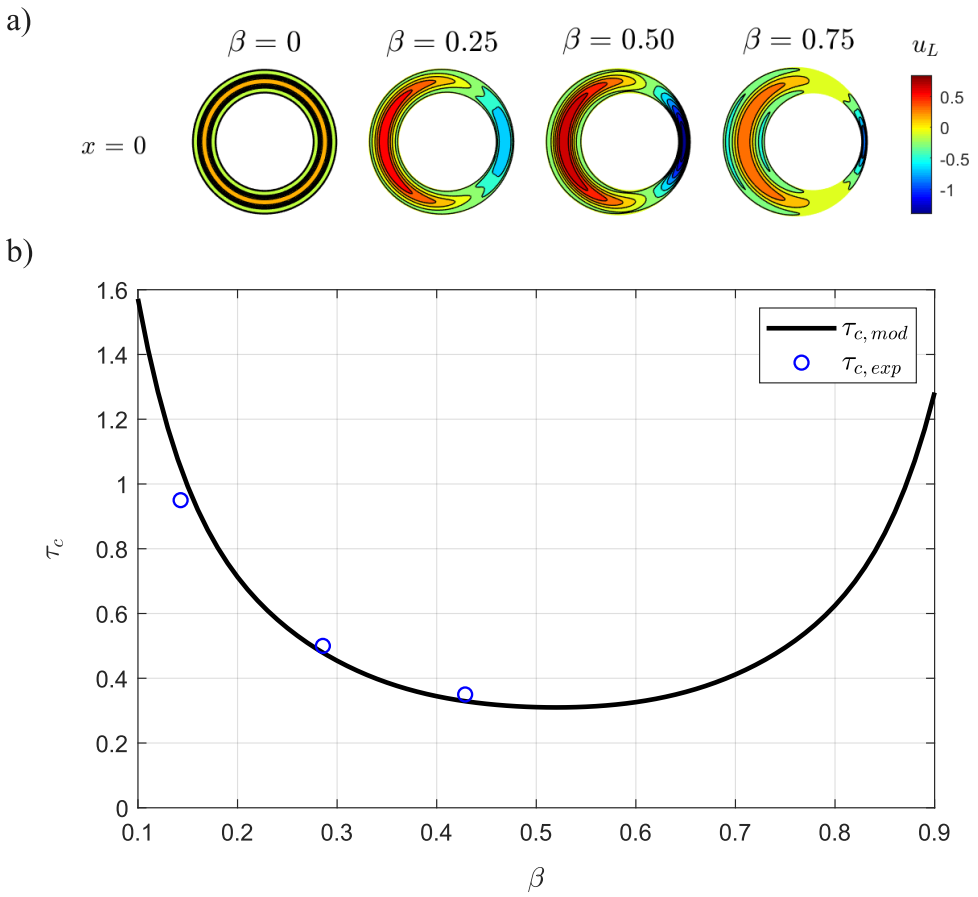

Figure 3.7: a) Contours of the axial component of the Lagrangian velocity, u_L, at the entrance of the canal, $x = 0$, for different values of β, provided by the theoretical model. b) Time taken by the solute to travel from $x = 0.45$ to $x = 0.05$ as a function of β, defined as τ_c. Symbols correspond to the experimental measurements and the solid line represents the model predictions with uniform compliance $\gamma = 1$.

of the steady streaming on the Womersley number is well-known in oscillatory flows over obstacles [97], but had not previously been demonstrated in connection with the flow in the spinal canal. For the lowest values of α, i.e. $\alpha = 3.04$ and $\alpha = 4.39$, the generated net flow rises up along the narrow part of the canal, $s = 0$, along a zone that gets thinner as α increases, while it decreases along the widest region, $s = 0.5$. However, for larger values of α the flow also begins to rise around the widest section (see panel corresponding to $\alpha = 6.80$). Indeed, for intermediate values of α, i.e. $\alpha = 6.80$ and $\alpha = 9.61$, the solute rises along both the narrow and wide regions of the canal, this movement becoming more important in the wide region for increasing values of α, i.e. 9.61. Finally, for the largest value of $\alpha = 11.77$, the flow dynamics inverts almost completely and the solute moves upwards mainly along $s = 0.5$ (widest section). There is a good qualitative agreement between the model and the experiments, although the discrepancies are somewhat larger than those previously found when varying β for $\alpha = 4.39$.

To experimentally quantify the effect of α on solute transport, Figure 3.10 includes the temporal evolution of the uppermost front of a solute initially located at $x = 0.5$. In all cases, the transport velocities are seen to increase at positions closer to the canal entrance. The results reveal a non-monotonic behaviour in the ascending velocity of the solute for increasing values of α, in that the rising velocity displays a pronounced

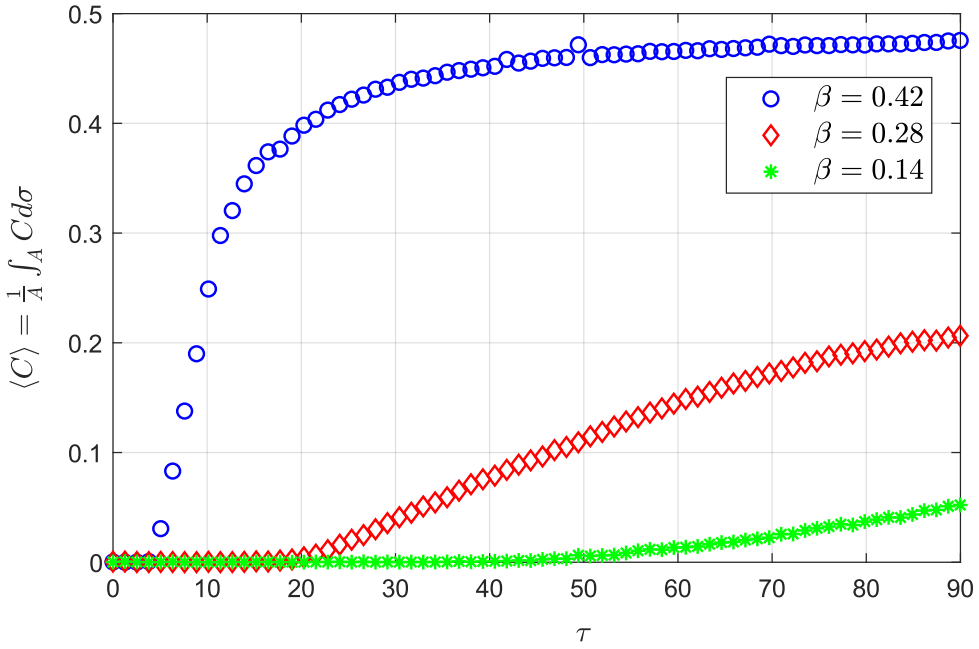

Figure 3.8: Experimental measurements of the temporal evolution of the solute concentration in the cranial vault, $\langle C\rangle(\tau) = 1/A\int_A C\,d\sigma$, for $\alpha = 4.39$ and $\beta = 0.14$, 0.28 and 0.42 respectively (experiments 7, 9 and 11 in Table 3.1).

decrease when α is increased from 3.04 to 6.80 but increases for larger values of α, indicating that the solute transport is less efficient at intermediate values of α, i.e. $3.04 \leq \alpha \leq 9.61$.

The influence of α is further investigated by evaluating the time τ_c taken by the solute, initially located at $x = 0.5$, to travel from $x = 0.45$ to $x = 0.05$, with values represented in Figure 3.11 as a function of α. The figure includes the experimental results, together with predictions obtained with the model using two different compliance functions, $\gamma(x, s)$. First, a uniform compliance $\gamma_1 = 1$, used up to now, has been considered, for which the small deformations of the canal thickness are axisymmetric. Second, to account for possible experimental asymmetries when the compliant tube deforms, a compliance function given by $\gamma_2(s) = 0.2 - 9.6\,(2s^2 - s)$ was also considered, which corresponds to a canal slightly more compliant at $s = \pm 0.25$ than in the symmetry plane $s = 0$ and $s = 0.5$. In both cases, three different regions can be identified in the evolution of τ_c with α. Initially, for small values of α, for which it has been observed that the flow rises through the narrowest section of the canal, τ_c decreases with α. However, for intermediate values of α, for which the solute rises along both the narrow and wide regions of the canal, τ_c increases until it reaches a maximum. Finally, for larger values of α, for which the flow rises through the widest section of the canal, τ_c decreases again as α increases. As seen in Chapter 2, τ_c barely depends on the compliance factor in the range $0 < \alpha < 5$, indicating that the results presented above for $\alpha = 4.39$ and varying values of β, where $\gamma = 1$, were not affected by the function of $\gamma(x, s)$ selected. However, for $\alpha > 5$ the differences in the values of τ_c obtained with the two compliance functions become more relevant. Probably, the most striking difference is the decrease of the local maximum when γ is assumed to depend on s, which takes place at lower values of α. In fact, the local maximum obtained with $\gamma_1 = 1$, corresponding to the case $\alpha = 9.6$, is $\tau_c = 1.79$, while for γ_2 the maximum, now for $\alpha = 7.9$, decreases to $\tau_c = 0.84$. The differences between the

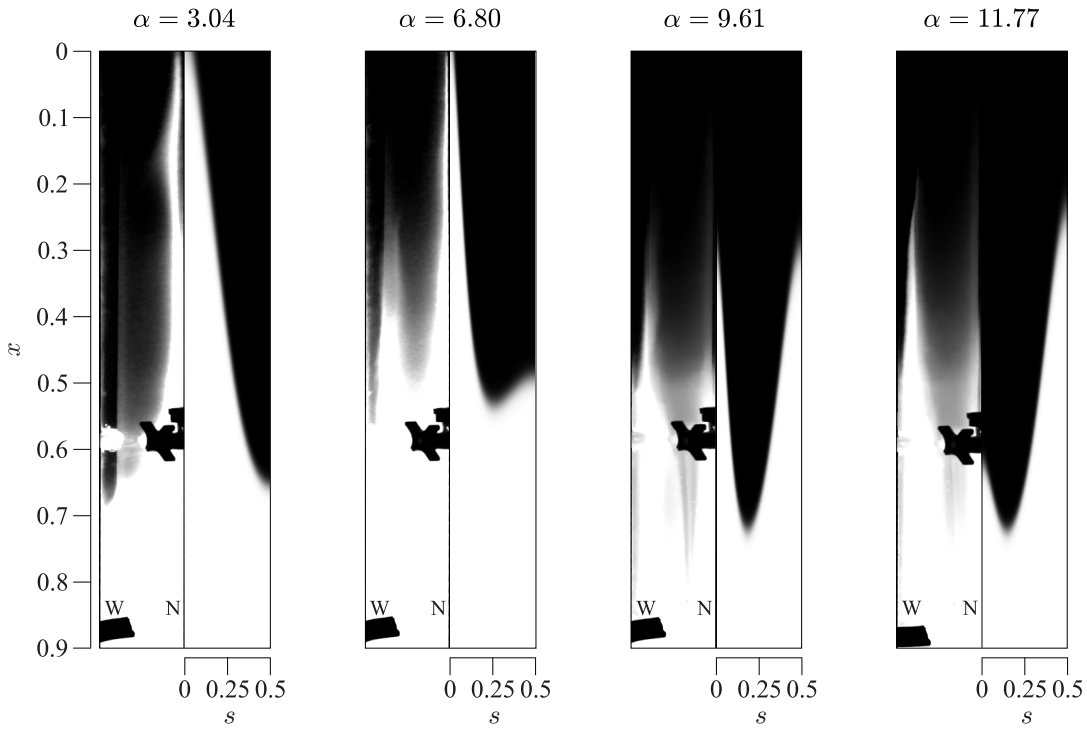

Figure 3.9: Distribution of a solute, initially filling the canal from $x = 0.5$ to $x = 1$, for $\alpha = 3.04$, 6.80, 9.61 and 11.77 where $\beta = 0.42$ in the straight configuration, corresponding to experiments 13-16 of Table 3.1. Experimental results are represented on the left-hand side of the panels while the theoretical predictions obtained integrating Equation (2.4) are represented on the right-hand side.

experiments and the model with uniform compliance γ_1 are significant, especially for $\alpha \geq 6$. Such discrepancies could be explained by the behavior of the flexible tube used in the experiments, stemming from the difficulties to completely preserve the eccentricity, the geometric inaccuracies or the asymmetric behavior of the elastic tube deformation, represented by γ_2 at large α values. However, the results obtained by implementing the model with a non-uniform compliance function, γ_2, agree fairly well with the experimental ones, which also exhibit a local maximum of τ_c although at $\alpha \approx 8$.

3.3.2 Variable eccentricity configuration

As previously discussed, the annular cross-section of the human SSAS displays an eccentricity that varies along the spinal canal, as the position of the spinal cord relative to the dura mater varies. In previous works, these variations have been postulated to play a relevant role in the dynamics of the flow of CSF. While Coenen et al. [22] and Gutiérrez-Montes et al. [47] reported the formation of closed recirculating Lagrangian vortices in the canal that hampered the transport of a solute, no experimental evidence corroborating theses results is currently available, thereby motivating the present analysis, which employs the configuration sketched in Figure 3.1(c), where $\bar{h}(x, s) = 1 - \beta \cos(2\pi x) \cos(2\pi s)$ with $\beta = 0.5$, all experiments performed with $\alpha = 4.45$.

As shown in Figure 3.12, where the experimental/model results are shown in the left-hand/right-hand sides of each panel, for this value of α a volume of solute initially located at $x \leq 0.5$ moves upwards (downwards) around the narrow (wide) part of the canal. In this configuration, at $x = 0.5$ the narrowest section corresponds to

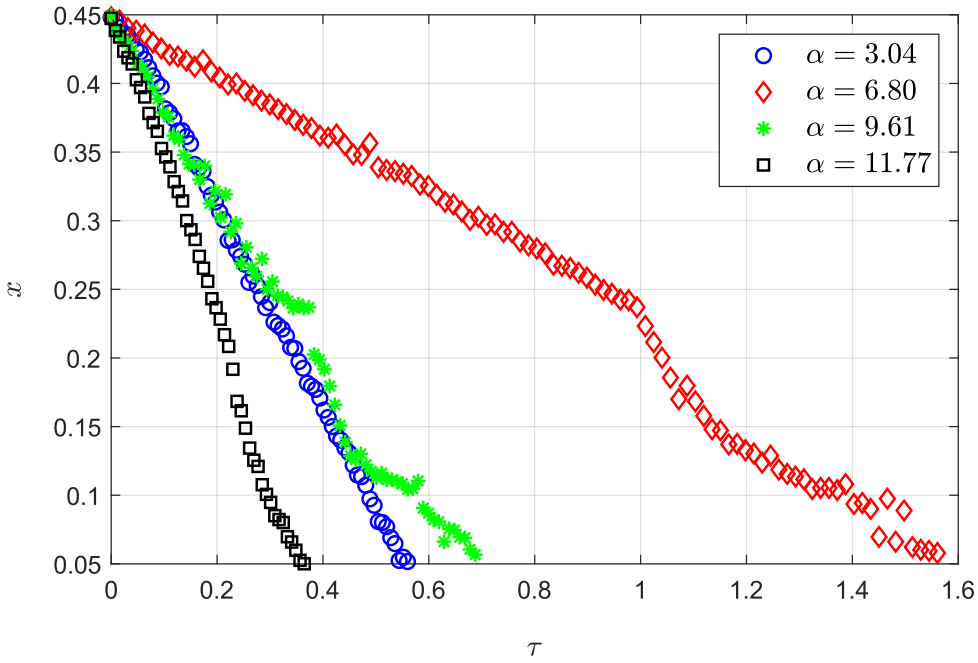

Figure 3.10: Temporal evolution of the solute along the spinal canal for $\beta = 4.2$ and $\alpha = 3.04$, 6.80 and 9.61 and 11.77 respectively (experiments 13-16 in Table 3.1).

$s = 0.5$. Focusing on the upwards motion, one can observe that, as the solute reaches $x \approx 0.27$ ($\tau \approx 0.36$), it slows down dramatically and starts moving azimuthally from $s = 0.5$ towards $s = 1$ due to the change of eccentricity, since the narrow (wide) section changes from $s = 0.5$ ($s = 0, 1$) upstream from that location. This change of eccentricity provokes the formation of closed recirculating regions along the canal [22], [47], so that, instead of continuing its progress along the canal, the solute turns around and moves down through the wide section (see panels at $\tau = 0.68$, 0,82 and 1 in Figure 3.12). Only a small amount of solute is observed to cross the boundary between recirculating regions to rise towards the canal entrance (see the narrow filament of solute moving upwards in the left side of the flexible tube in the experiments, and at $s = 1$ at $\tau = 1$ in Figure 3.12). As expected, the amount of solute reaching the cranial vault is much smaller than in the case of the straight configuration and it takes longer to arrive. The comparisons indicate that the theoretical model accurately predicts the motion of the solute in the canal.

The above results suggest that a variable eccentricity might have a major impact on the flow topology and the associated transport rate along the SSAS. To further quantify this effect, Figure 3.13(a) represents the temporal evolution of the axial location of the solute front as it travels towards the canal entrance determined both experimentally and using the model for the constant and variable eccentricity configurations. It can be observed that, in both cases, the experimental results and the predictions given by the analytical model agree fairly well. Initially, for $x \leq 0.35$, the evolution is similar in both cases, i.e. increasing transport velocity at higher locations (decreasing values of x). However, differently from the constant eccentricity case, in the canal of varying eccentricity the solute motion slows down as it approximates the stagnation point separating the upper and central recirculating regions, located at $x \approx 0.27$. At this position, where the flow turns azimuthally from $s = 0.5$ towards $s = 0, 1$, the fluid hardly advances towards the canal entrance (see the plateau at $0.5 \leq \tau \leq 1.2$ in Figure 3.13a), to subsequently move upwards again in that region,

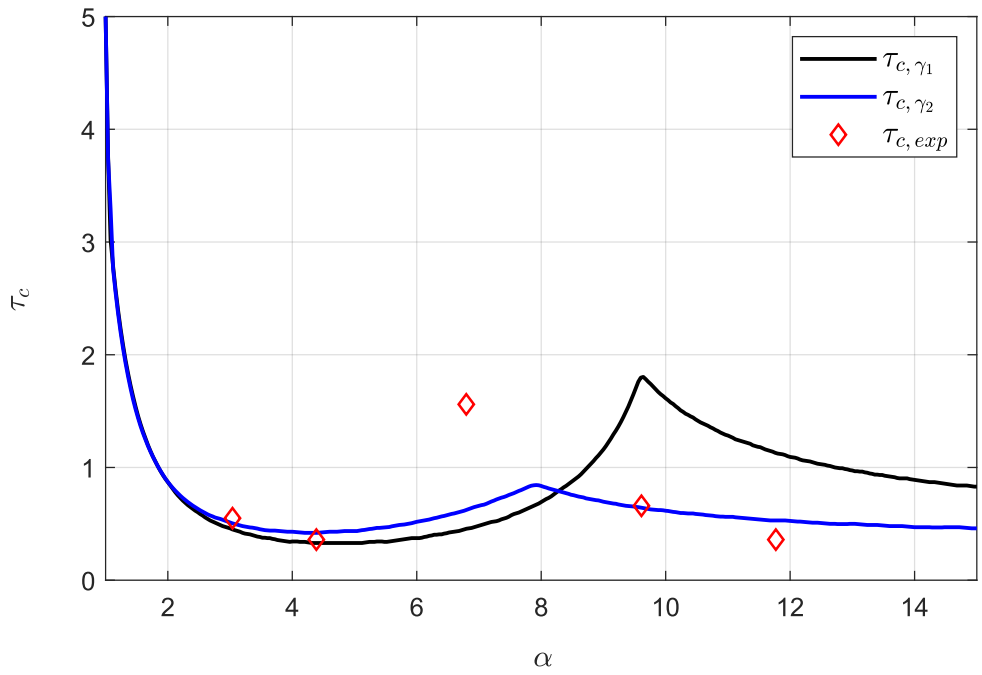

Figure 3.11: Dependence of the time taken by the solute, initially located at $x = 0.5$, to travel from $x = 0.45$ to $x = 0.05$, τ_c, with α. Symbols represent the experimental measurements and solid lines the model predictions obtained for $\gamma_1 = 1$ and $\gamma_2(s) = 0.2 - 9.6\,(2s^2 - s)$, respectively. Here $\beta = 0.42$.

which is now the narrow one, with increasing velocities at locations closer to the cranial vault. As a consequence, the time for the solute to reach the canal entrance, τ_c, becomes three times larger than in the constant eccentricity configuration for the case at hand. Furthermore, not only the advance velocity but also the amount of solute able to reach the entrance of the canal also decreases, since part of the solute remains trapped in the lower recirculating Lagrangian vortex located below $x \approx 0.27$.

Figure 3.13(b) displays the comparison of the time evolution of solute concentration in the cranial vault for the constant and variable eccentricity cases. Note that the rate at which the solute reaches the cranial vault is lower in the case of variable eccentricity, since $\mathrm{d}\langle C\rangle/\mathrm{d}\tau$ is smaller in this case than in the canal with constant eccentricity, as well as the quasi-asymptotic value of the concentration that reaches the cranial vault. In view of the above results, it is evident that the formation of recirculating flow patterns hinders the dispersion of the solute, with important implications concerning the rate at which a drug injected in the lumbar region can reach target locations at the cervical or cerebral level.

3.4 Conclusions

This experimental analysis addresses the motion of CSF in the human SSAS, with attention given to the dispersion rate of a solute injected at the low thoracic and lumbar regions, a key process in connection with ITDD procedures. To that aim, we have conducted *in vitro* experiments in a simplified annular geometry modelling the SSAS, similar to that considered in previous theoretical [29], [39] and numerical [47] studies, as well as in Chapter 2. A programmable pump has been used to induce a harmonic fluid motion in and out of the compliant canal with a stroke volume ΔV

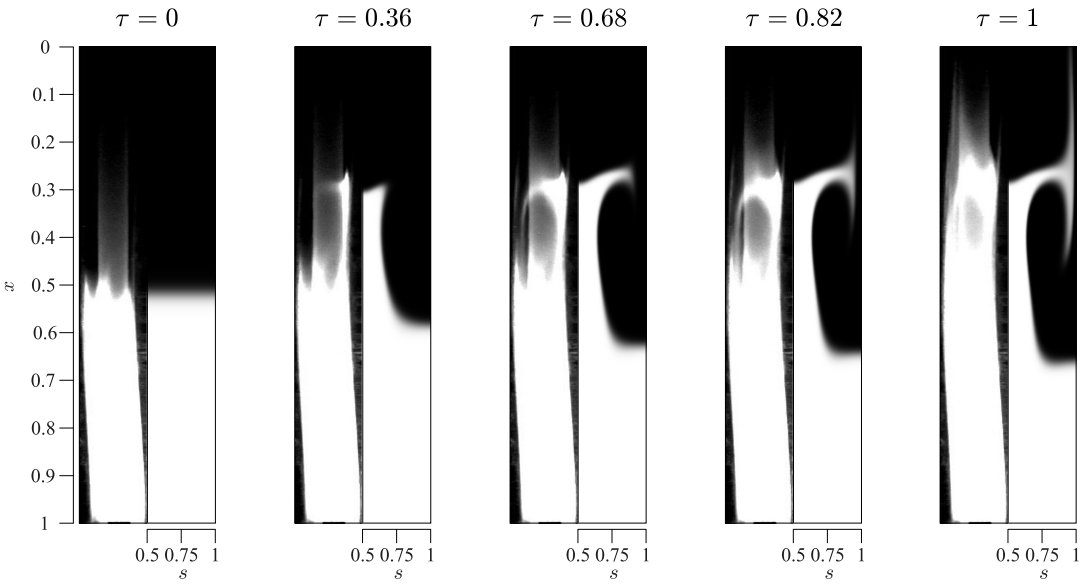

Figure 3.12: Time sequence of the evolution of a solute along a curved canal of unperturbed thickness $\bar{h}(x,s) = 1 - \beta\cos(2\pi x)\cos(2\pi s)$, with $\beta = 0.5$, initially filling the canal from $x = 0.5$ to $x = 1$,corresponding to experiment 17 of Table 3.1. Experimental results are represented on the left-hand side of the panels while the theoretical predictions obtained integrating Equation (2.4) are represented on the right-hand side.

much smaller than the total volume contained in the canal, that being the relevant limiting case for the flow in the SSAS. The solute motion has been characterized with use of LIF techniques. In particular, the effects of the canal eccentricity and the oscillation frequency, the latter measured by the Womersley number, have been assessed in a configuration with uniform eccentricity. A modified geometry allowing for the spatial variation of the cross-section eccentricity, a key feature of the human spinal canal, has also been considered. The results have been compared with predictions obtained using the analytical model developed in Sánchez et al. [29] and Lawrence et al. [39].

The results corroborate the existence of a slow net transport rate, with characteristic times of order $\varepsilon^{-2}\omega^{-1} \gg \omega^{-1}$, which is regulated by the convective transport driven by the time-averaged Lagrangian velocity (i.e. the sum of the Eulerian steady-streaming velocity and the Stokes-drift velocity) and, to a lesser extent, by the action of molecular diffusion across the SSAS [39], [47]. In the constant-eccentricity configuration, variations of the eccentricity are seen to yield significant variations in the induced transport velocities and associated amounts of solute reaching the canal entrance, with the solute transport achieving peak rates for intermediate values of $\beta \sim 0.5$. Variations in the Womersley number are seen to result in important changes in the flow topology, in addition to the flow velocities. In particular, the motion of solute was found to occur towards the cranial vault (bottom) in the narrow (wide) region of the canal for $\beta = 0.42$ and $\alpha \approx 3$, whereas it occurred in the opposite direction for $\beta = 0.42$ and $\alpha \approx 11$. On the other hand, the measurements conducted using a variable eccentricity configuration revealed the formation of recirculatory Lagrangian cells along the canal. As a consequence, part of the solute remained trapped inside these cells, thus hindering its transport towards the cranial vault. The results of this study are important in guiding future developments of predictive tools to assist clinicians and to evaluate the effectiveness of ITDD processes.

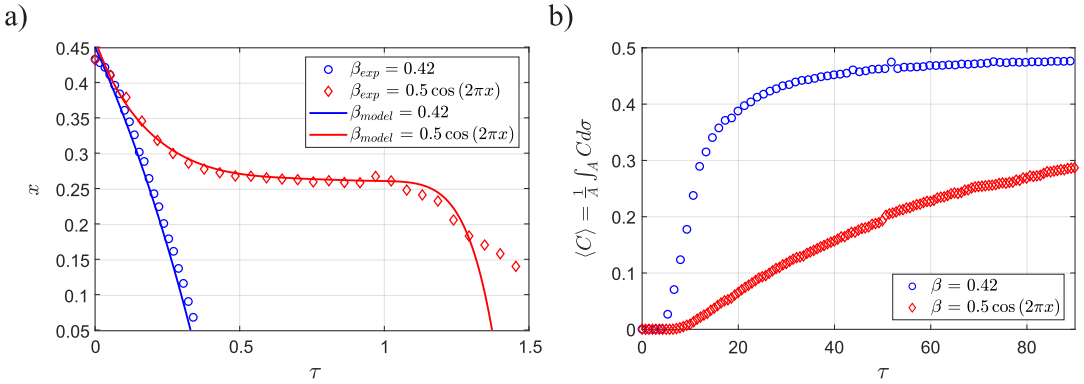

Figure 3.13: a) Temporal evolution of the solute along a constant eccentricity canal of $\beta = 0.42$ (experiment 5 in Table 3.1), and a canal whose eccentricity varies with x as $\beta\cos(2\pi x)$, with $\beta = 0.5$ (experiment 17 in Table 3.1), for $\alpha \approx 4.4$. Symbols represent the experimental measurements and the solid lines the results given by the theoretical model with $\gamma(x, s) = 1$. b) Experimental measurements of the temporal evolution of the solute concentration in the cranial vault, $\langle C\rangle(\tau) = 1/A\int_A C\,d\sigma$, for the constant and the variable eccentricity canals (experimental sets 11 and 18 respectively in Table 3.1).

Part II

Microanatomy effects on the CSF flow in the spinal canal

Chapter 4

Oscillatory flow around circular posts: on the effect of microanatomy

This chapter focuses on the experimental characterization of the time-averaged flow around circular posts, present in many different problems, including that of CSF around bundles of nerve roots in the spinal canal. The main experimental configuration consists of a circular post of radius a, confined by two parallel plates, separated a distance $2h$, being the canal aspect ratio $\lambda = h/a = 2$. An oscillatory flow of an incompressible fluid of density ρ and kinematic viscosity ν is considered, where the flow frequency ω and amplitude U_∞, as well as the waveform, have been varied. The fluid motion is mainly characterized by the corresponding Womersley number $\alpha = (a^2\omega/\nu)^{1/2} \in [5, 11]$ and the dimensionless stroke length $\varepsilon = U_\infty/(\omega a) \leq 1$. As a result of this motion, time-averaged flow patterns are generated, featuring the formation of different numbers of recirculating vortices of variable shape or rotation intensity. The resulting patterns, which vary within the range of parameters herein considered, have been partly compared with analytical predictions obtained for the limit $\varepsilon \ll 1$, which show good agreement even for finite values of ε. Finally, the analysis has been further extended to assess the flow in the presence of a linear array of posts separated a dimensionless semi-distance $\ell = d/a = 2$, where d is the semi-distance between the axes of two contiguous posts.

This Chapter is comprised, in part, in the paper: "Steady-streaming around a cylindrical post confined between two parallel plates", by A.J. Bárcenas-Luque, F. Moral-Pulido, C. Gutiérrez-Montes, W. Coenen, A.L. Sánchez & C. Martínez-Bazán, under preparation.

4.1 Introduction

The CSF motion and the transport of a solute along the SSAS have been studied in previous works [25], [29], [39] and analysed in previous chapters of this dissertation (see Chapter 2 and Chapter 3). These studies consider a clear spinal canal, free of obstacles inside it. However, it is well known that a real spinal canal features the presence of microanatomical elements along it, such as nerve roots, denticulate ligaments or trabeculae [98], [99]. The effect of such elements has been accounted for in different manners in numerical studies [100], [101], analytical developments [21] or experimental researches [50]. In any case, the inclusion of the microanatomy constitutes an important problem in accurately characterizing the CSF dynamics, which

also has important implications in different applications, such as ITDD protocols.

The oscillatory flow around a confined post or a linear array of confined posts might be a first step to include the effect of microanatomy in the characterization of the CSF motion in the SSAS. In that regard, the flow of a harmonic stream of velocity $u_\infty(t^*) = U_\infty \cos \omega t^*$ interacting with a cylinder is known to induce a time-averaged steady flow [89] around the solid body. The latter flow depends on the fluid properties, namely the density ρ and kinematic viscosity ν, the flow frequency ω and amplitude U_∞ and the characteristic length of the obstacle a (the radius of the post), which define the two controlling flow parameters, i.e. the dimensionless stroke length, $\varepsilon = U_\infty/(\omega a)$, and the Womersley number, $\alpha = \left(a^2\omega/\nu\right)^{1/2}$, being the associated Reynolds number $Re = \varepsilon\alpha^2$. This problem has been extensively studied for circular cylinders in the limit $\varepsilon \ll 1$ [89], [102]–[106]. Although the circular shape has been mainly investigated, other configurations, shapes and parametric ranges have also attracted scientific interest through the years [38], [107]–[110]. In addition, the latter works have been extended to account for the effect induced by anharmonic waveforms [111]–[114], for which significantly different flow patterns to those obtained in circular cylinders have been found. However, to our knowledge, the oscillatory flow around a confined post or a linear array of confined posts in the range $\alpha \in [1 - 10]$, $\varepsilon \leq 1$, the relevant one in the characterization of the CSF motion and the transport of solutes in the spinal canal, has not been yet addressed.

In the following, we present an experimental study of the time-averaged Lagrangian flow around a confined cylindrical post at first, extended to a linear array of circular elements. To that end, the analytical description of the problem is briefly presented in Section 4.2. Afterwards, Section 4.3 introduces the experimental facility and techniques employed to obtain the steady flow in detail, being the corresponding results reported and discussed in Section 4.4. Finally, Section 4.5 is devoted to the conclusions.

4.2 Problem description

The presented problem focuses on the analysis of the oscillatory flow of an incompressible, Newtonian fluid around a single (or a linear array of) cylindrical post(s), confined by two planar plates at the top and bottom boundaries. As seen in the schematics of Figure 4.1, the fluid, with well-known density ρ and kinematic viscosity ν, moves back and forth with width-averaged velocity $u_\infty(t^*) = U_\infty \cos(\omega t^*)$, where ω is the oscillatory frequency and U_∞ is the velocity amplitude (note that, an anharmonic waveform stream will be also considered below). Regarding the geometrical set, each post consists of a cylinder of radius a, semi-height h and semi-distance between the axes of contiguous posts d. Therefore, two controlling flow parameters are defined, namely the dimensionless stroke length ε and the Womersley number α, previously defined, together with two geometrical parameters: the aspect ratio of the canal, $\lambda = h/a$, and the dimensionless inter-post semi-distance, $\ell = d/a$. In this chapter, the governing parameters have been ranged $\varepsilon \leq 1$, $\alpha \in [5, 11]$, $\lambda = 2$ and $\ell = 2$, with $\ell \to \infty$ in the case of a single post.

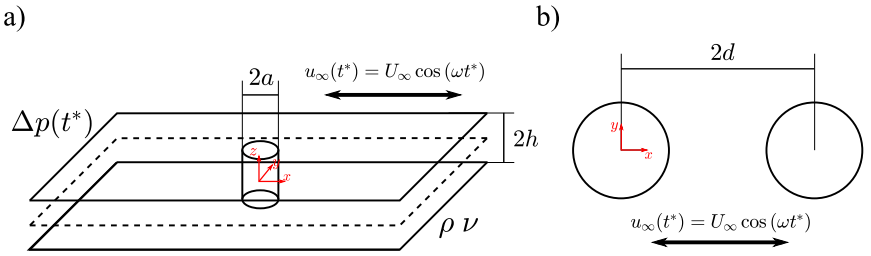

Figure 4.1: a) Scheme of the flow around a cylindrical post confined between two parallel plates, including the corresponding variables. b) Top schematic view of the oscillatory fluid flow around a linear array of cylindrical posts, separated a distance $2d$ among each other.

The problem is governed by the Navier-Stokes equations for an incompressible flow, which can be made dimensionless with use of a, ω^{-1}, U_∞ and $\rho\omega a U_\infty$ as characteristic length, time, velocity and pressure scales, to give

$$\nabla \cdot \mathbf{v} = 0, \tag{4.1}$$

$$\frac{\partial \mathbf{v}}{\partial t} + \varepsilon \mathbf{v} \cdot \nabla \mathbf{v} = -\nabla p + \frac{1}{\alpha^2} \nabla^2 \mathbf{v}, \tag{4.2}$$

subject to the non-slip condition at the solid boundaries, and the oscillatory fully-developed flow at the far-field (note that the far field can vary between $r = \sqrt{x^2 + y^2} \to \infty$ in the single post configuration, and $y \to \infty$ in the case of a linear array of posts, wherein the posts are also separated $2d$ spatially periodic in the x direction).

In the limit $\varepsilon \ll 1$, a solution for the flow around a post has been obtained using perturbation analysis by introducing expansions in powers of ε, denoting the fluid properties as $\phi(x, y, t) = \phi_0(x, y, t) + \varepsilon \phi_1(x, y, t) + \cdots$, as seen in previous chapters. In this case, the velocity is purely oscillatory at leading order, and includes a steady component, denoted as steady streaming, at the first-order corrections. The Lagrangian motion, which also accounts for the additional contribution of the Stokes drift, has been obtained from the leading-order Eulerian velocity field as shown in [38], [115].

4.3 Experimental setup

In this study, *in vitro* experiments were carried out to characterize the time-averaged flow patterns induced in the parametric range considered, being, as aforementioned, $\varepsilon \in [0.2, 0.5]$, $\alpha \in [5, 11]$, with fixed geometrical parameters $\lambda = h/a = 2$. Two types of experiments were performed: the first one focused on the flow field around a single post and the second one on the flow around a linear array of 5 posts separated a dimensionless semi-distance $\ell = d/a = 2$. Table 4.1 summarizes the flow conditions and waveform used in the different experiments for both, the single post and the array of five posts. To that aim, the facility shown in Figure 4.2 was employed, using distilled water with density $\rho = 998.2$ km/m^3 and kinematic viscosity $\nu = 10^{-6}$ m^2/s as the working fluid. The model consisted of an acrylic prismatic channel, of volume $V = 20 \times 10 \times 2$ cm^3, being the length $L = 20$ cm, width $2w = 10$ cm and height $2h = 2$ cm, respectively. The base of the tank was covered with black adhesive vinyl, which sets the background of the images and avoids the light reflections in the experiments. A vertical cylindrical post of radius $a = 5$ mm was placed in the middle of

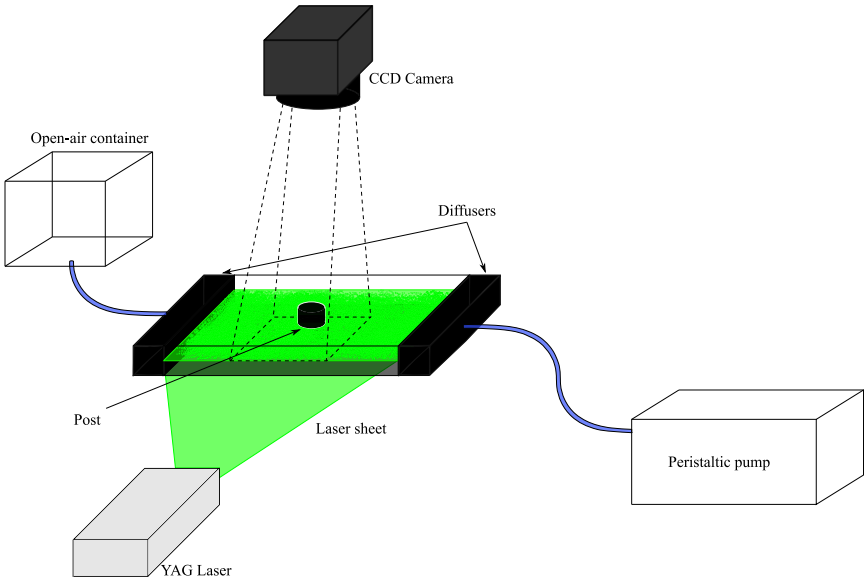

Figure 4.2: Schematic view of the full experimental facility (experimental model, programmable peristaltic pump and open-air container) and the image acquisition setup (YAG laser and CCD camera).

the canal, so that the canal aspect ratio results $\lambda = h/a = 2$. This radius was small enough to avoid any influence from the lateral confining walls on the fluid motion near the post, being the distance between the centre of the cylinder and the walls equal to $w = 5$ cm $= 10$a. This model configuration was also extended to consider a linear array of 5 posts, which were arranged aligned with the fluid motion. These elements were separated a distance $2d = 20$ mm, being the dimensionless inter-post semi-distance $\ell = d/a = 2$. The *in vitro* model was connected to a programmable peristaltic pump on one side, which generates the oscillatory flow, and an open-air container on the other side, to allow the displacement of the stroke volume. The programmable pump allowed to vary relevant parameters of the flow: the stroke volume, ΔV, the oscillatory frequency, $f = \omega/(2\pi)$, and the waveform (from a harmonic sinusoidal wave to a MRI-based anharmonic one). The fluid entered and exited the canal through nozzles placed at the inlet and outlet sections, which also included a piece of foam, that were used to homogenize the flow.

The conducted experiments aimed at characterizing the time-averaged flow, induced by the oscillatory stream. To that end, PTV techniques were employed, where hollow glass spheres of diameter $\phi_p = 10$ µm were used as tracking particles. The experiments consisted of long-duration sequences of black and white phase-averaged images. These series, which contain from 130 to 180 images, were taken with a CCD camera with resolution of 2048×2048 px. This camera was synchronized with a pulsed YAG laser, that emitted a horizontal planar green sheet ($\lambda_{laser} = 541$ nm) of width $\delta h < 1$ mm, and which was used to create a measurement plane at $z = 0$. The complete facility, including the pumping and acquisition systems, is schematically represented in Figure 4.2.

The acquired images were processed to obtain the pathlines followed by the particles, as well as the corresponding velocity and vorticity fields obtained from PIV measurements. The processing was coded in MATLAB®. To obtain the pathlines, a background image was subtracted to all images, which were then added up to create

Experiment	Waveform	f (Hz)	α	U_∞ (mm/s)	ε
1	Sine	0.16	5	1.005	0.2
2	Sine	0.24	6	1.508	0.2
3	Sine	0.32	7	2.01	0.2
4	Sine	0.40	8	2.51	0.2
5	Sine	0.50	9	3.14	0.2
6	Sine	0.64	10	4.02	0.2
7	Sine	0.78	11	4.90	0.2
8	Sine	0.16	5	2.51	0.5
9	Sine	0.24	6	3.77	0.5
10	Sine	0.32	7	5.03	0.5
11	Sine	0.40	8	6.28	0.5
12	Sine	0.50	9	7.85	0.5
13	MRI	0.16	5	1.005	0.2
14	MRI	0.25	6	1.508	0.2
15	MRI	0.32	7	2.01	0.2
16	MRI	0.40	8	2.51	0.2
17	MRI	0.50	9	3.14	0.2
18	MRI	0.625	10	4.02	0.2
19	MRI	0.80	11	4.90	0.2
20	MRI	0.16	5	2.51	0.5
21	MRI	0.25	6	3.77	0.5
22	MRI	0.32	7	5.03	0.5
23	MRI	0.40	8	6.28	0.5

Table 4.1: Experimental conditions of the different sets of experiments performed. Here, $\alpha = \left(a^2\omega/\nu\right)^{1/2}$ is the Womersley number, f is the oscillatory frequency of the motion, with $\omega = 2\pi f$, U_∞ is the peak velocity of the CSF motion for the harmonic waveform, and the harmonic equivalent peak velocity of the CSF motion for the anharmonic waveform, and $\varepsilon = (U_\infty/\omega)/a$ is the small parameter. The waveform indicated as 'Sine' is a harmonic wave and that indicated as 'MRI' corresponds to an anharmonic cardiac signal obtained from Magnetic Resonance Imaging.

a cumulative image that revealed the formation of the secondary steady flow patterns in each experiment. In the case of the Lagrangian velocity and vorticity fields, a PIV analysis was conducted using the toolbox MATLAB®PIVlab GUI [116]. In this case, after creating a mask for the cylinder (to eliminate the solid regions), a high-pass filter of window size larger than 150 px was used, to avoid non-uniform illumination in the background, in combination with an automatic contrast adjustment. The windows size was modified depending on the time-averaged velocity of the particles, to accurately obtain the velocity and vorticity fields. Finally, the results were calibrated using the diameter of the cylinder, $2a$, as the characteristic length and the period, $T = 1/f$, as the characteristic time.

4.4 Results

In this section, results from *in vitro* experiments, accompanied with complementary analytical predictions, are presented to characterize the time-averaged flow induced by the interaction of an oscillatory stream and a single post as well as an array of posts. First, Section 4.4.1 considers the effect of the Womersley number, α, for small

stroke lengths ($\varepsilon \simeq 0.2$), which also includes comparisons with analytical predictions obtained in the limit $\varepsilon \ll 1$. These results are extended to order unity values of ε in Section 4.4.2, for which the asymptotic description in powers of ε, for $\varepsilon \ll 1$, is no longer valid. The analysis in the aforementioned sections is conducted assuming a harmonic sinusoidal wave. In Section 4.4.3 the study is extended to the analyze the time-averaged flow induced by an anharmonic oscillatory wave, similar to that found in realistic CSF flows, as induced by pressure fluctuations generated by cardiac cycle. Finally, the time-averaged flow originated by the presence of an array of posts aligned with the flow oscillation axis is briefly described in Section 4.4.4.

4.4.1 Effect of the flow frequency: α

The presence of a cylinder of radius a inside an oscillatory stream of velocity $u_\infty(t^*) = U_\infty \cos(\omega t^*)$ induces a time-averaged steady motion in the parametric range considered herein, i.e. $\varepsilon = (U_\infty/\omega)/a \leq 0.5$, $\alpha = \left(a^2\omega/\nu\right)^{1/2} \sim \mathcal{O}(1)$, with $Re = \varepsilon\alpha^2 \leq 40$.

For small values of $\varepsilon \ll 1$, the motion can be described as the sum of a zero-averaged purely oscillatory velocity field and a first-order correction, whose non-zero average is denoted steady-streaming velocity. The latter description, although strictly valid for $\varepsilon \ll 1$, has been recently reported to provide results that remain reasonably accurate for finite values of ε, close to unity, for a linear array of circular cylinders [38]. The Eulerian velocity field of the two-dimensional flow, $\lambda = \infty$, has been described by Holtsmark et al. [102] or Chong et al. [117]. Furthermore, the description of the long-time scale motion of a fluid particle includes the additional contribution of the Stokes drift [117] that, in combination with the steady streaming, yields the mean Lagrangian velocity field. The Stokes drift has been found to be comparable to the steady streaming for $\alpha \leq 1$, but negligible otherwise [118]. In the case at hand, since the values of α experimentally considered are ranged 5 to 11, it is expected that the time-averaged Eulerian and Lagrangian velocity fields almost coincide in the cases reported in the present chapter for $\lambda = 2$.

In general terms, results reveal that, as happens in the two-dimensional case, the Lagrangian mean motion in the horizontal symmetry plane $z = 0$ shows identical recirculation patterns in the four quadrants. Consequently, for the single post case, results in only one quadrant will be reported in the following, see Figure 4.3. Similarly, in this configuration, two distinguished flow topologies can be identified. Thus, for values of the Womersley number below a critical one $\alpha < \alpha_c$, a sole vortex forms in each quadrant (left panels in Figure 4.3), which, in the first quadrant, rotates in clockwise direction, i.e. flow towards the post along the stream's oscillation axis $y = 0$ and away from the post along the antisymmetry axis $x = 0$. For values larger than the critical one $\alpha > \alpha_c$, a secondary external counter-rotating vortex appears, that, differently from what happens in the two-dimensional flow, in this case is closed due to the presence of the confining walls (right panels in Figure 4.3). The external vortex encloses the internal one close to the wall of the post at distances that decrease as α increases. The presence of the plates at the top and bottom boundaries has also an impact on the critical value α_c at which such flow topology change takes place. Specifically, this value has been found to increase as $\lambda = h/a$ decreases, being $\alpha_c \simeq 6.08$ in the infinite cylinder case [102], $\lambda = \infty$, and $\alpha_c \simeq 8.5$ in the present configuration, $\lambda = 2$. In addition, as observed in the theoretical analysis, the time-averaged flow becomes three-dimensional, and is characterized by the formation of two additional recirculation regions in the planes $x = 0$ and $y = 0$, although this

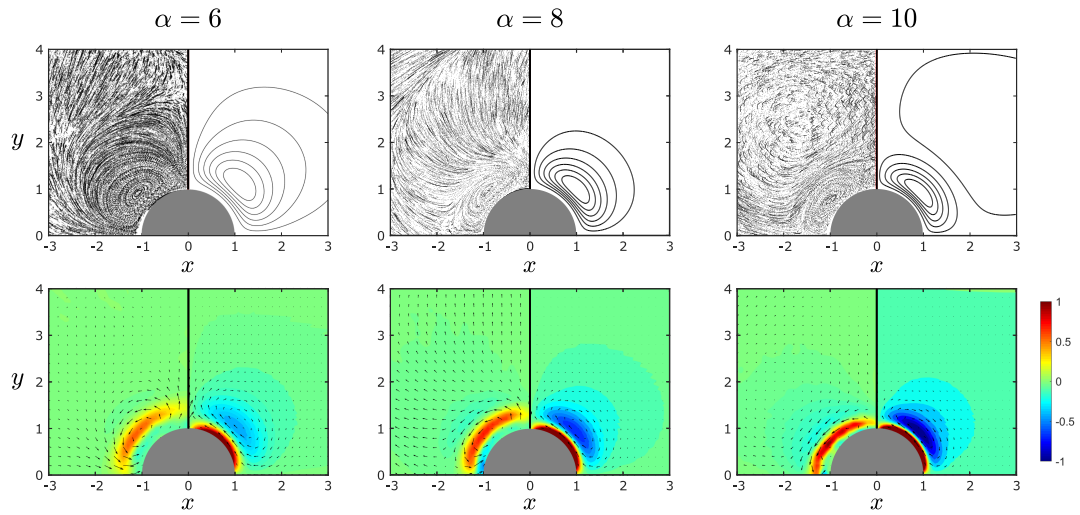

Figure 4.3: Steady pathlines (top row) and velocity + vorticity fields (bottom row) of the fluid around a single cylindrical post at different values of α. Left side of each panel corresponds to the experimental measurements ($\varepsilon = 0.2$) and right side to the analytical predictions ($\varepsilon \ll 1$).

matter will not be experimentally explored, due to optical access limitations. To illustrate theses observations, Figure 4.3 presents the comparison between the time-averaged analytical ($\varepsilon \ll 1$) and experimental ($\varepsilon \simeq 0.2$) results. In particular, the first row shows pathlines of the mean Lagrangian motion obtained experimentally, left or second quadrant, and analytically, right or first quadrant, for values of $\alpha = 6$, 8 and 10, in columns from left to right, respectively. The first two columns display flow topologies corresponding to $\alpha < \alpha_c$, whereas a flow topology change becomes apparent for $\alpha = 10$, where a second external counter-rotating vortex appears, which confines the inner vortex to the high-vorticity Stokes layer close to the post. In the second row, the vectors associated to the velocity fields are presented, together with colour contours of vorticity fields, normalized using the overall maximum analytical and experimental values of velocity and vorticity, respectively. In general, very similar and symmetric flow patterns are found for both the theoretical predictions and the measurements, with the analytical or experimental cores of the vortices located, approximately, along the $\pi/4$ or $3\pi/4$ rays, respectively, in all cases, the theory predicting slightly larger radial distances from the post to the vortex core. Finally, it can be also observed that increasing values of α yield more intense circulations, as inferred from the vorticity contours, while the cores of the vortex, for $\alpha < \alpha_c$, and that of the internal vortex, for $\alpha > \alpha_c$, become closer to the post, as it was previously anticipated.

4.4.2 Effect of ε

The asymptotic description in powers of ε in the limit $\varepsilon \ll 1$ ceases to be valid for finite values of the stroke length, $\varepsilon \sim \mathcal{O}(1)$. To explore this effect, in the present section experimental results for $\varepsilon \sim \mathcal{O}(1)$ are shown for two values of α, namely $\alpha = 5 < \alpha_c$ and $\alpha = 9 > \alpha_c$, which are also compared with their counterparts for $\varepsilon = 0.2$ (considered here as $\varepsilon \ll 1$). Therefore, Figure 4.4 displays pathlines of time-averaged Lagrangian flow, left or second quadrant, and corresponding normalized velocity vectors, coloured with normalized vorticity contours, right or first quadrant, for $\alpha = 5$, first column, and for $\alpha = 9$, second column, for $\varepsilon = 0.2$, first row, and for $\varepsilon = 0.5$, second row. In both α cases, similar flow patterns are observed for $\varepsilon = 0.2$ and $\varepsilon = 0.5$. Thus, for $\alpha = 5$ one vortex is generated with clockwise rotation in the

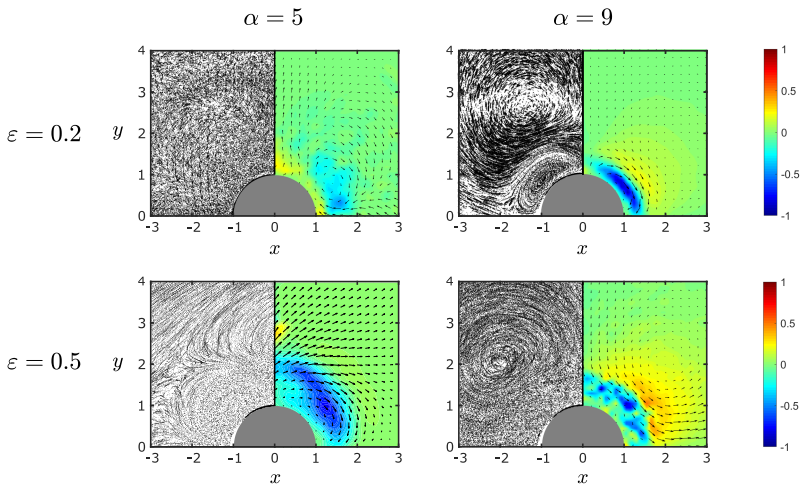

Figure 4.4: Steady flow patterns (left) and corresponding velocity and vorticity fields (right) of the flow around a cylindrical element at different values of α (subcritical flow on the left column and supercritical flow on the right column) and ε (theory approximation corresponds to the top row and order-unity values correspond to the bottom row).

first quadrant, whereas for $\alpha = 9$, a second external counter-rotating recirculating region appears, which encloses the internal vortex near the post. A close inspection of the results reveals that increasing stroke lengths might have an impact on the global flow topology and rotation intensity. In that regard, the size of the vortices is seen to be reduced when ε increases, for $\alpha = 9$, and the core of each vortex also becomes closer to the post wall. The latter is accompanied with more intense recirculations, as observed from the larger amplitudes of vorticity in the case of $\varepsilon = 0.5$ compared to those of $\varepsilon = 0.2$ in Figure 4.4. Interestingly, these results differ from what has been recently found in the case of a linear array of circular cylinders [38], where increasing values of the stroke length have been reported to yield less intense and larger recirculating vortices. Finally, the trend reported here has been observed to have also an impact on α_c, which seems to decrease for increasing values of ε.

4.4.3 Time-averaged Lagrangian motion in anharmonic oscillating flows: CSF flow

So far the analysis has been focused on the flow around a post with a harmonically sinusoidal stream of velocity $u_\infty(t^*) = U_\infty \cos \omega t^*$. However, in nature it is common to find oscillatory flows that present anharmonic temporal variations, such as that of the blood in veins and arteries, or that of the CSF in the CNS [19], [20]. Therefore, the study is experimentally extended to analyze the flow induced by an anharmonic oscillatory flow around a post in the present section. Specifically, a wave of temporal dependence equal to that of a CSF flow recently measured in a human spinal canal [21] has been considered. This velocity waveform can be expressed as a Fourier series $u_\infty(t^*) = \Sigma_{n=1}^{\infty} Re(A_n e^{i\omega_n t^*})$, where A_n are the associated coefficients [38], [119], [120]. Figure 4.5(a) shows the flow rate associated to a harmonic waveform while Figure 4.5(b) represents a period of the flow rate provided by a cardiac anharmonic waveform. In this figure the positive and negative flow rates are given during systole, of dimensionless duration t_1, and diastole, of dimensionless duration t_2, respectively with $\int_0^{2\pi} Q(t)dt = 0$ or, similarly, $|\int_0^{t_1} Q(t)dt| = |\int_{t_1}^{2\pi} Q(t)dt|$, where $t = 2\pi t^*/T$ represents the dimensionless time, and $T = 1/f = 2\pi/\omega$ is the period of the waveform.

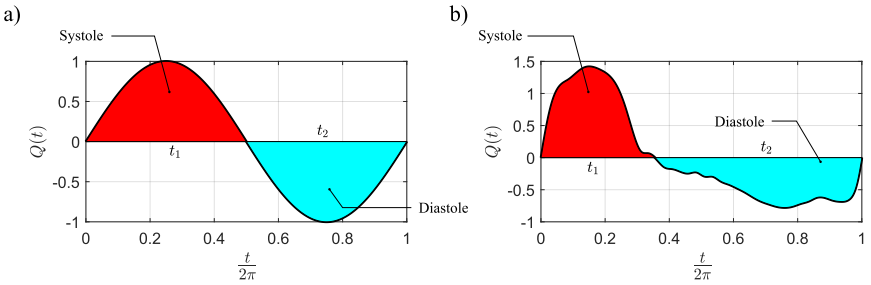

Figure 4.5: a) Harmonic flow waveform ($t_1 = t_2 = \pi$). b) Realistic flow waveform, obtained through MRI measurements and set as Fourier expansion ($t_1 \neq t_2$). Here, $t = 2\pi t^*/T$ represents the dimensionless time with $T = 1/f = 2\pi/\omega$ is the period of the waveform.

Differently from what happened in the harmonic case, where the time-averaged flow was symmetric in the four quadrants of the plane $z = 0$, the flow induced by an anharmonic wave results in a steady motion which is only symmetric with respect to the axis of the flow oscillation $y = 0$. Consequently, in the following the first two quadrants, $y \geq 0$, of the plane $z = 0$ will be shown in characterizing the flow. As in Section 4.4.1, Figure 4.6 shows pathlines of the time-averaged Lagrangian flow for the harmonic wave, top row, together with their counterparts for the anharmonic wave, bottom row, for different values of α, namely $\alpha = 6$, 8 and 10, and $\varepsilon = 0.2$. As previously shown, the harmonic wave induces steady flow patterns that are symmetric in each quadrant. However, this symmetry is broken in the anharmonic case, as a result of the inter-modes interaction [38], [120]. For the lowest value of α ($\alpha = 6$), the lack of fore-and-aft symmetry is hardly observable, where only marginally distorted vortices appear, with their cores near the post wall, as in the harmonic case. The loss of symmetry becomes more apparent for larger values of α, e.g. $\alpha = 8$, where, as for $\alpha = 6$, two vortices form close to the post, but which in this case are significantly distorted, being also their cores displaced downwards in the systolic direction (towards the the positive y-coordinate). In addition, the two vortices seem to be surrounded by a region of fundamentally streamwise velocity, which becomes more noticeable for even larger values of α. Finally, for $\alpha = 10$, a flow topology change takes place. In this case, the steady flow is characterized by the formation of an additional external vortex only in the first quadrant (downstream in the systolic direction). Moreover, the two vortices, already present for $\alpha < \alpha_c$, undergo larger distortions and are also displaced downwards in the systolic direction. Finally, the three vortices are surrounded by an almost horizontal external stream, which is in agreement with the results obtained for the infinite cylinder [112] or more recently in a linear array of circular cylinders [38].

The effect of considering finite stroke lengths is analyzed in Figure 4.7, where results for $\varepsilon = 0.5$ are compared with those previously shown for $\varepsilon = 0.2$, for $\alpha = 6$ and 8. As happened in the harmonic case, the size of the vortices formed is reduced when ε is increased, these being also more distorted and displaced downwards in the systolic direction in this case. Interestingly, as it was previously anticipated, increasing ε has also an impact on the flow topology change, reducing the value of α_c. The latter can be observed for both values of α, for which only two vortices are formed close to the post when $\varepsilon = 0.2$, one in each quadrant, whereas a third external vortex appears when $\varepsilon = 0.5$ in the first quadrant already at $\alpha = 6$.

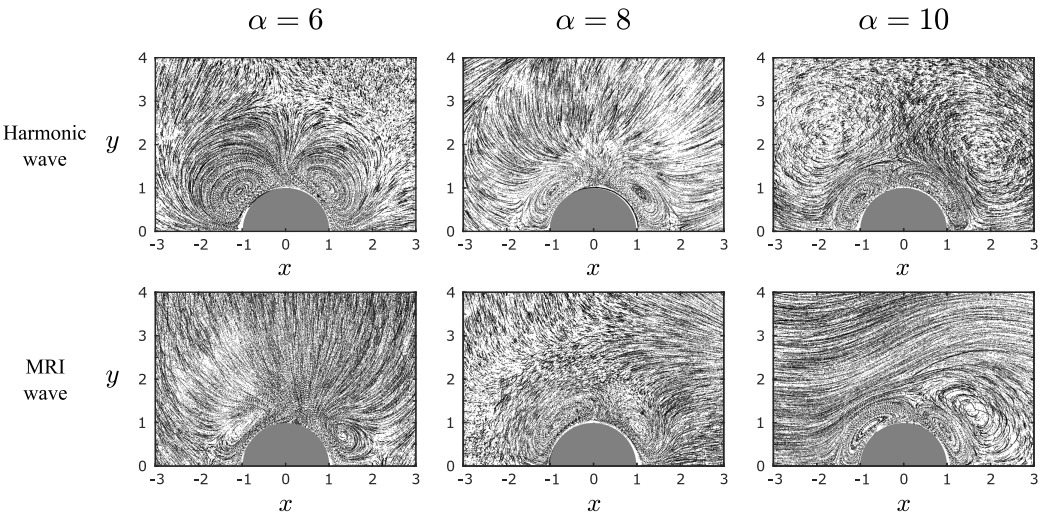

Figure 4.6: Steady pathlines of the flow around an obstacle confined between two parallel walls at different values of α and $\varepsilon = 0.2$. Top row corresponds to the tracking lines obtained with a harmonic waveform and bottom row corresponds to the tracking lines obtained through realistic flow motion.

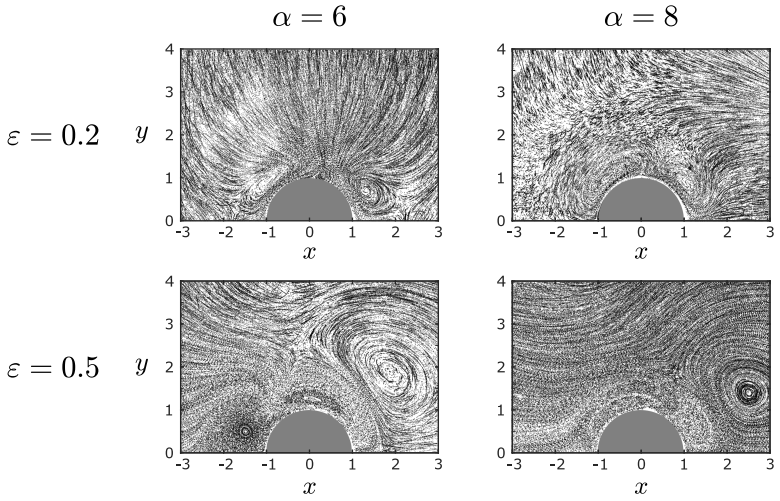

Figure 4.7: Steady fluid particles trajectories around a cylindrical post for different cases of α and ε, obtained with subject-specific CSF waveform.

4.4.4 Time-averaged motion around a linear array of posts

The human spinal canal is characterized by the presence of microanatomical elements along it, such as trabeculae, denticulate ligaments or nerve roots. In particular, nerve roots are present in most spinal segments and can be found in both sides of the canal arranged in bundles that emerge from the spinal cord and exit the vertebral column through the intervertebral discs. To further explore the effect of these elements on the steady flow that is induced in the case of an oscillatory flow around them, the present section reports preliminar experimental results of the time-averaged Lagrangian flow around an array of five circular posts, aligned with the oscillation axis, which are separated a semi-distance between the axes of contiguous posts d, thus, being the dimensionless semi-distance $\ell = d/a = 2$.

Figure 4.8 shows time-averaged pathlines in the horizontal symmetry plane $z = 0$ generated by a harmonic flow for different values of α, namely $\alpha = 5$, 6 and 9, and two values of ε, i.e. $\varepsilon = 0.2$ and 0.5, for $\ell = 2$. As it can be seen, the steady flow

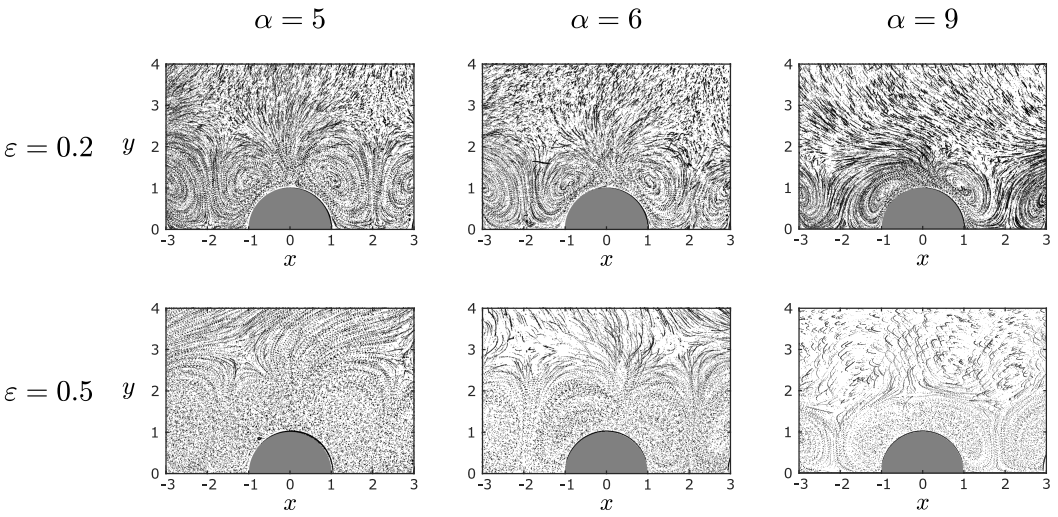

Figure 4.8: Steady flow patterns around a linear array of cylindrical posts separated by $\ell = 2$ at different values of α (columns) and ε (rows), induced by a harmonic waveform.

patterns induced for $\ell = 2$ are similar to those for $\ell = \infty$. Thus, considering the results for $\varepsilon = 0.2$, for $\alpha = 5$ and 6, two symmetric, counterclockwise vortices are formed, one in each quadrant, which display the same direction of rotation as for $\ell = \infty$. The presence of contiguous posts renders a confining effect, limiting the shape of each vortex to the semi-distance length in the axial direction. Consequently, deformed vortices are generated, whose cores are displaced towards the axis $x = 0$, in agreement with [38]. This effect is more apparent for the lowest value of $\alpha = 5$, since the vortices reduce in size and become closer to the posts when α increases. The presence of neighbouring posts seems somewhat to have also an impact on α_c, delaying the flow transition featuring the apparition of external counter rotating vortices in each quadrant to larger α. The latter is noticeable for $\alpha = 9$, where only two internal vortices are formed, one in each quadrant, whereas its counterpart for $\ell = \infty$ displays two vortices in each quadrant ($\alpha_c \simeq 8.5$ for $\ell = \infty$), see Figure 4.4. The bottom row of Figure 4.8 represents the results obtained for $\varepsilon = 0.5$. Similarly to what happened for $\ell = \infty$, increasing ε produces smaller and more intense recirculations, with vortices whose cores are closer to the posts. Furthermore, larger values of ε appear to advance the flow topology transition, as it was anticipated in previous sections. This can be observed in the case of $\alpha = 9$, for which a pair of inner and outer counter rotating vortices are formed in each quadrant when $\varepsilon = 0.5$, whereas only an inner vortex is seen when $\varepsilon = 0.2$. The linear array configuration is further explored in Figure 4.9, where time-averaged pathlines induced by an anharmonic fluid stream are shown for three values of $\alpha = 6$, 9 and 11, at $z = 0$ and for $\varepsilon = 0.2$. These kinds of waveforms have been found to cause the loss of flow symmetry in all quadrants, thus, this flow is only symmetric respect to the axis $y = 0$. As a consequence, for $\alpha < \alpha_c$, two different and asymmetric inner vortices form, with their cores unevenly displaced in the axial direction, which decrease in shape, become closer to the posts and increase in intensity when α increases. For $\alpha > \alpha_c$, a second external vortex appears in the first quadrant, similar to what happened for $\ell \to \infty$, but in the case of $\ell = 2$, the vortices being deformed and axially enclosed withing the semi-distance length. Moreover, in all cases the vortices are also surrounded by a region of streamwise velocity. To conclude, as it can be inferred from Figure 4.10, larger values of ε are found to produce the same effects as those reported in the case of a harmonic flow.

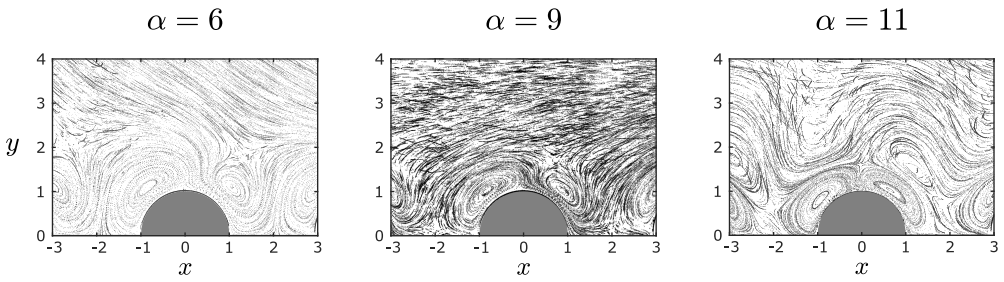

Figure 4.9: Steady pathlines of the flow around a cylinder at different values of α for $\varepsilon = 0.2$, induced by a patient-specific waveform.

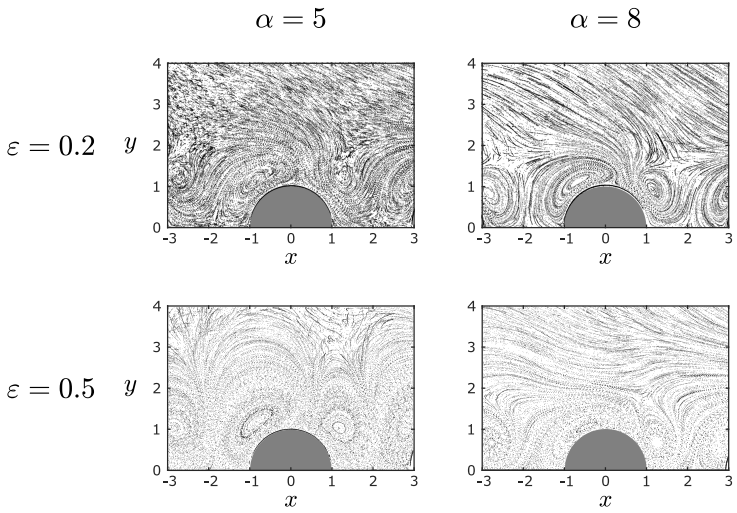

Figure 4.10: Particle pathlines of the steady flow around a cylindrical post for different values of α and ε, with a realistic CSF waveform.

4.5 Conclusions

In this chapter, the time-averaged flow topologies induced by oscillatory streams around circular posts has been considered. This analysis is focused on the effect of different parameters, such as the oscillatory flow frequency and the stroke length, as well as the waveform. Results obtained for a harmonic flow show time-averaged flow patterns that are identical in all quadrants, in each of which a recirculation cell forms near the post, for $\alpha < \alpha_c$, whose size reduces at larger values of α. The effect of α features a flow topology change when $\alpha > \alpha_c$, which is characterized by the formation of a second external vortex. The time-averaged flow induced by an anharmonic waveform is found to loss the symmetry respect to the transversal axis. In this case, different cell sizes form, in the subcritical flow range, and only an outer cell appears in the quadrant downstream in the systolic direction. Regardless the waveform, the flow topology transition has been found to also depend on the stroke length ε, and is seen to occur for lower values of α when ε increases. Finally, this analysis has been extended to consider a linear array of posts, representing a bundle of nerve roots along the spinal canal. Results show similar flow patterns for both geometrical configurations, i.e. a single post and an array of posts, when the stream is harmonic. However, significantly different flow topologies are found for anharmonic waveforms. These results aim at providing further understanding to the characterization of the influence of the microanatomy in the CSF flow, and sets the basis of future investigations, where not only the fluid flow but also the solute transport should be accounted for.

Part III

Characterization of the CSF flow in the cranial SAS

Chapter 5

In vitro characterization of the oscillatory flow in the cerebral aqueduct

This *in vitro* study aims at clarifying the relation between the oscillatory flow of the CSF in the cerebral aqueduct and the interventricular pressure difference over the range of flow conditions commonly encountered in healthy subjects. Dimensional analysis is used in designing a scaled model of the aqueduct flow, with physical similarity maintained by adjusting the flow frequency and the properties of the working fluid. The experiments include an aqueduct model with an anatomically correct shape determined from high-resolution magnetic resonance imaging (MRI). A programmable pump is employed to generate the flow-rate signal, including a sinusoidal waveform and a complex waveform previously measured *in vivo* using phase-contrast (PC) MRI. The time-varying pressure difference across the aqueduct is measured in parametric ranges covering relevant frequencies and stroke volumes. The experimental measurements are presented in dimensionless form to provide the relation between the waveforms of the flow rate and trans-aqueductal pressure difference. Parametric dependences are delineated for the time-averaged pressure fluctuations and for the phase lag between the pressure gradient and the flow rate, both having clinical relevance. The results are validated through comparisons with predictions obtained with a previously derived computational model. The parametric quantification in this study enables the derivation of a simple formula for the relation between the trans-aqueductal pressure and the stroke volume. This relationship can be useful in the quantification of transmantle pressure differences based on non-invasive PC MRI measurements of aqueduct flow for investigation of CSF-related disorders.

This Chapter is comprised in the paper: "An in vitro experimental investigation of oscillatory flow in the cerebral aqueduct", by S. Sincomb, F. Moral-Pulido, O. Campos, C. Martínez-Bazán, V. Haughton & A.L. Sánchez, submitted to the European Journal of Mechanics-B/Fluids.

5.1 Introduction

The CSF fills the cerebral ventricles and the SAS, which surrounds the brain and the spinal canal. As seen in previous chapters, its motion has been studied extensively, not only because of the key role in the transport of substances, but also due to its relevance in the development of pathological conditions related to abnormal CSF dynamics, such as NPH [60], [62]. In this aspect, the leading order motion (oscillatory), driven by cardiac and respiratory cycles [19], [20], [55]–[57], is more relevant in the

cranial cavity, being found the maximal CSF velocities in the cerebral aqueduct (a narrow passage connecting the third and fourth ventricles of $L \simeq 10$ mm and $a \simeq 1$ mm as length and radius, respectively), with clinical interest in developing NPH [61] and in understanding effects of different treatments [64], [65]. This effect can be related through the transmantle pressure (the instantaneous pressure difference between lateral ventricles and the CSAS), which can be approximated to the trans-aqueductal pressure difference $\Delta p_{aq}(t^*) = p_3 - p_4$, where the largest pressure drop occurs. The value of this pressure fluctuates from positive to negative about a negligibly small time-averaged value, with associated peak flow rates $Q_{aq}(t^*) \sim 0.1$ mL/s [70], [71]. Despite its low value, the transmantle pressure is considered to play a role in the ventricle enlargement characterizing NPH patients with altered CSF flow dynamics due to the cyclic strain field [74], which acts on the brain parenchyma and can explain the change of brain viscoelastic properties. The phase lag between $\Delta p_{aq}(t^*)$ and the flow rate $Q_{aq}(t^*)$ has also been investigated because of its potential clinical relevance in NPH patients [75], thereby underscoring the implications of the waveforms involved in aqueduct flow.

Measuring the transmantle pressure requires ultra-high-resolution pressure sensors to read simultaneously pressure values at the order of a few pascals, a difficult and risky surgery. Since the interventricular pressure difference $\Delta p_{aq}(t^*)$ can be computed from noninvasive MRI measurements of the aqueduct flow rate $Q_{aq}(t^*)$ [67], several efforts have been made to characterize it through this non-invasive procedure. In fact, different models [67], [72], [78] have established the corresponding relationship between both parameters. In addition to the different proposed models, *in vivo*, *in silico* and *in vitro* studies of the aqueduct flow have been performed, allowing the characterization of the flow in the aqueduct and inside the third ventricle, using realistic flow rates and simplified harmonic waveforms (e.g. the studies of Yamada et al. [55], Schibli et al. [84] and specially Holmlund et al. [87]). However, these results do not report the relative flow-rate/pressure-gradient phase lags, of clinical interest as described above.

The purpose of the present *in vitro* experiments is that of complementing these previous studies by providing a more complete parametric description of the interventricular pressure difference for a range of flow conditions found in healthy subjects. Experiments were conducted with an anatomically correct model, conveniently scaled up by a factor of 10, as needed to enable pressure measurements to be made, with care taken to maintain physical similarity. While most experiments considered a realistic time-dependent flow rate $Q_{aq}(t^*)$, to investigate influences of canal shape and flow-rate anharmonicity an initial set of measurements used instead a sinusoidal flow rate in an aqueduct model of constant circular section. The experimental results were validated through comparisons with predictions obtained using the previously published theoretical model [72]. The experimental measurements, presented in dimensionless form, provide a thorough description of the relation between the flow rate and the interventricular pressure difference. The new information can be useful in designing future protocols for quantification of transmantle pressure differences based on non-invasive phase contrast (PC) MRI measurements. Our experimental approach allows for future investigation of altered aqueduct CSF dynamics, such as that encountered in NPH patients.

In the following, an *in vitro* characterization of the interventricular pressure difference along the cerebral aqueduct is presented, complementing the aforementioned

previous studies. The rest of the chapter is organized as follows. The dimensional arguments employed in scaling the experiment are introduced in Section 5.2. The description of the facility and a detail account of the data acquisition procedures are given in Section 5.3. Experimental results are presented in Section 5.4. Finally, conclusions and future extensions of the work are discussed in Section 5.5.

5.2 Problem description

One could envision an experiment mimicking exactly the cerebral aqueduct conditions. Water would be used as working fluid, since its density $\rho = 1000$ kg/m^3 and kinematic viscosity $\nu = 0.71 \times 10^{-6}$ m^2/s differ from those of CSF by a negligibly small amount. The setup would involve a tiny canal whose shape and size would have to be identical to those of the human aqueduct (i.e. $L \simeq 10$ mm and $a \simeq 1$ mm), a micro-pump able to deliver oscillating flow rates with peak values on the order of 0.1 mL/s, and a sensor with the capability of measuring pressure differences of a few pascals with sufficient accuracy. Of course, such an experiment would be difficult due to microfabrication challenges and also because the devices that are required to deliver/measure accurately such small flow rates/pressure differences are uneconomical. The alternative procedure followed here involves scaling up the aqueduct model as well as the resulting flow rate and pressure difference, in such a way that the experiment can be performed in the lab using the available resources.

A phantom model of the aqueduct with a size scaling factor $\chi = 10$ was built to investigate experimentally the relation between the aqueduct flow rate and its associated inter-ventricular pressure drop. In scaling the model, account was taken of the physical similarity between the experimental conditions and those found in the human aqueduct, in order to guarantee that the experimental results represent the actual flow in the human aqueduct. To that end, all the dimensionless parameters must take the same values in the *in vitro* model and the human brain. In reducing the parametric dependence of the inter-ventricular pressure $\Delta p_{aq}(t^*)$, an initial attempt shows that the oscillatory flow depends on the canal shape, denoted by its length L and mean radius a, the density ρ and kinematic viscosity ν, the oscillatory motion frequency $\omega = 2\pi/T$, where T is the period of the fluid motion, and on the stroke volume $\Delta V = \frac{1}{2}\int_{t^*}^{t^*+2\pi/\omega} |Q_{aq}| \mathrm{d}t^*$ which is displaced back and forth along the canal and can be alternatively denoted with the stroke length $\Delta L = \Delta V/(\pi a^2)$.

Following the previous analysis developed in [72], the pressure difference $\Delta p_{aq}(t^*)$ is chosen to characterize by the mean value of its magnitude

$$\langle |\Delta p_{aq}| \rangle = \frac{\omega}{2\pi} \int_{t^*}^{t^*+2\pi/\omega} |\Delta p_{aq}| \mathrm{d}t^*, \tag{5.1}$$

so that we can write the mean pressure as the rest of parameters,

$$\langle |\Delta p_{aq}| \rangle = \langle |\Delta p_{aq}| \rangle (L, a, \rho, \nu, \Delta L, \omega). \tag{5.2}$$

Since the functional dependence features six parameters, three of which have independent dimensions, a straightforward application of the Buckingham Π theorem affords the reduction from six dimensional parameters to three dimensionless parameters, leading to

$$\langle |\Pi| \rangle = \frac{\langle |\Delta p_{aq}| \rangle}{\rho \omega^2 L \Delta L} = f\left(\frac{a}{L}, \frac{\Delta L}{L}, \alpha\right), \tag{5.3}$$

where $\alpha = \left(a^2\omega/\nu\right)^{1/2}$ is the Womersley number of the flow. The characteristic value used to scale Δp_{aq} follows from assuming that the local acceleration $\partial u/\partial t^* \sim \Delta L\omega^2$ is comparable to the pressure force per unit mass $\rho^{-1}\partial p/\partial x^*$, that being always the case for the flow conditions found in the cerebral aqueduct. While the aqueduct aspect ratio is very large, giving values of a/L in the range $1/20 \lesssim a/L \lesssim 1/10$, the dimensionless stroke length $\Delta L/L$ and the Womersley number α are of order unity, with typical values lying in the ranges $0.5 \lesssim \Delta L/L \lesssim 1.5$ and $2 \lesssim \alpha \lesssim 4$.

For illustrative purposes, the specific values corresponding to the 77 subjects considered in our previous study [79] are shown in Figure 5.1. The experiments reported below correspond to $\alpha = (2, 3, 4)$ (see Figure 5.1b) with $0.5 \lesssim \Delta L/L \lesssim 1.5$ (see Figure 5.1c), thereby covering the conditions most commonly found in healthy human subjects.

Regarding the design of the experiment, it is convenient to consider two flow con-

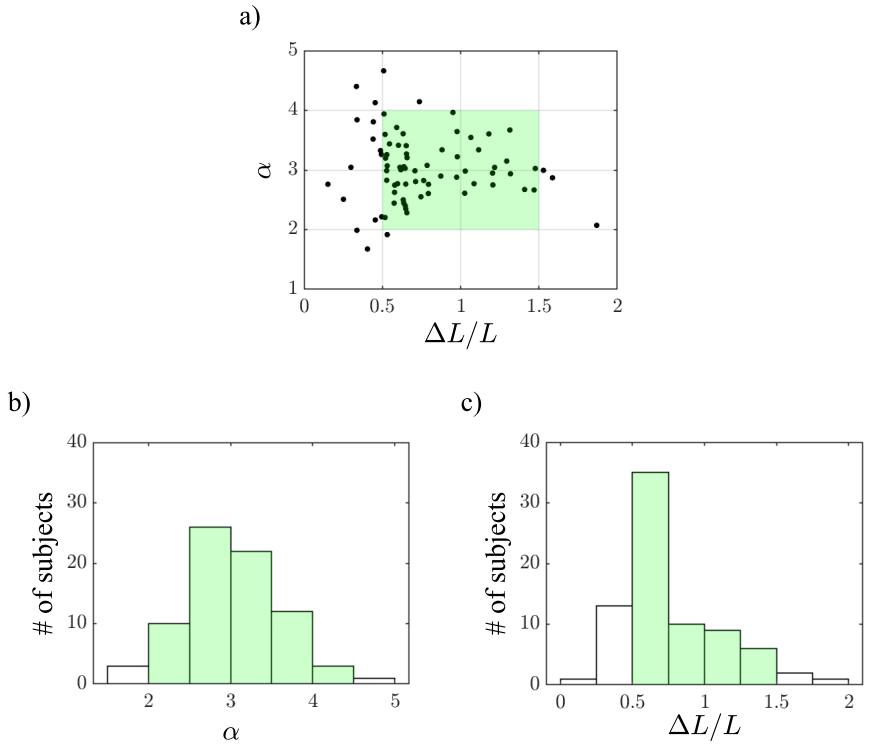

Figure 5.1: a) Scatter plot of values of the Womersley number (α) and stroke length-to-aqueduct length ratio ($\Delta L/L$) for 77 healthy volunteers participating in an IRB-approved study at HMRI, as reported elsewhere [79]. Distribution of these values for b) α and c) $\Delta L/L$.

figurations involving canals of different size that are geometrically similar, so that their aspect ratios a/L are identical. According to Equation (5.3), if the values of α and $\Delta L/L$ are equal in both configurations, then the resulting values of the dimensionless pressure-fluctuation amplitude $\langle|\Pi|\rangle = \langle|\Delta p_{aq}|\rangle/(\rho\omega^2 L\Delta L)$ would also be equal. Therefore, to guarantee physical similarity, the dimensions, frequency, stroke length, and kinematic viscosity of the experiment (denoted by the subscript E) must be related to those of the human aqueduct (denoted by the subscript H) by

$$\frac{a_E}{L_E} = \frac{a_H}{L_H}, \quad \frac{\omega_E a_E^2}{\nu_E} = \frac{\omega_H a_H^2}{\nu_H} \quad \text{and} \quad \frac{\Delta L_E}{L_E} = \frac{\Delta L_H}{L_H}. \tag{5.4}$$

When the above relations are satisfied, then the inter-ventricular pressure difference

$\langle|\Delta p_{aq}|\rangle_H$ can be computed in terms of the pressure difference $\langle|\Delta p_{aq}|\rangle_E$ measured between the containers (representing the third and fourth ventricles) with use made of

$$\frac{\langle|\Delta p_{aq}|\rangle_E}{\rho_E \omega_E^2 L_E \Delta L_E} = \frac{\langle|\Delta p_{aq}|\rangle_H}{\rho_H \omega_H^2 L_H \Delta L_H}. \tag{5.5}$$

The above expressions were used in scaling up the experiment by a factor $\chi = L_E/L_H = a_E/a_H = 10$. In particular, the working fluid was selected to give experimental pressure differences 100 Pa $\lesssim \Delta p_{aq} \lesssim$ 1500 Pa well within the operating range ±10 inH20 (±2490 Pa) of the available pressure sensor (see the pressure transducer features in Table 5.2). The need for a working fluid different from water is apparent when using Equation (5.4) to write Equation (5.5) in the form

$$\frac{\langle|\Delta p_{aq}|\rangle_E}{\langle|\Delta p_{aq}|\rangle_H} = \frac{\rho_E}{\rho_H}\left(\frac{\omega_E}{\omega_H}\right)^2 \frac{L_E}{L_H}\frac{\Delta L_E}{\Delta L_H} = \frac{\rho_E}{\rho_H}\left(\frac{\nu_E}{\nu_H}\right)^2 \chi^{-2}. \tag{5.6}$$

Clearly, in order for the pressure difference of the experiment with $\chi = 10$ to be larger than that of the cerebral aqueduct (i.e. $\langle|\Delta p_{aq}|\rangle_H \sim 5$ Pa), the working fluid in the experiment must be significantly more viscous than CSF, thereby motivating the use of mixtures of glycerol and water. To that end, three different glycerol-water mixtures were used to satisfy the physical similarity conditions. In order to set the composition of each mixture, let us consider a harmonic shape as the intra-ventricular pressure difference waveform Δp_{aq}, being the amplitude of this signal $\Delta p_{peak} = 2\langle|\Delta p_{aq}|\rangle$. The dimensionless value of this pressure can be obtained from Equation (5.3) as

$$\frac{\Delta p_{peak}}{\rho\omega^2 L^2} = 2\,(\Delta L/L)\,\langle|\Pi|\rangle(\alpha, a/L, \Delta L/L), \tag{5.7}$$

wherein the ranges of α, a/L and $\Delta L/L$ have been set previously. If a/L is fixed and $\langle|\Pi|\rangle$ is nearly independent on the parameter $\Delta L/L$ [72], $\langle|\Pi|\rangle$ can be obtained for each value of α, being

$$\langle|\Pi|\rangle = \begin{cases} 0.8, & \text{for} \quad \alpha = 2 \\ 0.6, & \text{for} \quad \alpha = 3 \\ 0.5, & \text{for} \quad \alpha = 4. \end{cases} \tag{5.8}$$

Once $\langle|\Pi|\rangle$ is set and knowing that Δp_{peak} must be between the range $100 \leq \Delta p_{peak} \leq 1500$ Pa to ensure reliable readings, the oscillatory frequency ω and kinematic viscosity can be obtained from Equation (5.7) as

$$\omega = \left[\frac{\Delta p_{peak}}{2\langle|\Pi|\rangle\rho L^2\,(\Delta L/L)}\right]^{1/2} \tag{5.9}$$

and

$$\nu = \frac{a^2}{\alpha^2}\left[\frac{\Delta p_{peak}}{2\langle|\Pi|\rangle\rho L^2\,(\Delta L/L)}\right]^{1/2}. \tag{5.10}$$

Finally, substituting the parameters of each expression and using $\rho = 1200$ kg/m^3, $L = 0.15$ m and $a = 0.01$ m as the fluid density, canal length and radius respectively, the corresponding kinematic viscosities and compositions of the mixtures (in terms of relative volume contents) yield $\nu_E = (10.5, 6.82, 3.83) \times 10^{-5}$ m^2/s and $(84/16, 80/20, 74/26)$, respectively. These mixtures have been set considering a constant room temperature $T_{room} = 21.5$ °C.

5.3 Experimental details and techniques

The experiments presented below were performed in an *in vitro* model of the interventricular space. The model consisted of two large reservoirs of cubic shape connected by the cerebral aqueduct model, as can be seen in the schematics of Figure 5.2(b) and 5.2(c). The reservoirs were constructed using acrylic sheets of width $w = 1/2''$ and assembled with acrylic cement. The periodic flow was generated with a programmable piston pump (SuperPump AR, ViVitro Labs, Victoria, Canada) connected through semi-rigid tubing to a ball valve located near the bottom of one of the reservoirs. The reservoir inner volume $\sim 8\ L$ was sufficiently large to minimize the pressure disturbances introduced by the associated intermittent jet stream. A latex balloon partially filled with air was included in the second reservoir to allow for compliance. It is important to note that, since the flow rate $Q_{aq}(t^*)$ was imposed by the peristaltic pump, the specific compliance of the balloon is unimportant for determining experimentally the spatial pressure difference between the two containers, which is only a function of the pulsating motion across the narrow aqueduct. For the same flow rate $Q_{aq}(t^*)$, it was verified experimentally that a balloon that was completely filled with air gave pressure fluctuations in both containers, i.e. $p_3(t^*)$ and $p_4(t^*)$, that were much larger than those in an experiment involving a partially filled balloon, but the corresponding instantaneous pressure difference between both containers $\Delta p_{aq} = p_3 - p_4$ remained unchanged.

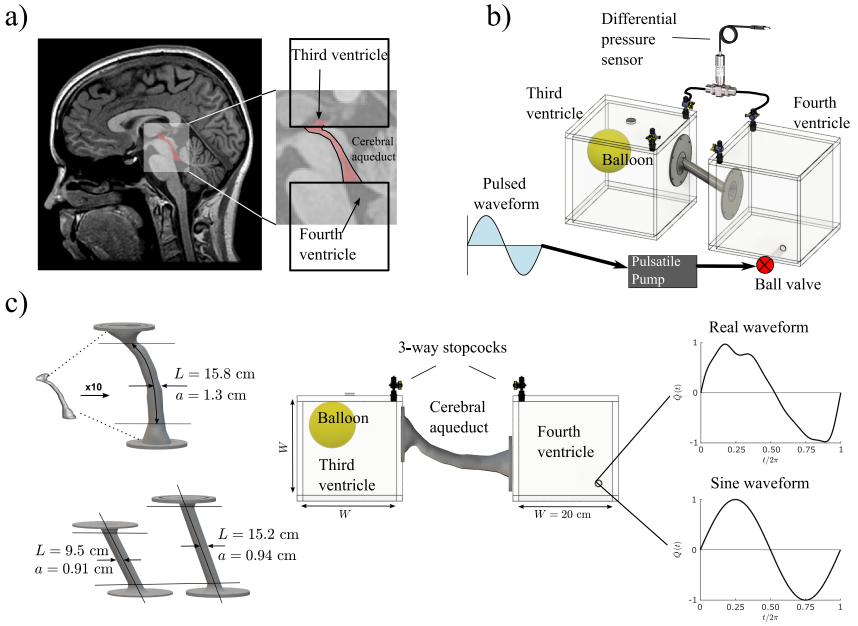

Figure 5.2: a) Geometry of the cerebral aqueduct, extracted from Magnetic Resonance Images (MRI) b) Schematic view of the complete *in vitro* model: both reservoirs, the latex balloon and the duct which represents the aqueduct (the presented model corresponds to the canonical geometry, provided at [72]. In addition, the differential pressure transducer is also represented. c) Scheme of the different geometries of the cerebral aqueduct with the corresponding dimensions (left), frontal view of the *in vitro* model (middle) and input flow rate waveforms, divided into the CSF real flow (right-up) and a harmonic waveform (right-down).

A first set of experiments employed the canonical aqueduct model shown in Figure 5.2(b) and in the bottom-left subplot of Figure 5.2(c), involving a circular cylinder of uniform radius whose edges were rounded to avoid flow separation during inflow. This simple configuration allowed to test the dependence of the results on

the aspect ratio a/L by using two tubes with different aspect ratios $a/L = 0.097$ and $a/L = 0.062$. A second set of experiments employed a realistic model of the cerebral aqueduct, shown in the top-left subplot of Figure 5.2(c), corresponding to the subject-specific anatomy used in Sincomb et al. [79] (associated IRB approved through Huntington Medical Research Institutes). In characterizing the subject's anatomy, high-resolution anatomic MRI images were used to segment the CSF contained in the aqueduct using ITK-SNAP (Version 3.6.0; www.itksnap.org) [121]; i.e. see Figure 5.2(a). The resulting segmentation model was then scaled by a factor of 10 ($\chi = 10$) and smoothed (Autodesk Meshmixer); i.e. see Figure 5.2(c). The segmentation represents the lumen of the cerebral aqueduct and was offset by 3 mm to create a hollow model with sufficient wall thickness to provide structural rigidity. After scaling up the model, the resulting inner mean radius and length were $a = 1.3$ cm and $L = 15.8$ cm, respectively, yielding an aspect ratio $a/L = 0.082$. The length of the real geometry was determined from the previous study, where the length is based on an increased of lumen size of 50% [79]. The scaled model printed for this study included some additional portion of the third and fourth ventricles seen in the red highlighted segmentation of the MRI image in Figure 5.2. A detailed view of the canal geometry with indication of the resulting canal length is included as an inset in Figure 5.5(a), to be discussed later.

For both geometries the connecting elements, representing the aqueduct, were 3D-printed on a Form 3 Stereolithography (SLA) resin desktop printer using a rigid clear resin (Formlabs). Printed parts were post-processed in accordance with the manufacturer instructions. The longer geometries were printed in two separate pieces due to the size limitation of the printer. Following post-processing, both pieces were joined using UV resin welding and epoxy resin after full cure. The models have flange attachments with a hand-made silicone o-ring which are secured to the reservoirs by screws and liquid PTFE (teflon) to avoid leakage.

As mentioned above, several mixtures of glycerol and water at different concentrations were used as a working fluid, in order to accommodate the pressure sensor measurements and the pump parameters under their corresponding limits. These mixtures are compounded mostly by glycerol (more than 75% in volume fraction), yielding densities and kinematic viscosities ranged between $\rho = 1202.2 - 1225.6 \mathrm{kg/m^3}$ and $\nu = 3.83 - 10.5 \times 10^{-5} \mathrm{m^2/s}$ respectively. The glycerol properties are sensitive to temperature changes, so that the room temperature was controlled with a constant value of $\mathrm{T_{room}} = 21.5^{\mathrm{o}}\mathrm{C}$. With these different mixtures and, therefore, values of density and viscosity, it was necessary to establish the periodic motion frequency with the desired values of the Womersley number, α. In addition, the large viscosity of the working fluid requires additional care when filling and purging the system, in order to avoid trapped air bubbles inside the mixture, which may induce errors in the measurements. To that end, the mixture was degassed with a vacuum chamber at first, and then the facility was filled with the use of a funnel.

The periodic volumetric flow rate $Q_{aq}(t^*)$ considered in the experiments included a simple sine wave $Q_{aq}(t^*) = \frac{1}{2}\Delta V \omega \sin(\omega t^*)$ and a physiologically correct waveform determined through PC-MRI measurements in a healthy 25-year-old female subject [79]. In generating the periodic signal, the pulsatile pump uses as input the prescribed piston position, a zero-averaged signal that must start and end at the same value. The harmonic waveform is supplied as one of the default options in the pump software. For the realistic waveform, the piston position was determined using a

trapezoidal cumulative numerical integration of the PC-MRI flow rate signal, and the result was scaled according to the manufacturer instructions to ensure the correct performance of the pump. The flow rate is adjustable within the limits of the pump, including frequencies in the range $3 - 200$ BPM and stroke volumes in the range $0 - 180$ mL/stroke.

A wet/wet differential bidirectional pressure transducer (OMEGA Engineering) connected to the reservoirs was used to take measurements of $\Delta p_{aq}(t^*)$ (device specifications can be found in Table 5.1). Since the cross-section of the reservoirs is much larger than the cross-section of the aqueduct, the velocities in the reservoirs are much smaller than those found in the aqueduct, so that the pressure in each container is nearly uniform. As a result, the value of Δp_{aq} is largely independent of the specific sensor-placement locations, provided that they are selected to be away from the entrance/exit regions. As indicated in Figure 5.2(b), in the conducted experiments the sensors were placed at the top of the reservoirs near the corners, where the fluid motion is negligible.

The system and pressure lines were checked to be bubble free. The pressure difference $\Delta p_{aq}(t^*)$ was measured with a sampling frequency of 80 Hz. To synchronize $\Delta p_{aq}(t^*)$ with $Q_{aq}(t^*)$ simultaneous recordings of instantaneous piston position were acquired using the pump's voltage output. An Arduino Mega micro-controller, with an internal 10 bit ADC, was used to convert the voltage output to a digital signal, which was transmitted via a serial connection to a portable computer, where an open source serial data logger was used to time-stamp and save the data. The voltage was converted to piston position according to the manufacturer's manual instructions. The sampling frequency of the analog output is 2500 Hz. The differences observed between the prescribed input piston position and the piston position computed from the pump's voltage output were smaller than 5%, in agreement with the manufacturer's stated waveform accuracy (i.e. $< 4\%$ of stroke volume at 70 BPM and $< 5\%$ of stroke volume at 200 BPM).

Name	**Description**
Transducer Material	316L Stainless Steel
Process fitting	1/4-18 NPT Female
Pressure type	Diff. Wet/Wet Bidirectional
Range unit	in-H2O (4°C)
in-H2O	10
Pressure transducer output	USB (high-speed)
Pressure transducer accuracy	±0.08% B.S.L.
Electrical termination	Cable (2m, 6ft)
Temperature range	18 to 85°C (-0 to 185°F)
Thermal accuracy: Zero shift / Span shift	±0.80% / ±0.60%

Table 5.1: Differential pressure transducer configuration

An experiment using a given glycerol-water mixture started by setting the corresponding amplitude-normalized waveform. Frequency values were selected in the range $0.15 \text{ Hz} \leq \omega/(2\pi) \leq 1.17$ Hz to provide the desired value of $\alpha = (a_E^2 \omega_E / \nu_E)^{1/2}$, with results shown below for $\alpha = (2, 3, 4)$. Once the pump is running at constant frequency, pressure measurements were taken in subsequent tests for increasing values

of the stroke volume $\Delta V = \pi a^2 \Delta L$, an input variable that could be adjusted manually to cover the range $0.5 \leq \Delta L/L \leq 1.5$ in increments of $\Delta(\Delta L/L) = 0.1$. Each test comprised a total of 40-50 cycles. A complete list of measurements obtained is given in Table 5.2.

No.Exp.	Geom.	$\nu \cdot 10^5$ (m^2/s)	Mixt.	f (BPM)	α	$\Delta L/L$
1	**CS**	**10.5**	**84/16**	**48**	**2**	**0.5-1.5**
2	CS	6.82	80/20	31	2	0.5-1.5
3	**CS**	**6.82**	**80/20**	**71**	**3**	**0.5-1.5**
4	CS	6.82	80/20	126	4	0.5-1.8
5	CS	3.83	74/26	18	2	0.5-1.5
6	CS	3.83	74/26	40	3	0.5-1.5
7	**CS**	**3.83**	**74/26**	**71**	**4**	**0.5-1.5**
8	**CL**	**10.5**	**84/16**	**45**	**2**	**0.5-1.5**
9	CL	6.82	80/20	29	2	0.5-1.4
10	**CL**	**6.82**	**80/20**	**66**	**3**	**0.5-1.5**
11	CL	3.83	74/26	17	2	0.5-1.5
12	CL	3.83	74/26	37	3	0.5-1.5
13	**CL**	**3.83**	**74/26**	**66**	**4**	**0.5-1.5**
14	**RE**	**10.5**	**84/16**	**24**	**2**	**0.5-1.3**
15	RE	10.5	84/16	53	3	0.8-1.1
16	RE	6.82	80/20	15	2	0.8-1.1
17	**RE**	**6.82**	**80/20**	**35**	**3**	**0.5-1.3**
18	RE	6.82	80/20	62	4	0.5-1.1
19	RE	3.83	74/26	9	2	0.5-1.3
20	RE	3.83	74/26	19	3	0.5-1.3
21	**RE**	**3.83**	**74/26**	**35**	**4**	**0.5-1.3**

Table 5.2: List of experiments conducted for each geometry ('CS' for *canonical short*, 'CL' for *canonical long* and 'RE' for *real geometry*) and viscosity value with corresponding frequency $\omega/2\pi$ (expressed in beats per minute, BPM) and sampled range of dimensionless stroke length $\Delta L/L$ (increments of $\Delta(\Delta L/L) = 0.1$). The α value determined for each mixture and where measurements were made 3 separate times is given in bold.

All signal processing was performed using a custom routine in MATLAB®. Signals were aligned using the timestamps of each recording. The pressure signal was filtered to eliminate noise and then zero-averaged. Pressure measurements from the sine wave flow rate were low-pass filtered at five times the selected frequency ω_E, while the results corresponding to the subject-specific waveform were low-pass filtered at eight times ω_E, as needed to retain sufficient high-frequency content. The piston-position signal, needed to synchronize the flow rate with the pressure difference, is resampled to the same frequency as the pressure signal (80 Hz). This signal reading would produce some cases with sudden spikes much larger than the average peak value (> 100 x) which were detected using a Hampel filter and smoothed. The piston-position signal was differentiated to obtain the flow rate that was then low-pass filtered. The results, appropriately nondimensionalized according to $\Pi(t) = \Delta p_{aq} / \left(\rho_E \omega_E^2 L_E \Delta L_E\right)$ and $\bar{Q}(t) = Q_{aq} / \left(\omega_E \pi a_E^2 \Delta L_E\right)$, where $t = \omega_E t^*$, were compared with predictions obtained using a previously published flow model [72]. Time-averaged magnitudes of the pressure difference $\langle|\Pi|\rangle = \int_0^{2\pi} |\Pi| \mathrm{d}t/(2\pi)$ were calculated using the trapezoidal rule.

The definition of the phase lag between $\Pi(t)$ and $\bar{Q}(t)$ is not unique. One could for example define the phase lag based on the relative position of the maxima or minima of the two signals within a given cycle, but with this definition the resulting values were found to be very sensitive to changes in the waveforms. A more robust approach, employed here, involves the use of the spectral domain. Thus, Fast Fourier Transform (FFT) was used to determine the fundamental mode and its corresponding phase for each variable, i.e.

$$\mathcal{F}[(\bar{Q}(t))](\omega_0) = |\bar{Q}(\omega_0)|e^{i\varphi_Q}$$
$$\mathcal{F}[(\Pi(t))](\omega_0) = |\Pi(\omega_0)|e^{i\varphi_\Pi},$$

with the phase lag determined from the difference between both phases $\varphi = \varphi_\Pi - \varphi_Q$. For definiteness, φ is defined in the range $-\pi \leq \varphi \leq \pi$, so that a positive value indicates that the pressure difference peaks before the flow rate.

5.4 Results

Pressure readings were obtained for the geometries and flow-rate signals indicated in Table 5.2. Resulting dimensionless pressure waveforms $\Pi(t) = \Delta p_{aq}/\left(\rho\omega^2\Delta L L\right)$ corresponding to sinusoidal and physiologically correct flow rates are shown in the bottom panels of Figure 5.3 for the canonical geometry, with corresponding model predictions shown in the accompanying top panels. As shown in Figure 5.3(a), for the sinusoidal flow rate, given by $\bar{Q}(t) = \frac{1}{2}\sin(t)$ in dimensionless form, the associated differential pressure is found to be nearly sinusoidal. By way of contrast, the physiologically correct flow rate, considered in Figure 5.3(b), induces a markedly anharmonic transmantle pressure $\Pi(t)$ exhibiting three peaks that are reminiscent of the percussion, tidal-wave, and dicrotic-wave peaks characterizing the intracranial pressure waveform [122]. For the particular case depicted in Figure 5.3(b), corresponding to $\alpha = 2$ and $\Delta L/L = 1$, the resulting time-averaged fluctuation amplitudes $\langle|\Pi|\rangle$ differ by approximately 14% and the corresponding phase lags φ exhibit differences of 12% from the model.

Extending the results of an initial case towards the full range of both parameters, Figure 5.4 represents the dimensionless time-averaged pressure fluctuations $\langle|\Pi|\rangle$ and accompanying phase lags φ determined experimentally for the cylindrical configuration. Following the dimensional analysis presented earlier, the results are plotted for values of the reduced stroke length in the range $0.5 \leq \Delta L/L \leq 1.5$ and two different values of the Womersley number $\alpha = 2$ (blue symbols) and $\alpha = 4$ (red symbols). Results acquired for $\alpha = 3$ are not included in the plot to avoid excessive cluttering. The plot includes measurements corresponding to three different glycerol-water mixtures, using two circular cylinders of different aspect ratio to represent the aqueduct, with results identified by either hollow markers ($a/L = 0.096$) or filled markers ($a/L = 0.062$). Theoretical predictions obtained with the mathematical model derived in Sincomb et al. [72] are represented by solid lines.

Except for an "outlier" set of experiments corresponding to the short geometry with $\nu = 6.82 \times 10^{-5}$ m^2/s (hollow triangles), the accordance of the different experimental results and the theoretical predictions is very satisfactory, especially with

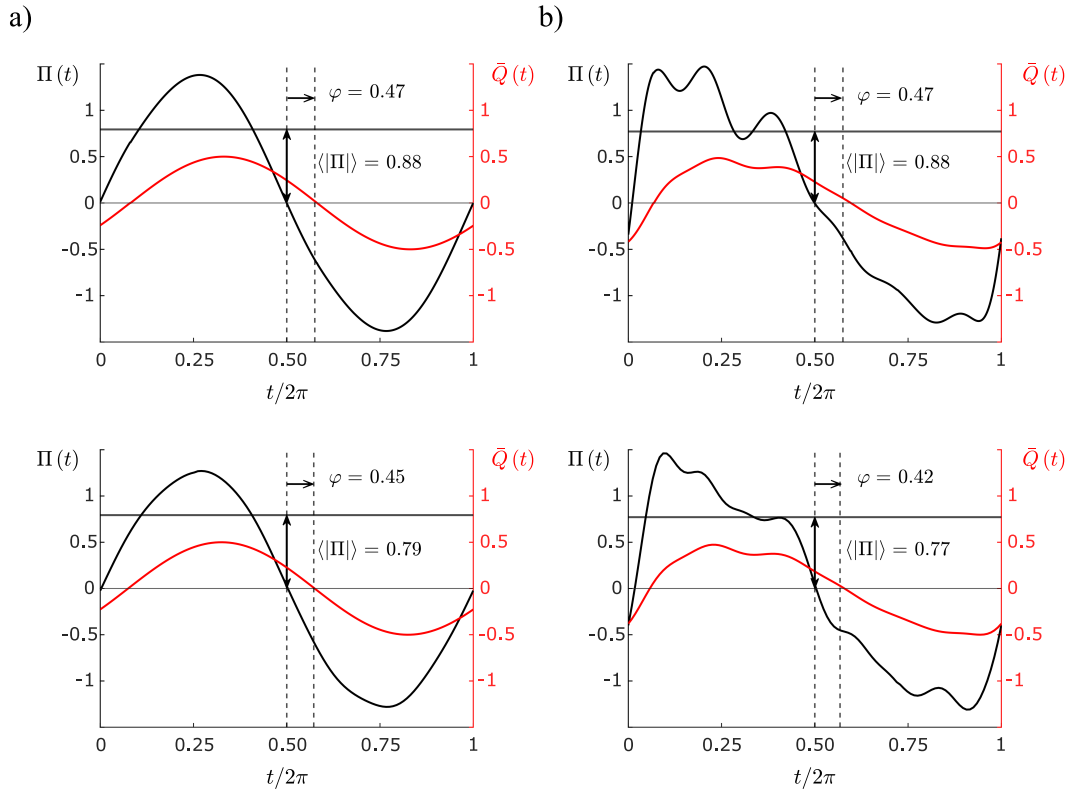

Figure 5.3: Dimensionless interventricular pressure $\Pi(t)$ corresponding to $\alpha = 2$ and $\Delta L/L = 1$ as determined from the previously published mathematical model [72] (top) and from the experimental measurements (bottom) for the cylindrical aqueduct ($a/L = 0.062$) with sinusoidal flow rate $\bar{Q} = \frac{1}{2}\sin t$ (a) and with the PC-MRI flow rate (b). Each plot includes an indication of the associated time-averaged pressure difference $\langle|\Pi|\rangle$ and phase lag φ.

regards to the results for $\alpha = 4$, thereby providing additional confidence on the selected parametric characterization of the flow. The analysis reveals that both $\langle|\Pi|\rangle$ and φ depend weakly on the dimensionless stroke length, variations remaining below about 10% over the entire range $0.5 \leq \Delta L/L \leq 1.5$ explored in the figure. By way of contrast, the dependence of the results on α is much more pronounced. As can be seen, as the Womersley number increases from $\alpha = 2$ to $\alpha = 4$, the pressure drop decreases by about 40%, that being a consequence of reduced effect of shear stresses, whereas the phase lag nearly doubles. The increase of φ with increasing α can be explained by noting that the phase lag between the intraventricular pressure and the flow rate is mainly a result of the interplay of the different forces entering in the momentum equation. In flows at low Womersley numbers, the viscous term becomes at the same order at the local acceleration and the pressure forces, so that the associated flow rate $Q_{aq}(t^*)$ is in phase with $\Delta p_{aq}(t^*)$. In contrast, in the opposite limit $\alpha \gg 1$, viscous forces can be neglected from the momentum equation. Thus, the flow rate and the intraventricular pressure can be expected to be in quadrature, as follows from a balance between local acceleration and pressure gradient. The results in Figure 5.4(b) are therefore consistent with the expected transition from $\varphi = 0$ ($\alpha \ll 1$) to $\varphi = \pi/2$ ($\alpha \gg 1$).

Measurements taken using the anatomically correct model are presented in Figure 5.5 for both harmonic (Figure 5.5a) and physiologically correct (Figure 5.5b) flow rate waveforms $Q_{aq}(t^*)$. For this geometry, the large pressure variations associated

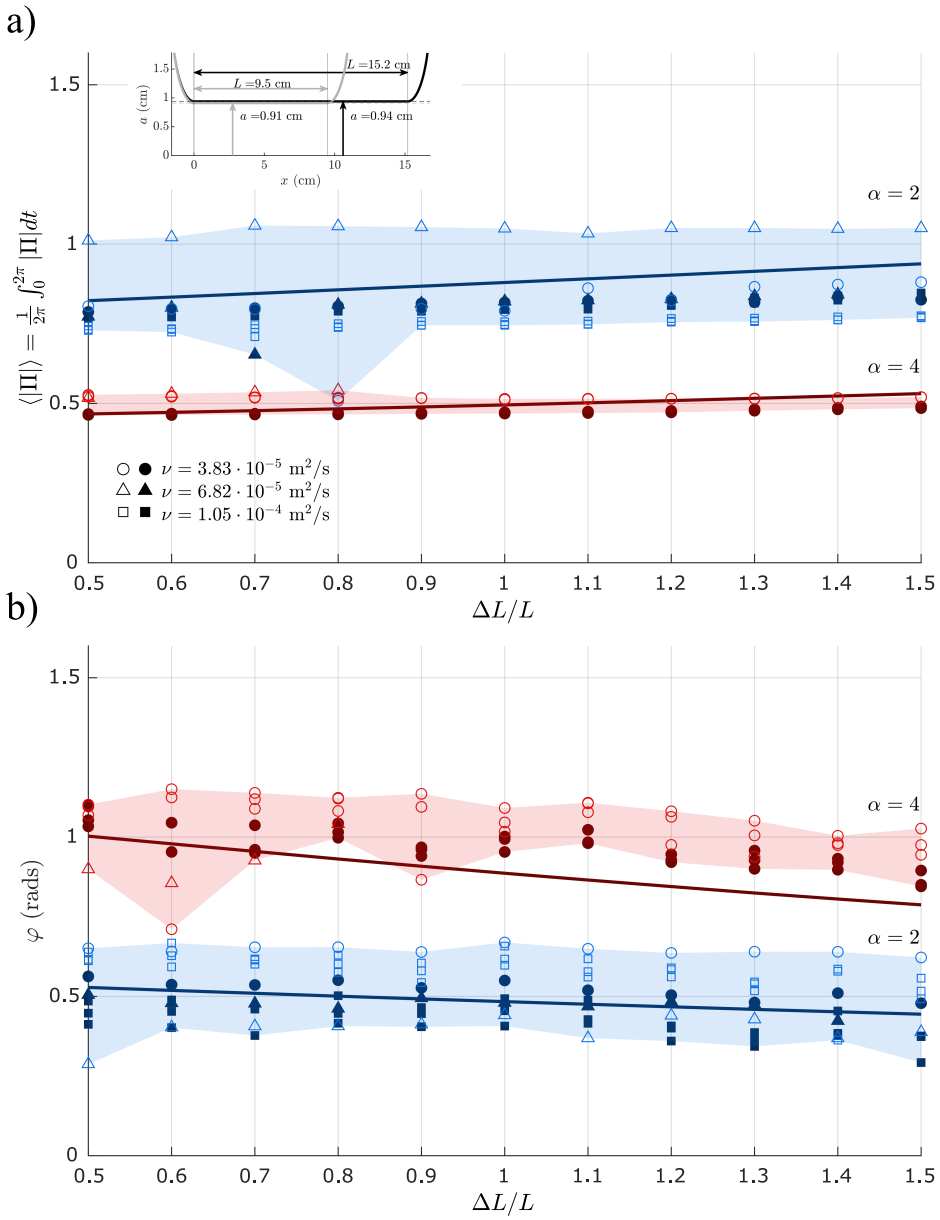

Figure 5.4: The variation with $\Delta L/L$ of the time-averaged magnitude of the pressure difference $\langle|\Pi|\rangle$ and phase lag φ for $\alpha = 2$ (blue) and 4 (red) as measured with three different glycerol-water mixtures (viscosity values are indicated in the labels) in experiments using a harmonic flow rate along with a circular cylinder as a canonical representation of the aqueduct (hollow symbols: $a/L = 0.096$, solid symbols: $a/L = 0.062$).

with the experiments at large stroke volumes were found to compromise the structural integrity of the reservoirs, so that the experiments were restricted to values of $\Delta L/L \leq 1.3$. As in Figure 5.4, very good agreement is obtained when the results of different working fluids are plotted in dimensionless form using α to characterize viscous effects.

Effects of canal anatomy on the pressure drop can be assessed by comparing the results in the top panels of Figures. 5.4 and 5.5(a), both corresponding to a sinusoidal flow rate. As can be seen, the dimensionless intraventricular pressure measured in the anatomically correct experiments is noticeably larger than that of the circular

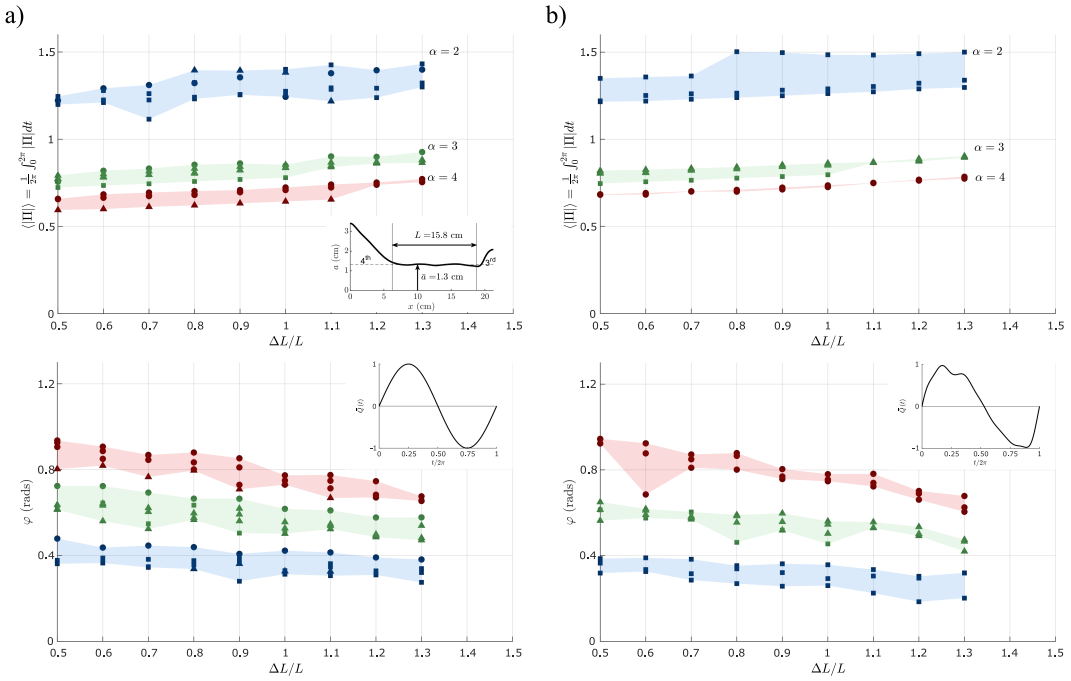

Figure 5.5: The variation with $\Delta L/L$ of the time-averaged magnitude of the pressure difference $\langle|\Pi|\rangle$ and phase lag φ for $\alpha = (2, 3, 4)$ as measured with three different glycerol-water mixtures (see labels in Figure 5.4) in experiments using an anatomically correct aqueduct shape (top left inset) together with a) a harmonic flow rate and b) an MRI-measured flow rate.

cylinders, a result attributable to the additional pressure loss occurring in the nozzle-like entrance regions of the third and fourth ventricles, which are included in the realistic model, as indicated in the inset of Figure 5.5(a). In principle, the presence of these regions could be accounted for in defining the canal length, leading to larger values of L and correspondingly smaller values of $\langle|\Pi|\rangle$, as follows from its definition in Equation (5.3), thereby possibly improving agreement between the canonical and anatomically correct results.

The comparison between the top panels in Figures 5.5(a) and 5.5(b) reveals that, while the waveform of the interventricular pressure is drastically different for the harmonic and physiologically correct flow rates, as seen in Figure 5.3, the differences in the mean pressure fluctuation $\langle|\Pi|\rangle$ remain smaller than 5% for all values of α and $\Delta L/L$. The differences in the phase lag are also very small, as seen in the lower plots, indicating that, for many quantitative purposes the flow rate can be represented by a simple sinusoidal function, as done in earlier analyses [67].

Of particular interest for quantitative purposes are the results shown in Figure 5.5(b), correspondingly to an anatomically correct aqueduct geometry and a physiologically correct flow rate. The lower plot shows the phase difference φ between $\Delta p_{aq}(t^*)$ and $Q_{aq}(t^*)$. As expected, the resulting value, weakly dependent on $\Delta L/L$, is found to increase as flow acceleration becomes more pronounced with increasing α. On the other hand, the value of $\langle|\Pi|\rangle$ shown in the upper plot of Figure 5.5(b), can be used in Equation (5.3) to provide

$$\frac{\omega}{2\pi}\int_{t^*}^{t^*+2\pi/\omega}|\Delta p_{aq}|\mathrm{d}t^* = \langle|\Pi|\rangle\rho\omega^2 L\frac{\Delta V}{\pi a^2}, \tag{5.11}$$

which can be useful in computing the mean value of the transmantle pressure fluctuation from MRI measurements of the stroke volume ΔV and the cerebral-aqueduct anatomy, the latter entering through the values of L and a.

The above expression (5.11) is useful in discussing the clinical relevance of the stroke volume, a metric previously proposed as a predictor for shunt response in patients with normal pressure hydrocephalus [60]. Compared with normal subjects, NPH patients are known to have larger stroke volumes [123], which, according to Equation (5.11), would be indicative of augmented interventricular pressure fluctuations, a reasoning that implicitly assumes that the aqueduct radius remains constant. However, enlargement of the aqueduct leads to a drastic reduction in the trans-aqueductal pressure, both because of the direct proportionality $\langle|\Delta p_{aq}|\rangle \propto a^{-2}$ present in Equation (5.11) and also because $\langle|\Pi|\rangle$ decreases with increasing $\alpha = a\sqrt{\omega/\nu}$, as shown in Figure 5.5(b). As a result, patients with simultaneous increased stroke volume and enlarged aqueduct cross-section may exhibit normal values of Δp_{aq}, as revealed in *in vivo* studies [69]. Clearly, future investigations addressing this issue can benefit from the simple quantitative description provided in Equation (5.11).

5.5 Conclusions

Experiments employing a scaled physical model of the cerebral aqueduct have been used to characterize the relation between the flow rate $Q_{aq}(t^*)$ and the interventricular pressure difference $\Delta p_{aq}(t^*)$. The focus has been on the time-averaged magnitude of the interventricular pressure difference $\langle|\Delta p_{aq}|\rangle$ and on the phase difference φ between $\Delta p_{aq}(t^*)$ and $Q_{aq}(t^*)$, both quantities potentially having clinical interest in connection with NPH [74], [75]. Dimensional analysis was used to simplify the parametric dependence, leading to the reduced functional dependence identified in Equation (5.11). A first set of experiments using two circular cylinders showed that the flow is fairly independent of the aspect ratio a/L, in agreement with previous theoretical results [74]. The dependences on the other two parameters (i.e. $\Delta L/L$ and α) are summarized in Figures 5.4 and 5.5, with the results in the former figure validated through comparisons with theoretical predictions. The agreement between the experimental measurements and the theoretical predictions is quite satisfactory in all cases.

The experimental setup provides an *in vitro* characterization of the relation between aqueductal flow and interventricular pressure using an anatomically correct aqueduct geometry and a physiologically correct flow rate, which complements previous experimental efforts [84]–[87]. The development exploits the fact that Δp_{aq} can be determined by investigating the flow through the aqueduct, without specific knowledge of the brain compliance, which is, however, essential for determining the temporal intracranial pressure fluctuations [124]. Mean interventricular pressure fluctuations have been characterized over parametric ranges describing the flow in the human aqueduct, leading to the derivation of a simple formula, given in Equation (5.11), for the mean trans-aqueductal pressure difference. Since in most cases the largest spatial pressure drop occurs across the aqueduct, Equation (5.11) can be applied in general to quantify the mean transmantle pressure from non-invasive MRI-measurements of the stroke volume. In using the equation, one should keep in mind that the transmantle pressure may differ significantly from the trans-aqueductal pressure in pathologic cases involving exceedingly enlarged aqueducts, stenosed foramina of Monro or other obstructions in the ventricular flow path; for these cases, Equation (5.11) would give

an inaccurate representation of the transmantle pressure. Besides quantification of the mean trans-aqueductal pressure, attention has been given to the determination of the phase lag between the $\Delta p_{aq}(t^*)$ and the flow rate $Q_{aq}(t^*)$, a metric with potential clinical application [75]. The phase lag has been found to depend mainly on the flow frequency and aqueduct radius (i.e. through $\alpha = a\sqrt{\omega/\nu}$), while the dependence on the stroke volume is much weaker.

Future investigations could benefit from improvements to the experimental apparatus. For instance, because of the volumetric size and available compliance of the experimental setup, the experiments reported above were limited on the range of stroke volumes and frequencies applied to the system, with additional limitations arising from the available pressure transducer. A lower frequency and/or lower stroke volumes incurred a larger noise contribution in the measurements. This was partially remedied through the use of different glycerol-water viscosity values and our attempt to balance the stroke volume and frequency. Additional sources of error include the presence of air bubbles within the main setup. We believe that a non-visible small air bubble likely within the pressure transducer and/or pump may be the cause for the outlier data points in the upper plot of Figure 5.4. The characterization of the phase lag on the basis of the fundamental frequency was found to be more robust than measurements based on cross-correlation or peak-to-peak time difference, which is partly due to the occurrence of signal jitter. However, this method relies on the availability of a large number of samples for high-frequency resolution, so that a decreased sampling frequency is needed for smaller time-sample sets. Future experiments should be recorded for longer duration to reduce this error. Additional systematic errors induced by the time-stamp alignment, which is on average about 1 ms ($< 5\%$ error), can be minimized by sampling over many cycles and performing repeated experiments, as done in the present study. The novel setup allows for investigation of various input parameters (signal waveform, fluid viscosity, aqueduct geometry) allowing us to measure the corresponding effects on the interventricular pressure. Future studies should consider the systematic variation of these parameters to understand certain diseases. Specifically, this experimental setup could be used to investigate the connection between changes in the frequency composition of the flow-rate signal, reported for example in [125], and the associated transmantle pressure. Also of interest are investigations of the relevance of the phase lag φ as a potential new marker of interest [75] as well as studies addressing diseases that result in altered CSF flow in the aqueduct such as NPH.

Chapter 6

Conclusions

6.1 General conclusions

The work presented in this Thesis focuses on characterizing the CSF flow in the SAS. To that aim, a theoretical study and *in vitro* experiments have been performed to characterize the velocity profile of the CSF flow and its corresponding transport phenomena in accordance with the biological ranges of the governing parameters, with attention given to the dispersion rate of a solute injected at the low thoracic and lumbar regions, a key process in connection with ITDD procedures, as well as with the diagnose potential disorders, such as NPH. In particular, the present investigation has been conducted in a simplified geometry employed in previous works [29], [39], [47], wherein additional steps have been included to reach a simple close-to-real model. In the following, the main conclusions and ideas developed and described through the previous chapters are summarised.

The first part of the dissertation, which considers the simplified geometry of the spinal canal modelled in previous works, starts with Chapter 2, where the CSF velocity profile and its solute transport are evaluated in accordance with the governing parameters of the problem, being the geometry of the SSAS, the pulsatility of the CSF motion, the pressure wave which induces CSF pulsatile motion and the elasticity of the canal. Here, considering a straight canal with constant cross section and constant eccentricity, a characteristic steady CSF flow topology has been observed with a net flux of CSF moving cranial along the narrowest region of the canal and caudal along the widest region of the canal, for low values of α. This flow configuration changes towards a reverse topology with larger values of the Womersley number, α, being the upward motion along the widest region of the canal and the downward motion along its narrowest region. This induces changes in the required time for a certain solute concentration to reach the cranial vault: whereas the flow rate changes as α increases, such required time increases until it reaches a maximum, decreasing abruptly for higher values of α. Moreover, the eccentricity of the canal modulates the transition of the flow topology, as well as the amplitude of the CSF flow rate: more eccentric channels delay the transition of the steady flow patterns, but also reduce the required time for the solute to reach the entrance of the canal, obtaining a relationship between this time, $\tau_c|_{max}$, and the relative eccentricity, β, of order $\tau_c|_{max} \sim \beta^2$. In addition to this extensive analysis, a step forward has been performed thanks to the use of a new geometry, where the eccentricity changes along its axis, being this new geometry closer to the actual geometry of the SSAS. Results on this geometry show the formation of recirculating cells in the canal, which increases the dispersion of solute within each cell but hinders its transport towards the brain. This flow topology also changes with α, wherein the solute is able to surpass the circulating cells for larger values of this parameter. The analytical predictions have

been corroborated with *in vitro* experiments in Chapter 3, using a facility similar to the analytical model. Experimental results validate the analytical model, showing an excellent agreement in terms of the solute advance for different eccentricities at lower values of α. Furthermore, the experimental model also shows the variations in the flow topology for different values of the Womersley number, as well as the recirculating cells for the variable eccentricity geometry. These experiments have been conducted, for the first time, with an induced motion thanks to the flexibility of the inner wall of the canal, emulating the pulsatile motion of the CSF, induced by the intracranial pressure fluctuations, considering the fluid-structure interaction problem.

In addition to the effect of the geometry and the Womersley number, the study has been extended to analyse the effects of the pressure wave propagation inside the canal and the elastic properties of the walls. In this regard, low values of the dimensionless wave number k are related to wave lengths larger than the length of the canal. This effect shows that the fluid particles oscillate with the same phase, presenting a varicose motion of the walls, which induces the flow patterns described before. However, when k increases up to order unity, the trend changes: the maximum in the velocity profile is displaced towards the middle of the canal and a big recirculating cell appears. Similar to the canonical geometry, increasing the value of k also induces an increase in the modulus of the velocity field up to $k \sim 1$ for the curved geometry; for larger values, the presence of new recirculating cells and the reduction of the flow rate is induced because the pressure wave is not able to penetrate inside the canal. Finally, the effect of the elastic properties of the canal show differences if the compliance function γ is constant or azimuthal-dependent, presenting different times to reach the solute the cranial vault. The results of this study are important in guiding future developments of predictive tools to assist clinicians and to evaluate the effectiveness of ITDD processes.

The results in Part I of this dissertation are obtained considering a constant eccentric, canonical canal at first, and a more realistic one later. However, in the previous analysis the effect of the microanatomy has not been considered. To that end, the second part of this Thesis has focused on evaluating this effect in terms of the steady fluid motion. This analysis has been performed through *in vitro* experiments, where a simple model with one unique element has been evaluated at first, and secondly with a linear array of elements, evaluating the parametric dependence of the induced steady flow patterns, being the Womersley number, the relative stroke parameter, ε, and the shape of the waveform. Results show, for an harmonic flow rate waveform, the formation of symmetric vortex patterns, whose size is reduced with α up to a critical value: values above α_c show the formation of a second outer cell. The value of α_c is dependent of several parameters, being one of them ε: from the limit of $\varepsilon \ll 1$, an increase of ε leads to not only higher values of the vorticity field, but also an advance in the formation on these outer cells. The resulting steady flow patterns change within the shape of waveform: whereas double symmetry patterns are induced with a harmonic waveform, actual CSF flow induce asymmetries in the transversal axis, being the 'negative' cell bigger than the positive. Moreover, supercritical flow patterns show only one exterior vortex in the positive semi-plane instead of the exterior vortex on each quadrant: in the negative semi-plane, net flow towards the negative side is generated.

Apart from the aforementioned results obtained for one post, the analysis has been extended to consider a linear array of elements, which may correspond to the

flow around the nerve roots along the spinal canal. Similar to the case of one post, the formation of recirculating cells and the transition to supercritical flow patterns are also observed. However, the shape of the recirculating cells differs from that obtained for the post: the presence of contiguous elements narrow the cells and deform their shape. Moreover, the value of α_c also differs with the presence of the neighbour posts: the distance between elements delays the transition to supercritical steady flow patterns. These results show the influence of the microanatomy of the CSF flow and, therefore, its solute transport, along the spinal canal. The induced steady flow patterns may produce changes in the flow inside the canal, being the solute able to move faster among the recirculating cells seen in Chapter 2 and Chapter 3 and also alter the arrival times of the solute to reach the cranial vault.

The work presented in Parts I and II aimed to characterize the CSF flow and its corresponding solute transport along the SSAS. In contrast to this objective, a different goal has been addressed in Part III: Chapter 5 has provided initial steps at characterizing the transmantle pressure and its relationship with the corresponding flow rate along the cerebral aqueduct in accordance with the governing parameters, i.e. the Womersley number, the dimensionless stroke length $\Delta L/L$ and the aspect ratio a/L. This characterization has been performed through an initial *in vitro* model of the cerebral aqueduct of previous works [72] at first, and a second healthy patient-specific geometry of the cerebral aqueduct. Moreover, this analysis has set two different waves: a harmonic waveform and a realistic waveform, obtained through MRI measurements. Experiments show that, while the effect of the aspect ratio is completely irrelevant, a slight dependence of the stroke length is observed: the absolute-time-averaged value of the transmantle pressure increases and the phase lag between the transmantle pressure and the flow rate decreases within $\Delta L/L$. Although the dependence of the stroke length has been reported, this influence is weak compared to the effect of α, which is the strong parameter in this analysis. In fact, an increase of α reduces the absolute-time-averaged value of the transmantle pressure and increases its phase lag with the flow rate. These results have been compared with the analytical model developed previously, obtaining good agreement in terms of pressure and phase lag. In addition to the parametric dependence, the real geometry and using a realistic flow rate waveform also present the same trends as seen for the canonical results, concluding that a subject-specific geometry of the cerebral aqueduct and its corresponding flow rate can be modelled as a slender tube with a characteristic radius and a sinusoidal flow rate. This study sets the preliminary steps in evaluating the transmantle pressure in the cerebral aqueduct: determining the pressure variation through dimensionless formulation is a powerful technique which can be solved easier and faster than others, i.e. direct numerical simulations (DNS). In addition, as seen in literature, a few *in vitro* models have provided the pressure in a facility similar to that presented in this chapter; however, this is the first time that the phase lag of the pressure is obtained through *in vitro* experiments with the corresponding model agreement despite its potential clinical application [75]. Thus, this study will be useful to develop a potential tool for future diagnoses through non-invasive techniques, avoiding the referring clinical risks of the eventual invasive procedures.

6.2 Future work

During the development of this Thesis, several additional questions have arisen. Addressing these questions will provide with a more comprehensive understanding of the problem and might be the subject of future works. To that end, this section aims at introducing such questions.

First of all, this dissertation seeks to characterize the CSF motion along the spinal canal through different ways. As is introduced in Chapter 2 and extended along the first part of this Thesis, this problem is addressed as a fluid-structure interaction (FSI) problem, wherein the pulsating intracranial pressure fluctuations displace a small fraction of the total CSF volume in and out of the SSAS, thanks to the compliance of the fatty tissue and blood vessels of the dura mater. In fact, the model predictions presented in Chapter 2 shows how the propagation of the pressure wave induces changes in the steady flow behaviour on the one hand, generating recirculating cells at large values of the dimensionless wavenumber k. On the other hand, the canal compliance presents changes in the transport phenomena when it depends on the azimuthal component, i.e. a delay in the transition of the reversal flow configuration and reductions in the arrival times of the solute into the CSAS. Despite the relevance of the model predictions, *in vitro* work to validate these effects has not been carried out in this dissertation. Therefore, further experiments with changes in the elastic properties of the canal will be useful to study the influence of these parameters.

As aforementioned described, the contemplated experiments and model predictions presented in Chapters 2 and 3 show the effects of the governing parameters of the flow in the solute dispersion of the CSF in the spinal canal. These results have been obtained with isobaric conditions between CSF and the drug (equal densities). However, this condition is not clinical: as far as is seen in literature, most of the drugs used in ITDD procedures are considered hyperbaric (more dense than CSF) or hypobaric (less dense than CSF), so that effects of buoyancy are clinically interesting to study. According to previous analytical works of the research group in which the effect of the buoyancy is study in the long-time scale [126] and the lack of *in vitro* work in this field, interest will be focus on characterizing this effect through *in vitro* measurements, which will corroborate the analytical work and will set one step further in the investigation presented in this dissertation.

Apart from the exhaustive work, previously presented in Part I, Part II has focused on evaluating the influence of the microanatomy in the spinal canal (i.e. nerve roots, trabeculae, etc). These elements induce the formation of steady CSF flow structures, which may change the flow rate, as seen in previous works of the research group [21]. In spite of the clinical potential of this effect, no *in vitro* work has been addressed yet. Thus, further efforts will be made in including the linear arrays of posts inside the model of the spinal canal described in Part I, which emulate the nerve roots that emerge from the spinal cord and get across the spinal subarachnoid space. This study will allow to evaluate differences between the clean model and a close-to-real spinal canal in terms of solute dispersion, which will have an impact on the optimization of ITDD procedures.

Finally, thanks to the research stay of the author of this dissertation at University of California San Diego, Part III of this Thesis has addressed the characterization of

the transmantle pressure in the cerebral aqueduct, in accordance with governing parameters previously reported [79]. The *in vitro* results are useful to diagnose relating diseases, such as NPH. These experiments have been obtained by the use of an *in vitro* model, similar to the analytical model previously presented [72], as well as a subject-specific geometry of a healthy patient, which validates the theory. As mentioned above, this work corresponds to the first steps of a further investigation, wherein accurate non-invasive diagnoses of malformations and diseases would be possible. Thus, future works would include more realistic geometries, provided from healthy to NPH diagnosed patients, which will allow to obtain the critical parameters that determine these diseases through noninvasive techniques, reducing drastically the clinical risks.

Bibliography

[1] L. Sakka, G. Coll, and J. Chazal, "Anatomy and physiology of cerebrospinal fluid," *Eur. Ann. Otorhinolaryngol. Head Neck Dis.*, vol. 128, pp. 309–316, 2011. DOI: https://doi.org/10.1016/j.anorl.2011.03.002.

[2] D. A. Seehusen, M. M. Reeves, and D. A. Fomin, "Cerebrospinal fluid analysis," *Am. Fam. Physician*, vol. 68, no. 6, pp. 1103–1109, 2003.

[3] K. Ambarki, T. Lindqvist, A. Wåhlin, *et al.*, "Evaluation of automatic measurement of the intracranial volume based on quantitative MR imaging," *Am. J. Neuroradiol.*, vol. 33, no. 10, pp. 1951–1956, 2012. DOI: https://doi.org/10.3174/ajnr.A3067.

[4] D. Orešković and M. Klarica, "The formation of cerebrospinal fluid: Nearly a hundred years of interpretations and misinterpretations," *Brain Res. Rev.*, vol. 64, no. 2, pp. 241–262, 2010. DOI: https://doi.org/10.1016/j.brainresrev.2010.04.006.

[5] L. Sass, M. Khani, J. Romm, *et al.*, "Non-invasive MRI quantification of cerebrospinal fluid dynamics in amyotrophic lateral sclerosis patients," *Fluids Barriers CNS*, vol. 17, no. 4, p. 14, 2020. DOI: https://doi.org/10.1186/s12987-019-0164-3.

[6] L. N. Telano and S. Baker, *Physiology, Cerebral Spinal Fluid*. United States: National Library of Medicine, 2022.

[7] M. Bottros and P. Chisto, "The function and structure of the cerebrospinal fluid outflow system," *Cerebrospinal Fluid Res.*, vol. 7, no. 1, p. 9, 2010. DOI: https://doi.org/10.1186/1743-8454-7-9.

[8] R. Spector, S. Snodgrass, and C. Johanson, "A balanced view of the cerebrospinal fluid composition and functions: Focus on adult humans," *Exp. Neurol.*, vol. 273, pp. 57–68, 2015. DOI: https://doi.org/10.1016/j.expneurol.2015.07.027.

[9] D. Greitz, A. Franck, and B. Nordell, "On the pulsatile nature of intracranial and spinal CSF-circulation demonstrated by MR imaging," *Acta Radiol.*, vol. 34, no. 4, pp. 321–328, 1993. DOI: https://doi.org/10.1080/02841859309173251.

[10] D. Greitz and J. Hannerz, "A proposed model of cerebrospinal fluid circulation: Observations with radionuclide cisternography.," *Am. J. Neuroradiol.*, vol. 17, no. 3, pp. 431–438, 1996.

[11] H. Davson, "The blood-brain barrier," *J. Physiol.*, vol. 255, no. 1, pp. 1–28, 1976.

[12] A. K. Ommaya, M. A. Oxon, and M. B. Punjab, "Subcutaneous reservoir and pump for sterile access to ventricular cerebrospinal fluid," *Lancet*, vol. 282, pp. 983–984, 1963. DOI: https://doi.org/10.1016/S0140-6736(63)90681-0.

[13] M. Bottros and P. Chisto, "Current perspectives on intrathecal drug delivery," *J. Pain Res.*, vol. 7, pp. 615–626, 2014. DOI: http://dx.doi.org/10.2147/JPR.S37591.

[14] S. V. Watve, M. Sivan, W. A. Raza, and F. F. Jamil, "Management of acute overdose or withdrawal state in intrathecal baclofen therapy," *Spinal Cord*, vol. 50, pp. 107–111, 2012. DOI: https://doi.org/10.1038/sc.2011.112.

[15] J. Whedon and D. Glassey, "Cerebrospinal fluid stasis and its clinical significance," *Alternat. Ther. Health Med.*, vol. 15, no. 3, pp. 54–60, 2009.

[16] S. Bothwell, D. Janigro, and A. Patabendige, "Cerebrospinal fluid dynamics and intracranial pressure elevation in neurological diseases," *Fluids Barriers CNS*, vol. 16, no. 9, 2019. DOI: https://doi.org/10.1186/s12987-019-0129-6.

[17] H. L. Rekate, "A contemporary definition and classification of hydrocephalus," *Semin. Pediatr. Neurol.*, vol. 16, no. 1, pp. 9–15, 2009. DOI: https://doi.org/10.1016/j.spen.2009.01.002.

[18] B. Langridge, E. Phillips, and D. Choi, "Chiari malformation type 1: A systematic review of natural history and conservative management," *World Neurosurg.*, vol. 104, pp. 213–219, 2017. DOI: https://doi.org/10.1016/j.wneu.2017.04.082.

[19] D. Kelley and J. Thomas, "Cerebrospinal fluid flow," *Annu. Rev. Fluid Mech.*, vol. 55, pp. 237–264, 2023. DOI: https://doi.org/10.1146/annurev-fluid-120720-011638.

[20] A. Linninger, K. Tangen, C. Hsu, and D. Frim, "Cerebrospinal fluid mechanics and its coupling to cerebrovascular dynamics," *Annu. Rev. Fluid Mech.*, vol. 48, no. 1, pp. 219–257, 2016. DOI: https://doi.org/10.1146/annurev-fluid-122414-034321.

[21] S. Sincomb, W. Coenen, C. Gutiérrez-Montes, C. Martínez-Bazán, V. Haughton, and A. L. Sánchez, "A one-dimensional model for the pulsating flow of cerebrospinal fluid in the spinal canal," *J. Fluid Mech.*, vol. 939, A26, 2022. DOI: https://doi.org/10.1017/jfm.2022.215.

[22] W. Coenen, C. Gutiérrez-Montes, S. Sincomb, *et al.*, "Subject-specific studies of csf bulk flow patterns in the spinal canal: Implications for the dispersion of solute particles in intrathecal drug delivery," *Am. J. Neuroradiol.*, vol. 40(7), 1242–1249, 2019. DOI: https://doi.org/10.3174/ajnr.A6097.

[23] S. Dreha-Kulaczewski, M. Konopka, A. A. Joseph, *et al.*, "Respiration and the watershed of spinal CSF flow in humans," *Sci. Rep.*, vol. 8, no. 1, p. 5594, 2018. DOI: https://doi.org/10.1038/s41598-018-23908-z.

[24] G. Aktas, J. M. Kollmeier, A. A. Joseph, *et al.*, "Spinal CSF flow in response to forced thoracic and abdominal respiration," *Fluids Barriers CNS*, vol. 16, no. 10, p. 8, 2019. DOI: https://doi.org/10.1186/s12987-019-0130-0.

[25] C. Gutiérrez-Montes, W. Coenen, M. Vidorreta, *et al.*, "Effect of normal breathing on the movement of csf in the spinal subarachnoid space," *American Journal of Neuroradiology*, vol. 43, no. 9, pp. 1369–1374, 2022. DOI: https://doi.org/10.3174/ajnr.A7603.

[26] F. Moral-Pulido, J. I. Jiménez-González, C. Gutiérrez-Montes, W. Coenen, A. L. Sánchez, and C. Martínez-Bazán, "In vitro characterization of solute transport in the spinal canal," *Phys. of Fluids*, vol. 35, no. 5, 2023.

[27] H. S. Smith, T. R. Deer, P. Staats, V. Singh, N. Sehgal, and H. Cordner, "Intrathecal drug delivery," *Pain Physician*, vol. 11, S89–S104, 2008.

[28] G. Di Chiro, "Movement of the cerebrospinal fluid in human beings," *Nature*, vol. 204, pp. 290–291, 1964. DOI: https://doi.org/10.1038/204290a0.

[29] A. L. Sánchez, C. Martínez-Bazán, C. Gutiérrez-Montes, *et al.*, "On the bulk motion of the cerebrospinal fluid in the spinal canal," *J. Fluid Mech.*, vol. 841, pp. 203–227, 2018.

[30] K. Kundu and U. K. Sarkar, "Analytical and numerical investigation of Poiseuille flow through semi-elliptic annulus," *Phys. Fluids*, vol. 34, no. 8, 2022. DOI: https://doi.org/10.1063/5.0101058.

[31] S. Gupta, M. Soellinger, P. Boesiger, D. Poulikakos, and V. Kurtcuoglu, "Three-dimensional computational modeling of subject-specific cerebrospinal fluid flow in the subarachnoid space," *J. Biomech. Eng.*, vol. 131, no. 2, p. 021 010, 2009. DOI: doi:10.1115/1.3005171.

[32] K. Tangen, Y. Hsu, D. Zhu, and A. Linninger, "CNS wide simulation of flow resistance and drug transport due to spinal microanatomy," *J. Biomech.*, vol. 48, no. 10, pp. 2144–2154, 2015, ISSN: 0021-9290. DOI: https://doi.org/10.1016/j.jbiomech.2015.02.018. [Online]. Available: https://www.sciencedirect.com/science/article/pii/S0021929015000974.

[33] H. Stockman, "Effect of anatomical fine structure on the flow of cerebrospinal fluid in the spinal subarachnoid space," *J. Biomech. Eng.*, vol. 128, no. 1, 106–114, 2006. DOI: https://doi.org/10.1115/1.2132372.

[34] H. Stockman, "Effect of anatomical fine structure on the dispersion of solutes in the spinal subarachnoid space," *J. Biomech. Eng.*, vol. 129, no. 5, 666–675, 2007. DOI: https://doi.org/10.1115/1.2768112.

[35] M. Khani, L. Sass, T. Xing, M. Sharp, O. Balédent, and B. Martin, "Anthropomorphic model of intrathecal cerebrospinal fluid dynamics within the spinal subarachnoid space: Spinal cord nerve roots increase steady-streaming," *J. Biomech. Eng.*, vol. 140, no. 8, pp. 0 810 121–08 101 215, 2018. DOI: https://doi.org/10.1115/1.4040401.

[36] S. Cheng, D. Fletcher, S. Hemley, M. Stoodley, and L. Bilston, "Effects of fluid structure interaction in a three dimensional model of the spinal subarachnoid space," *J. Biomech.*, vol. 47, no. 11, pp. 2826–2830, 2014. DOI: https://doi.org/10.1016/j.biomech.2014.04.027.

[37] S. Linge, V. Haughton, A. LØvgren, K. Mardal, and H. Langtangen, "CSF flow dynamics at the craniovertebral junction studied with an idealized model of the subarachnoid space and computational flow analysis," *AJNR Am. J. Neuroradiol.*, vol. 31, no. 1, pp. 185–192, 2010. DOI: https://doi.org/10.3174/ajnr.A1766.

[38] J. Alaminos-Quesada, J. J. Lawrence, W. Coenen, and A. L. Sánchez, "Oscillating viscous flow past a streamwise linear array of circular cylinders," *J. Fluid Mech.*, vol. 959, no. A39, 2023.

[39] J. J. Lawrence, W. Coenen, A. L. Sánchez, *et al.*, "On the dispersion of a drug delivered intrathecally in the spinal canal," *J. Fluid Mech.*, vol. 861, pp. 679–720, 2019. DOI: https://doi.org/10.1017/jfm.2018.937.

[40] G. Stokes, "On the theory of oscillating waves," *Trans. Camb. Phil. Soc.*, vol. 8, 441–455, 1847.

[41] G. D. Cramer and S. A. Darby, *Clinical Anatomy of the Spine, Spinal Cord, and Ans*. United States: Mosby, 2014.

[42] D. M. Perriman, J. M. Scarvell, A. R. Hughes, B. Ashman, C. J. Lueck, and P. N. Smith, "Validation of the flexible electrogoniometer for measuring thoracic kyphosis," *Spine*, vol. 35, no. 14, pp. 633–640, 2010. DOI: https://doi.org/10.1097/BRS.0b013e3181d13039.

[43] L. Sass, M. Khani, G. Natividad, R. Tubbs, O. Baledent, and B. Martin, "A 3D subject-specific model of the spinal subarachnoid space with anatomically realistic ventral and dorsal spinal cord nerve rootlets," *Fluids Barriers CNS*, vol. 14, no. 36, 2017. DOI: https://doi.org/10.1186/s12987-017-0085-y.

[44] Y. Ishida, K. Suzuki, and K. Ohmori, "Dynamics of the spinal cord: An analysis of functional myelography by CT scan," *Neuroradiology*, vol. 30, no. 6, pp. 538–544, 1988. DOI: https://doi.org/10.1007/BF00339697.

[45] H. Inoue, K. Ohmori, T. Takatsu, T. Teramoto, Y. Ishida, and K. Suzuki, "Morphological analysis of the cervical spinal canal, dural tube and spinal cord in normal individuals using CT myelography," *Neuroradiology*, vol. 38, no. 2, pp. 148–151, 1996. DOI: https://doi.org/10.1007/BF00604802.

[46] R. Lee, A. van Zundert, P. Breedveld, J. Wondergem, D. Peek, and P. Wieringa, "The anatomy of the thoracic spinal canal investigated with magnetic resonance imaging (MRI)," *Acta Anaesth Belg*, vol. 58, 163–167, 2007. DOI: http://dx.doi.org/10.1097/AAP.0b013e3181e8a344.

[47] C. Gutiérrez-Montes, W. Coenen, J. J. Lawrence, C. Martínez-Bazán, A. L. Sánchez, and J. C. Lasheras, "Modelling and direct numerical simulation of flow and solute dispersion in the spinal subarachnoid space," *Appl. Math. Model.*, vol. 94, pp. 516–553, 2021. DOI: https://doi.org/10.1016/j.apm.2021.01.037.

[48] H. Hettiarachchi, Y. Hsu, T. Harris Jr., and A. Linninger, "The effect of pulsatile flow on intrathecal drug delivery in the spinal canal," *Ann. Biomed. Eng.*, vol. 39, no. 10, pp. 2592–2602, 2001. DOI: https://doi.org/10.1007/s10439-011-0346-x.

[49] M. Khani, L. R. Sass, M. K. Sharp, *et al.*, "In vitro and numerical simulation of blood removal from cerebrospinal fluid: Comparison of lumbar drain to neurapheresis therapy," *Fluid Barriers CNS*, vol. 17, pp. 1–17, 2020. DOI: https://doi.org/10.1186/s12987-020-00185-5.

[50] M. Khani, G. Burla, L. Sass, *et al.*, "Human in silico trials for parametric computational fluid dynamics investigation of cerebrospinal fluid drug delivery: Impact of injection location, injection protocol, and physiology," *Fluids Barriers CNS*, vol. 19, no. 8, 2022. DOI: https://doi.org/10.1186/s12987-022-00304-4.

[51] A. Benninghaus, O. Balédent, A. Lokossou, C. Castelar, S. Leonhardt, and K. Radermacher, "Enhanced in vitro model of the CSF dynamics," *Fluids Barriers CNS*, vol. 16, no. 11, 2019. DOI: https://doi.org/10.1186/s12987-019-0131-z.

[52] G. Williams, S. Thyagaraj, A. Fu, *et al.*, "In vitro evaluation of cerebrospinal fluid velocity measurement in type I Chiari malformation: Repeatability, reproducibility, and agreement using 2D phase contrast and 4D flow MRI," *Fluids Barriers CNS*, vol. 18, no. 12, 2021. DOI: https://doi.org/10.1186/s12987-021-00246-3.

[53] A Brodbelt and M Stoodley, "Csf pathways: A review," *Br. J. Neurosurg.*, vol. 21, no. 5, pp. 510–520, 2007.

[54] T. Brinker, E. Stopa, J. Morrison, and P. Klinge, "A new look at cerebrospinal fluid circulation," *Fluids Barriers CNS*, vol. 11, no. 1, pp. 1–16, 2014.

[55] S. Yamada, M. Miyazaki, Y. Yamashita, *et al.*, "Influence of respiration on cerebrospinal fluid movement using magnetic resonance spin labeling," *Fluids Barries CNS*, vol. 10, no. 1, p. 36, 2013.

[56] L. Chen, A. Beckett, A. Verma, and D. A. Feinberg, "Dynamics of respiratory and cardiac CSF motion revealed with real-time simultaneous multi-slice epi velocity phase contrast imaging," *Neuroimage*, vol. 122, pp. 281–287, 2015.

[57] S. Yatsushiro, S. Sunohara, H. Atsumi, M. Matsumae, and K. Kuroda, "Visualization and characterization of cerebrospinal fluid motion based on magnetic resonance imaging," *Hydrocephalus: Water on the Brain*, p. 9, 2018.

[58] S. Gupta, M. Soellinger, P. Boesiger, D. Poulikakos, and V. Kurtcuoglu, "Three-dimensional computational modeling of subject-specific cerebrospinal fluid flow in the subarachnoid space," *J. Biomech. Eng.*, vol. 131, no. 2, p. 021 010, 2009.

[59] S. Hakim and R. D. Adams, "The special clinical problem of syptomatic hydrocephalus with normal cerebrospinal fluid pressure: Observations on cerebrospinal fluid hydrodynamics," *J. Neurol. Sci.*, vol. 2, no. 4, pp. 307–327, 1965.

[60] W. G. Bradley, D. Scalzo, J. Queralt, W. N. Nitz, D. J. Atkinson, and P. Wong, "Normal-pressure hydrocephalus: evaluation with cerebrospinal fluid flow measurements at MR imaging," *Radiology*, vol. 198, no. 2, pp. 523–529, 1996.

[61] P. H. Luetmer, J. Huston, J. A. Friedman, *et al.*, "Measurement of cerebrospinal fluid flow at the cerebral aqueduct by use of phase-contrast magnetic resonance imaging: Technique validation and utility in diagnosing idiopathic normal pressure hydrocephalus," *Neurosurgery*, vol. 50, no. 3, pp. 534–543, 2002.

[62] S. Qvarlander, K. Ambarki, A. Wåhlin, *et al.*, "Cerebrospinal fluid and blood flow patterns in idiopathic normal pressure hydrocephalus," *Acta Neurol. Scand.*, vol. 135, no. 5, pp. 576–584, 2017.

[63] T. Esmade and S. Cooke, "Shunting for normal pressure hydrocephalus (nph)," *CDRS*, vol. 3, 2002.

[64] G. A. Bateman and A. Loiselle, "Can mr measurement of intracranial hydrodynamics and compliance differentiate which patient with idiopathic normal pressure hydrocephalus will improve following shunt insertion?" *Acta Neurochir (Wien)*, vol. 149, pp. 455–462, 2007.

[65] A. K. Sharma, S. Gaikwad, V. Gupta, A. Garg, and N. K. Mishra, "Measurement of peak csf flow velocity at cerebral aqueduct, before and after lumbar csf drainage, by use of phase-contrast mri: Utility in the management of idiopathic normal pressure hydrocephalus," *Clin. Neurol. Neurosurg.*, vol. 110, no. 4, pp. 363–368, 2008.

[66] B. Sweetman, M. Xenos, L. Zitella, and A. A. Linninger, "Three-dimensional computational prediction of cerebrospinal fluid flow in the human brain," *Med. Biol. Eng. Comput.*, vol. 41, no. 2, pp. 67–75, 2011.

[67] G. Bardan, F. Plouraboué, M. Zagzoule, and O. Baledent, "Simple patient-based transmantle pressure and shear estimate from cine phase-contrast MRI in cerebral aqueduct," *IEEE Trans. Biomed. Eng.*, vol. 59, no. 10, pp. 2874–2883, 2012.

[68] P. K. Eide and T. Sæhle, "Is ventriculomegaly in idiopathic normal pressure hydrocephalus associated with a transmantle gradient in pulsatile intracranial pressure?" *Acta Neurochir. (Wien)*, vol. 152, no. 6, pp. 989–995, 2010.

[69] G. Ringstad, K. E. Emblem, O. Geier, N. Alperin, and P. K. Eide, "Aqueductal stroke volume: Comparisons with intracranial pressure scores in idiopathic normal pressure hydrocephalus," *Am. J. Neuroradiol.*, vol. 36, no. 9, pp. 1623–1630, 2015. DOI: https://doi.org/10.3174/ajnr.A4340.

[70] K. Markenroth Bloch, J. Töger, and F. Ståhlberg, "Investigation of cerebrospinal fluid flow in the cerebral aqueduct using high-resolution phase contrast measurements at 7T MRI," *Acta Radiol.*, vol. 59, no. 8, pp. 988–996, 2018.

[71] J. Shanks, K. Markenroth Bloch, K. Laurell, *et al.*, "Aqueductal CSF stroke volume is increased in patients with idiopathic normal pressure hydrocephalus and decreases after shunt surgery," *Am. J. Neuroradiol.*, vol. 40, no. 3, pp. 453–459, 2019.

[72] S. Sincomb, W. Coenen, A. Sánchez, and J. Lasheras, "A model for the oscillatory flow in the cerebral aqueduct," *J. Fluid Mech.*, vol. 899, 2020.

[73] D. N. Levine, "Intracranial pressure and ventricular expansion in hydrocephalus: Have we been asking the wrong question?" *J. Neurol. Sci.*, vol. 269, no. 1-2, pp. 1–11, 2008.

[74] S. Sincomb, V. Haughton, A. Sanchez, E. Criado-Hidalgo, and J. C. Lasheras, "Strain accumulation visco-elastic ventriculomegaly hypothesis for the onset of idiopathic normal pressure hydrocephalus (inph)," *Biophys. J.*, vol. 118, no. 3, 452a, 2020.

[75] P Karki, P. M. Cogswell, M. Murphy, *et al.*, "Fluid mechanics based distinct cerebrospinal fluid dynamics signature in normal pressure hydrocephalus," in *ISMRM & ISMRT Annual Meeting & Exhibition*, International Society for Magnetic Resonance in Medicine, 2023.

[76] V. Vinje, G. Ringstad, E. K. Lindstrøm, *et al.*, "Respiratory influence on cerebrospinal fluid flow–a computational study based on long-term intracranial pressure measurements," *Sci. Rep.*, vol. 9, no. 1, pp. 1–13, 2019. DOI: https://doi.org/10.1038/s41598-019-46055-5.

[77] R. D. Penn, M. C. Lee, A. A. Linninger, K. Miesel, S. N. Lu, and L. Stylos, "Pressure gradients in the brain in an experimental model of hydrocephalus," *J. Neurosurg.*, vol. 102, no. 6, pp. 1069–1075, 2005.

[78] P. Longatti, A. Fiorindi, P. Peruzzo, L. Basaldella, and F. M. Susin, "Form follows function: Estimation of CSF flow in the third ventricle–aqueduct–fourth ventricle complex modeled as a diffuser/nozzle pump," *J. Neurosurg.*, vol. 1, no. aop, pp. 1–8, 2019.

[79] S. Sincomb, W. Coenen, E Criado-Hidalgo, *et al.*, "Transmantle pressure computed from mr imaging measurements of aqueduct flow and dimensions," *Am. J. Neuroradiol.*, vol. 42, no. 10, pp. 1815–1821, 2021.

[80] E. E. Jacobson, D. F. Fletcher, M. K. Morgan, and I. H. Johnston, "Fluid dynamics of the cerebral aqueduct," *Pediatr. Neurosurg.*, vol. 24, no. 5, pp. 229–236, 1996.

[81] E. E. Jacobson, D. F. Fletcher, M. K. Morgan, and I. H. Johnston, "Computer modelling of the cerebrospinal fluid flow dynamics of aqueduct stenosis," *Med. Biol. Eng. Comput.*, vol. 37, no. 1, pp. 59–63, 1999.

[82] L. Fin and R. Grebe, "Three dimensional modeling of the cerebrospinal fluid dynamics and brain interactions in the aqueduct of sylvius," *Comput. Methods Biomech. Biomed. Engin.*, vol. 6, no. 3, pp. 163–170, 2003.

[83] V. Kurtcuoglu, M. Soellinger, P. Summers, *et al.*, "Computational investigation of subject-specific cerebrospinal fluid flow in the third ventricle and aqueduct of sylvius," *J. Biomech.*, vol. 40, no. 6, pp. 1235–1245, 2007.

[84] M. Schibli, M. Wiesendanger, L. Guzzella, *et al.*, "In-vitro measurement of ventricular cerebrospinal fluid flow using particle tracking velocimetry and magnetic resonance imaging," in *2008 First International Symposium on Applied Sciences on Biomedical and Communication Technologies*, IEEE, 2008, pp. 1–5.

[85] J. M. Furlan, J. R. Kadambi, K. A. Loparo, S. N. Sreenath, and S. Manjila, "Piv investigation of cerebral spinal fluid flow in the cerebral ventricular system," *J. Flow Vis. Image Process.*, vol. 16, no. 2, 2009. DOI: 10.1615/JFlowVisImageProc.v16.i2.30.

[86] S. Bottan, D. Poulikakos, and V. Kurtcuoglu, "Phantom model of physiologic intracranial pressure and cerebrospinal fluid dynamics," *IEEE Trans. Biomed. Eng.*, vol. 59, no. 6, pp. 1532–1538, 2012.

[87] P. Holmlund, S. Qvarlander, J. Malm, and A. Eklund, "Can pulsatile CSF flow across the cerebral aqueduct cause ventriculomegaly? a prospective study of patients with communicating hydrocephalus," *Fluids Barriers CNS*, vol. 16, no. 1, pp. 1–10, 2019.

[88] S. Sincomb, "Modeling of cerebrospinal fluid flow using quantitative mri for clinical application," Ph.D. dissertation, UCSD, 2022.

[89] N. Riley, "Steady streaming," *Annu. Rev. Fluid Mech.*, vol. 33, no. 1, pp. 43–65, 2001. DOI: https://doi.org/10.1146/annurev.fluid.33.1.43.

[90] J. T. Stuart, "Double boundary layers in oscillatory viscous flow," *J. Fluid Mech.*, vol. 24, no. 4, pp. 673–687, 1966.

[91] J. B. Grotberg, "Volume-cycled oscillatory flow in a tapered channel," *J. Fluid Mech.*, vol. 141, pp. 249–264, 1984. DOI: https://doi.org/10.1017/S0022112084000823.

[92] J. Jackson and B. Williams, "Errors in velocity measurement by the Pitot principle in fluids with slowly propagated pressure waves," *J. Biomed. Eng.*, vol. 1, pp. 50–54, 1979. DOI: https://doi.org/10.1016/0141-5425(79)90010-4.

[93] B. Kalata W. Martin, M. Oshinski J.N. Jerosch-Herold, T. Royston, and F. Loth, "MR measurement of cerebrospinal fluid velocity wave speed in the spinal canal," *IEEE Trans. Biomed. Eng.*, vol. 56, 1765–1768, 2009. DOI: https://doi.org/10.1109/TBME.2008.2011647.

[94] K. Sonnabend, G. Brinker, D. Maintz, A. Bunck, and K. Weiss, "Cerebrospinal fluid pulse wave velocity measurements: In vitro and in vivo evaluation of a novel multiband cine phase-contrast MRI sequence," *Magn. Reson. Med.*, vol. 85, 197– 208, 2020. DOI: https://doi.org/10.1002/mrm.28430.

[95] P. Peñas López, B. Van Elburg, M. Parrales, and J. Rodríguez-Rodríguez, "Diffusion of dissolved CO_2 in water propagating from a cylindrical bubble in a horizontal hele-shaw cell," *Phys. Rev of Fluids*, vol. 2, 2017. DOI: https://doi.org/10.1103/PhysRevFluids.2.063602.

[96] K. Tangen, R. Leval, A. Mehta, and A. Linninger, "Computational and in vitro experimental investigation of intrathecal drug distribution: Parametric study of the effect of injection volume, cerebrospinal fluid pulsatility, and drug uptake," *Anesth. Analg.*, vol. 124, no. 5, pp. 1686–1696, 2017. DOI: https://doi.org/10.1213/ANE.0000000000002011.

[97] J. Holtsmark, I. Johnsen, T. Sikkeland, and S. Skavlem, "Boundary layer flow near a cylindrical obstacle in an oscillating, incompressible fluid," *J. Acoust. Soc. Am.*, vol. 26, no. 1, pp. 26–39, 1954. DOI: https://doi.org/10.1121/1.1907285.

[98] Q. Hogan, "Size of human lower thoracic and lumbosacral nerve roots," *ASA*, vol. 85, no. 1, pp. 37–42, 1996.

[99] H. E. Killer, H. R. Laeng, J. Flammer, and P. Groscurth, "Architecture of arachnoid trabeculae, pillars, and septa in the subarachnoid space of the human optic nerve: Anatomy and clinical considerations," *BJO*, vol. 87, no. 6, pp. 777–781, 2003.

[100] H. Stockman, "Effect of anatomical fine structure on the flow of cerebrospinal fluid in the spinal subarachnoid space," *J. Biomech. Eng.*, vol. 128, no. 1, pp. 106–114, 2006.

[101] H. Stockman, "Effect of anatomical fine structure on the dispersion of solutes in the spinal subarachnoid space," *J. Biomech. Eng.*, vol. 129, no. 5, pp. 666–675, 2007.

[102] J. Holtsmark, I. Johnsen, T. Sikkeland, and S. Skavlem, "Boundary layer flow near a cylindrical obstacle in an oscillating, incompressible fluid," *J. Acoust. Soc. Am.*, vol. 26, no. 1, pp. 26–39, 1954.

[103] W. Raney, J. Corelli, and P. Westervelt, "Acoustical streaming in the vicinity of a cylinder," *J. Acoust. Soc. Am.*, vol. 26, no. 6, pp. 1006–1014, 1954.

[104] M. Tatsuno, "Circulatory streaming around an oscillating circular cylinder at low Reynolds numbers," *Journal of the Physical Society of Japan*, vol. 35, no. 3, pp. 915–920, 1973.

[105] B. R. Lutz, J. Chen, and D. T. Schwartz, "Microscopic steady streaming eddies created around short cylinders in a channel: Flow visualization and stokes layer scaling," *Phys. Fluids*, vol. 17, no. 2, p. 023 601, 2005.

[106] B. R. Lutz, J. Chen, and D. T. Schwartz, "Hydrodynamic tweezers: 1. noncontact trapping of single cells using steady streaming microeddies," *Analytical Chemistry*, vol. 78, no. 15, pp. 5429–5435, 2006.

[107] P. Bearman, M. Downie, J. Graham, and E. Obasaju, "Forces on cylinders in viscous oscillatory flow at low Keulegan-Carpenter numbers," *J. Fluid Mech.*, vol. 154, pp. 337–356, 1985.

[108] N. Riley, "On a sphere oscillating in a viscous fluid," *Q. J. Mech. Appl. Math.*, vol. 19, no. 4, pp. 461–472, 1966.

[109] W. Coenen, "Steady streaming around a cylinder pair," *Proc. R. Soc. A: Math. Phys. Eng. Sci.*, vol. 472, no. 2195, 2016.

[110] B. Yan, D. Ingham, and B. Morton, "Streaming flow induced by an oscillating cascade of circular cylinders," *J. Fluid Mech.*, vol. 252, pp. 147–171, 1993.

[111] M. Higa and T. Takahashi, "Stationary flow induced by an unharmonically oscillating sphere," *J. Phys. Soc. Japan*, vol. 56, no. 5, pp. 1703–1712, 1987.

[112] M. Tatsuno, "Secondary flow induced by a circular cylinder performing unharmonic oscillations," *J. Phys. Soc. Japan*, vol. 50, no. 1, pp. 330–337, 1981.

[113] T. Miyagi and K. Nakahasi, "Secondary flow induced by an unharmonically oscillating circular cylinder," *J. Phys. Soc. Japan*, vol. 39, no. 2, pp. 519–526, 1975.

[114] Y. Bhosale, T. Parthasarathy, and M. Gazzola, "Shape curvature effects in viscous streaming," *J. Fluid Mech.*, vol. 898, 2020.

[115] J. J. Lawrence, W. Coenen, A. L. Sánchez, *et al.*, "On the dispersion of a drug delivered intrathecally in the spinal canal," *J. Fluid Mech.*, vol. 861, pp. 679–720, 2019.

[116] W. Thielicke and E. Stamhuis, "Pivlab-towards user-friendly, affordable and accurate digital particle image velocimetry in matlab," *J. Open Res. Softw.*, vol. 2, no. 1, 2014. DOI: http://dx.doi.org/10.5334/jors.bl.

[117] K. Chong, S. Kelly, S. Smith, and J. Eldredge, "Inertial particle trapping in viscous streaming," *Phys. Fluids*, vol. 25, no. 3, p. 033 602, 2013.

[118] J. Alaminos-Quesada, "Limit of the two-dimensional linear potential theories on the propulsion of a flapping airfoil in forward flight in terms of the reynolds and strouhal number," *Phys. Rev. Fluids*, vol. 6, p. 123 101, 12 2021.

[119] B. Davidson and N. Riley, "Jets induced by oscillatory motion," *J. Fluid Mech.*, vol. 53, no. 2, pp. 287–303, 1972.

[120] J. Alaminos-Quesada, C. Gutiérrez-Montes, W. Coenen, and A. Sánchez, "Stationary flow driven by non-sinusoidal time-periodic pressure gradients in wavy-walled channels," *Applied Mathematical Modelling*, vol. 122, pp. 693–705, 2023.

[121] P. A. Yushkevich, J. Piven, H. Cody Hazlett, *et al.*, "User-guided 3D active contour segmentation of anatomical structures: Significantly improved efficiency and reliability," *Neuroimage*, vol. 31, no. 3, pp. 1116–1128, 2006.

[122] A. Di Ieva, E. M. Schmitz, and M. D. Cusimano, "Analysis of intracranial pressure: Past, present, and future," *The Neuroscientist*, vol. 19, no. 6, pp. 592–603, 2013.

[123] D.-S. Kim, J.-U. Choi, R. Huh, P.-H. Yun, and D.-I. Kim, "Quantitative assessment of cerebrospinal fluid hydrodynamics using a phase-contrast cine mr image in hydrocephalus," *Childs Nerv. Syst.*, vol. 15, pp. 461–467, 1999. DOI: https://doi.org/10.1007/s003810050440.

[124] A. Benninghaus, O. Balédent, A. Lokossou, C. Castelar, S. Leonhardt, and K. Radermacher, "Enhanced in vitro model of the csf dynamics," *Fluids Barriers CNS*, vol. 16, no. 1, pp. 1–11, 2019.

[125] T. Miyati, M. Mase, T. Banno, *et al.*, "Frequency analyses of csf flow on cine mri in normal pressure hydrocephalus," *Eur. Radiol.*, vol. 13, pp. 1019–1024, 2003.

[126] J. Alaminos-Quesada, W. Coenen, C. Gutiérrez-Montes, and A. Sánchez, "Buoyancy modulated Lagrangian drift in wavy-walled vertical channels as a model problem to understand drug dispersion in the spinal canal," *J. Fluid Mech.*, vol. 949, no. A48, 2022.